V.Naumov

From Cosmic Rays to Neutrino Oscillations

Part I

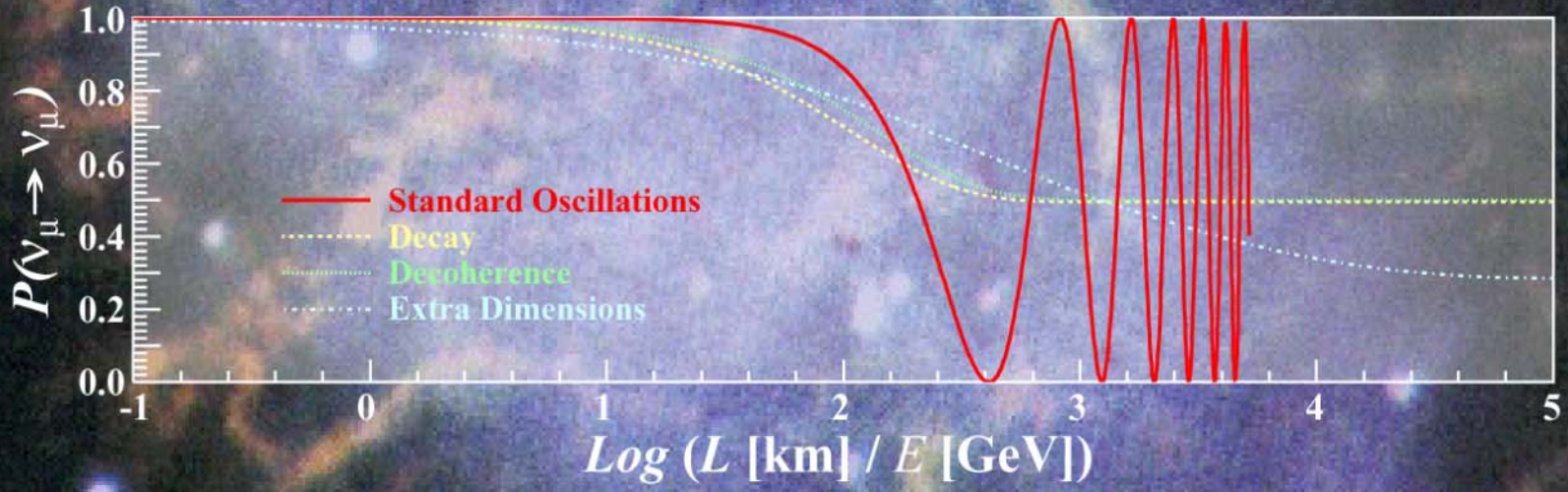

JINR, Dubna, February 2006

What are Cosmic Rays?

Cosmic Rays (CR) are high-energy particles of extraterrestrial origin

The astrophysical field of activity for particle and nuclear physics

"Classical" **CR** are nuclei or ionized atoms ranging from a single proton up to an iron nucleus and beyond, but being mostly **protons** (~90%) and α **particles** (~9%).

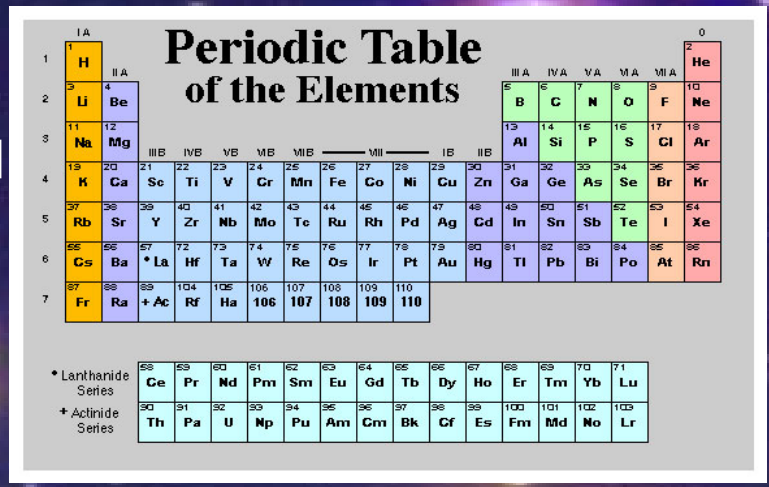

However the above "definition" is much wider and includes in fact all stable and quasistable particles:

- antiprotons & (maybe) antinuclei,
- neutrons (e.g., from the Sun),
- hard gamma rays ($\lambda < 10^{-12}$ cm),
- electrons & positrons,
- neutrinos & antineutrinos,
- esoteric entities (strangelets, relativistic WIMPs, magnetic monopoles, relic mini black holes, microscopic black holes & branes from extra dimesions, mirror particles, ... *whatever you want*).

Secondary CR (produced by the primaries in the Earth's atmosphere) consist of essentially all elementary particles and nuclei (both stable and unstable). The most important are

- nucleons, stable nuclei & radionuclides,
- (hard) gamma rays,
- mesons ($\pi^{\pm}$,π^{0},$K^{\pm}$, …, $D^{\pm}$,…),
- charged leptons ($e^{\pm}$, $\mu^{\pm}$, $\tau^{\pm}$),
- neutrinos & antineutrinos (ν_e, ν_μ, ν_τ),
- exotics.

Discovery of elementary particles

Particle	Year	Discoverer (Nobel Prize)	Method	
e^-	1897	Thomson (1906)	Discharges in gases	
p	1919	Rutherford	Natural radioactivity	
n	1932	Chadwik (1935)	Natural radioactivity	
e^+	1933	Anderson (1936)	Cosmic Rays	★
$\mu^\pm$	1937	Neddermeyer, Anderson	Cosmic Rays	★
$\pi^\pm$	1947	Powell (1950) , Occhialini	Cosmic Rays	★
$K^\pm$	1949	Powell (1950)	Cosmic Rays	★
π^0	1949	Bjorklund	Accelerator	
K^0	1951	Armenteros	Cosmic Rays	★
Λ^0	1951	Armenteros	Cosmic Rays	★
Δ	1932	Anderson	Cosmic Rays	★
Ξ^-	1932	Armenteros	Cosmic Rays	★
$\Sigma^\pm$	1953	Bonetti	Cosmic Rays	★
p^-	1955	Chamberlain, Segre' (1959)	Accelerators	
anything else	1955 $\Longrightarrow$ today	various groups	Accelerators	
$m_\nu \neq 0$	2000	KAMIOKANDE	Cosmic rays	★

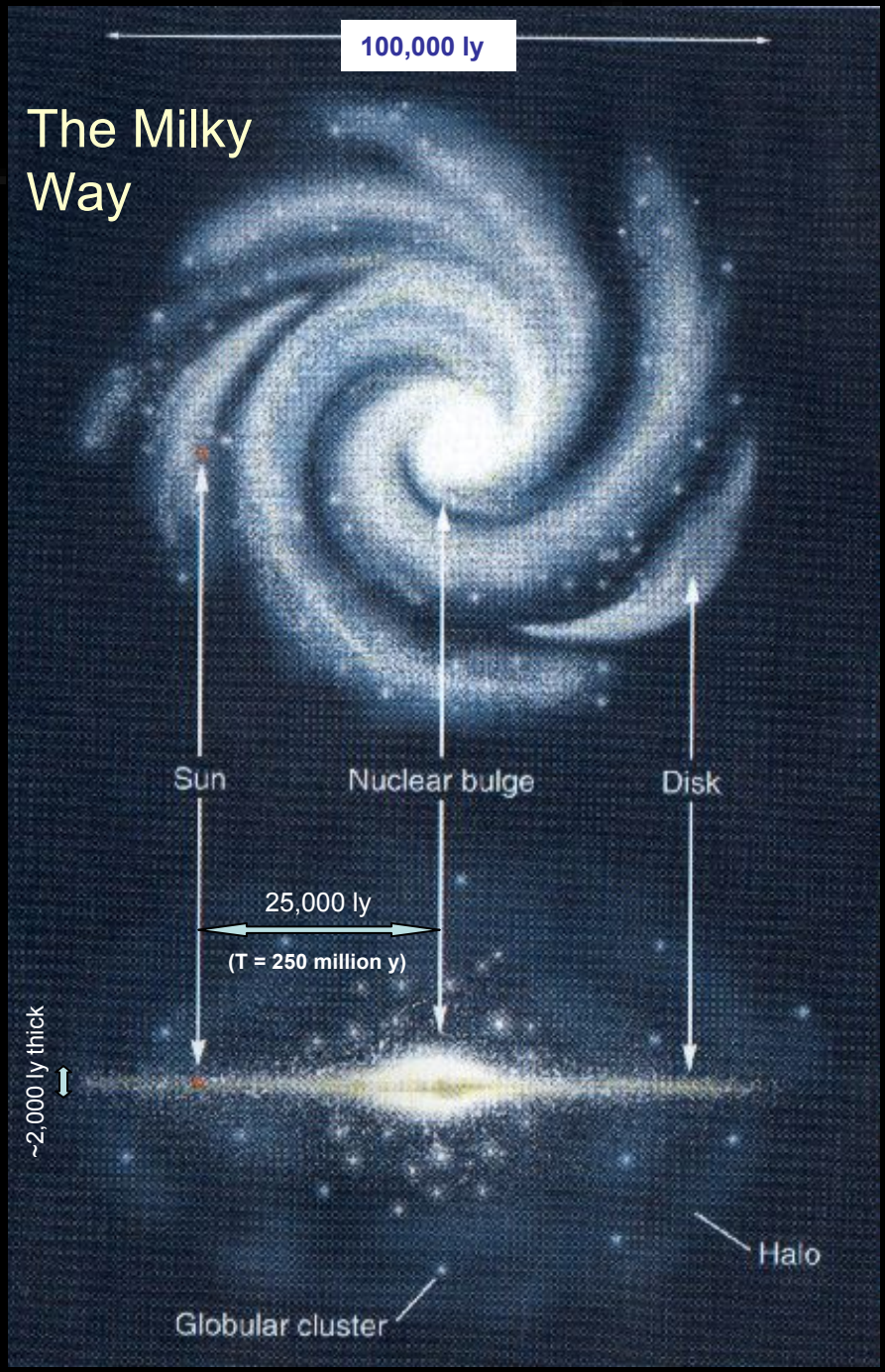

The mean concentration of the (classical) CL near the Earth $n_{CR} \sim 10^{-10}$ cm^{-3}.
The mean energy $\langle E_{CR} \rangle \sim 10$ GeV.
Therefore, the mean energy density is

$$\varepsilon_{CR} = n_{CR} \langle E_{CR} \rangle \sim 1 \text{ eV/cm}^3 \sim 10^{-12} \text{ erg/cm}^3$$

The mean density in the Galaxy is of the same order of magnitude and the full energy of CR in the Galaxy can be estimated

$$W_{CR}^{Disk} \sim \varepsilon_{CR} V_{Disk} \sim 10^{55} \text{ erg} \sim 10 M_{Sun} c^2$$

$$W_{CR}^{Halo} \sim \varepsilon_{CR} V_{Halo} \sim 10^{56} \text{ erg} \sim 100 M_{Sun} c^2$$

It is of the order of (or larger than) the kinetic energy of the interstellar gas and of the interstellar magnetic field!

CR is one of the factor affecting the energetics of the Galaxy.

The same is true for essentially all the "normal" galaxies.

For the powerful radio-galaxies the full energy of CR is fantastically large:

$$W_{CR} \sim 10^{60\text{-}61} \text{ erg} \sim 10^7 M_{Sun} c^2.$$

Honorable Mention to Cosmic Rays

In a sense, the solar system is built from Cosmic Rays.

Cosmic Rays affected (and maybe still affect) the evolution of the life on the Earth being during billions of years a catalyzer of mutations.

It might be that Cosmic Rays killed the dinosaurs (thanks so much!).

Cosmic Rays probably affect the climate on the Earth.

Cosmic Rays produce fantastic Aurora Polaris (also thanks, mainly from Eskimos).

Cosmic Rays are associated with the extreme phenomena in the Universe (SNs, GRBs, radio-galaxies, quasars,…)

In background: Mounted cast skeleton of Afrovenator, a predator that grew to a length of 30 feet. Sereno's team discovered Afrovenator in 130-million-year-old sediments during his 1993 expedition to Niger. Photo by Paul Sereno. **From <http://www-news.uchicago.edu/releases/photos/expedition2/>**

Big Bang Nucleosynthesis

Era of Nuclear Reactions: ~3 min to ~3.5 min (T ~ 10^9 to 10^8 K)

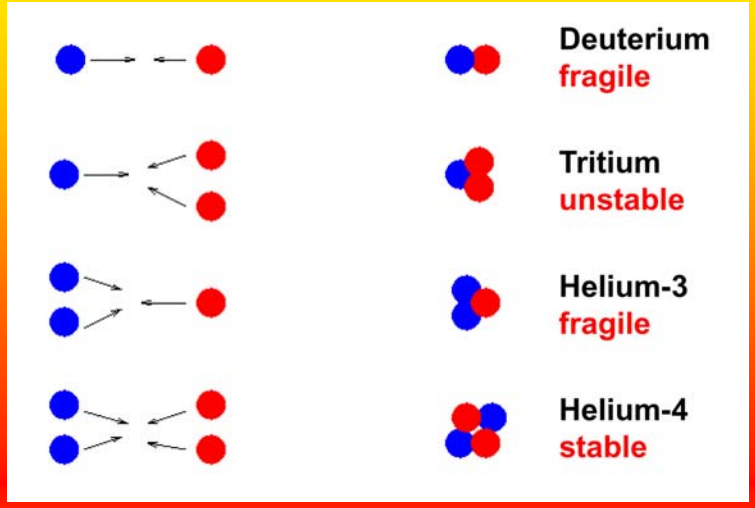

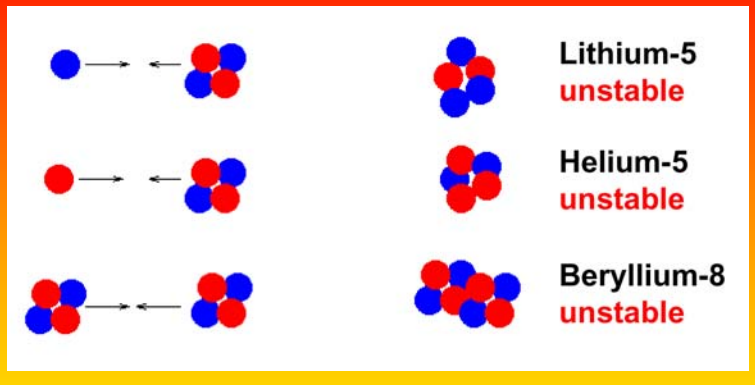

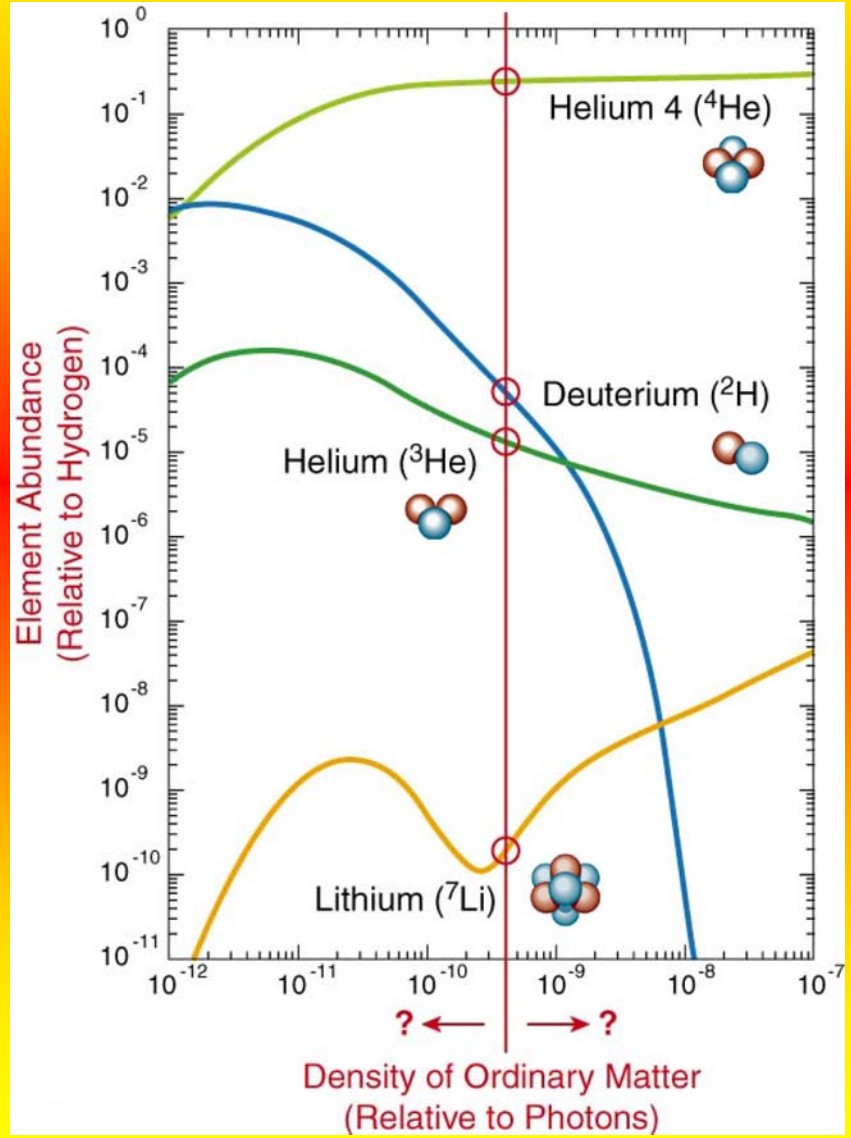

The net result of the early nuclear reactions is to transform all of the neutrons, along with the necessary protons, into ^{4}He plus traces of ^{2}H, ^{3}He, ^{7}Li, ^{6}Li, ^{7}Be.

Supernovae

SN1998S in NGC3877
by Enrico Prosperi

SN1998S in NGC387
by Pedro Re

SN 2001V - N3987s1
by Rafael Ferrando

From David Bishop's collection of real optical supernova images
International Supernovae Network, URL: <http://www.supernovae.net/snimages/animations.html>

A Supernovae Taxonomy

Early Spectra:

No Hydrogen / Hydrogen

up to 10^{43} J usually old stars

up to 10^{44} J often young, heavy stars

SN I
Si/ No Si

SN II
~3 mos. spectra
He dominant/H dominant

SN Ia
1985A
1989B

He poor/He rich
(absorption near 5700 A)

SN Ic
1983I
1983V

SN Ib
1983N
1984L

SN IIb
1993J
1987K

"Normal" SN II
Light Curve decay after maximum
Linear / Plateau

SN IIL
1980K
1979C

SN IIP
1987A
1988A
1969L

Believed to originate from **deflagration** or **detonation** of an ***accreting white dwarf***

Core collapse
Most (NOT all) H is removed during evolution by tidal stripping

Core Collapse
Outer Layers stripped by winds *(Wolf-Rayet Stars)* or binary interactions
Ib: H mantle removed
Ic: H & He removed

Core Collapse
of a massive progenitor with plenty of H

Theory

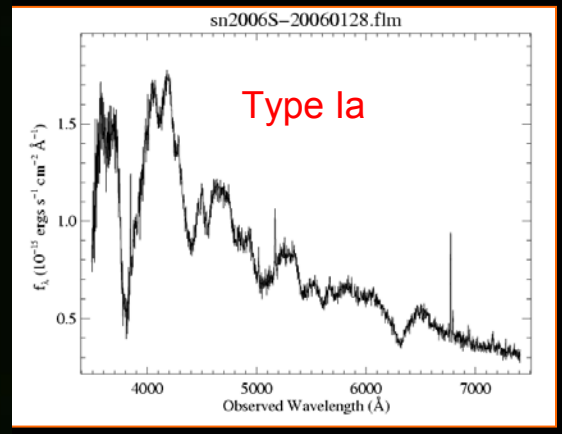

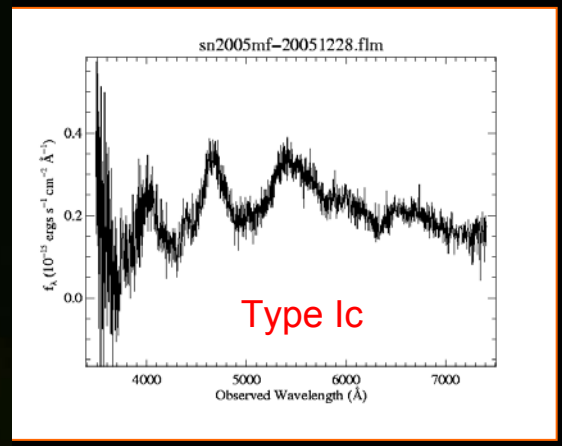

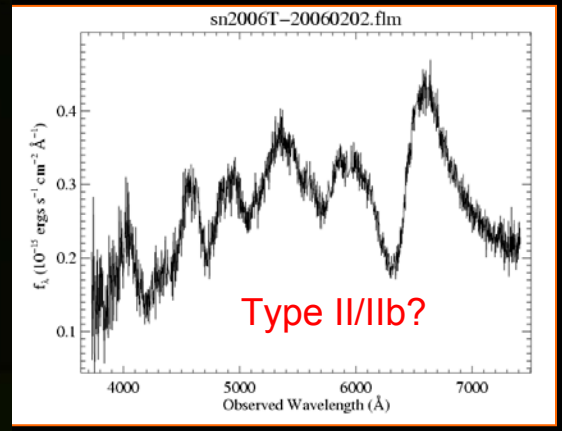

Artist's concepts of supernova explosions

There is an initial flash of light from the supernova explosion causing the ring to glow. Debris hurls into space, the fastest moving at 0.1*c*. The supernova's shockwave causes the ring to glow again.

The closer the pieces of the ring are to the shockwave, the sooner they light up. Eventually, the whole ring lights up.

[from NASA HubblSite]

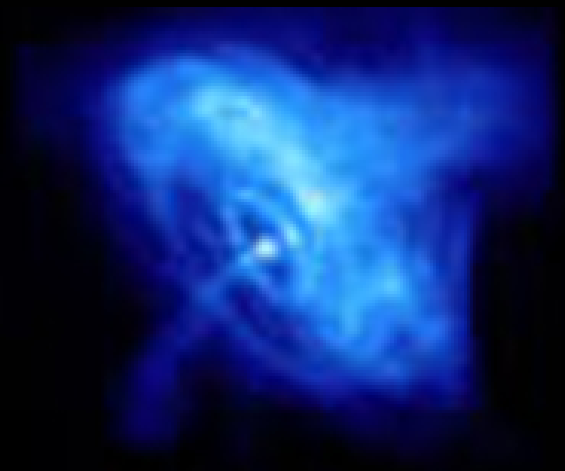

The Crab Nebula, the remnant of a supernova explosion

The X-ray image shows tilted rings or waves of high-energy particles that appear to have been flung outward over the distance of a *light year* from the central star, and high-energy jets of particles blasting away from the neutron star in a direction perpendicular to the spiral. It provides important clues to the puzzle of how the cosmic generator, a pulsing neutron star, energizes the nebula, which still glows brightly 952 years after the SN explosion.

According to **Martin Weisskopf** (NASA's Marshall Space Flight Center)

"The Crab pulsar is accelerating particles up to the speed of light and flinging them out into interstellar space at an incredible rate."

[from Chandra X-ray Observatory]

Genus Diversity & Cosmic Rays

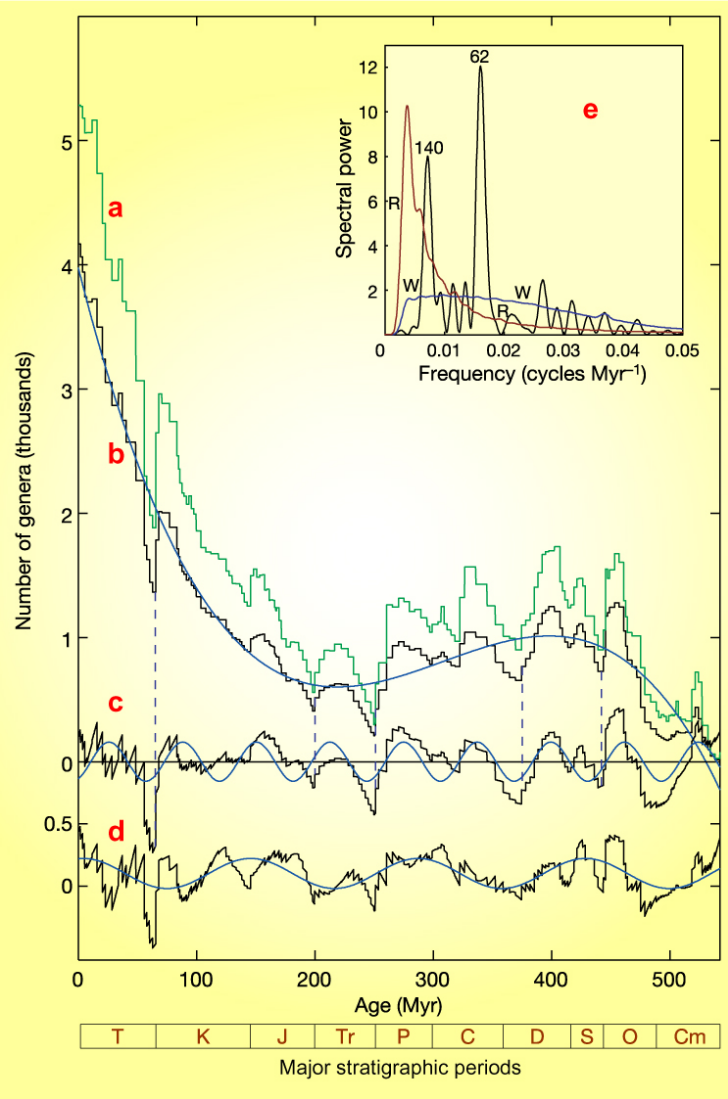

Physicists Robert Rohde and Richard Muller (University of California) analyzed the fossil records of marine animals over the past 542 million years and found that biodiversity appears to rise and fall in mysterious cycles of 62 million years. These cycles cannot be explain by any terrestrial process.

a. The green plot shows the number of known marine animal genera versus time from Sepkoski's compendium, converted to the 2004 Geologic Time Scale.

b. The black plot shows the same data, with single occurrence and poorly dated genera removed. The trend line (blue) is a third-order polynomial fitted to the data.

c. As b, with the trend subtracted and a 62-Myr sine wave superimposed.

d. The detrended data after subtraction of the 62-Myr cycle and with a 140-Myr sine wave superimposed. Dashed vertical lines indicate the times of the five major extinctions.

e. Fourier spectrum of c. Curves W (in blue) and R (in red) are estimates of spectral background.

[**Reference**: R.A. Rohde & R.A. Muller, "Cycles in fossil diversity," Lett. to Nature, **434** No. 10 (2005) 208-210.]

It seems the puzzle is already resolved by Mikhail Medvedev and Adrian Melott (Kansas University).

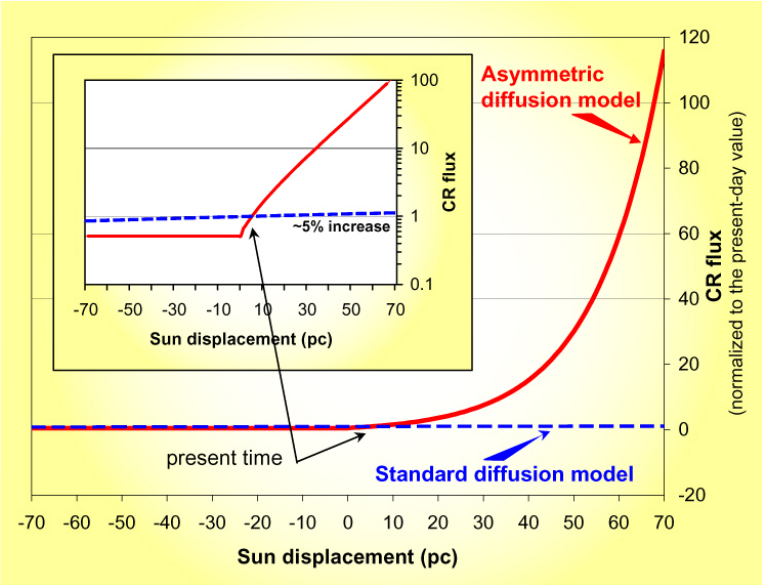

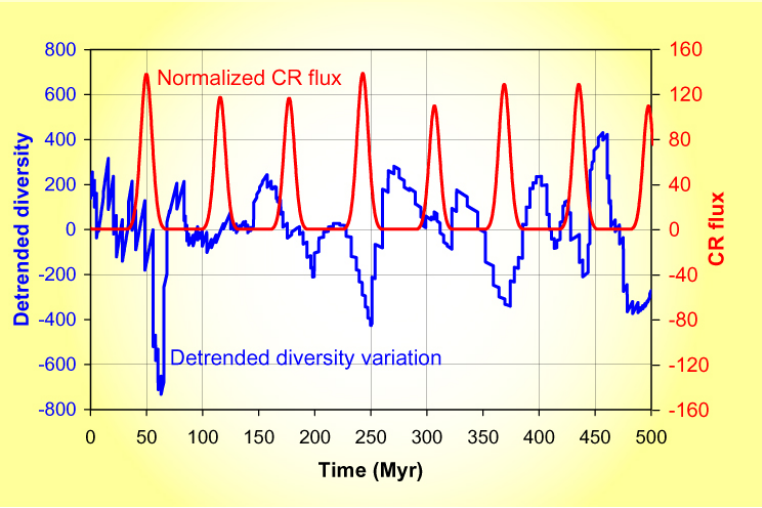

While astro- and geophysical phenomena may be periodic for such a long time, no plausible mechanism has been found. The fact that the period of the diversity cycle (62 My) is close to the 64 My period of the vertical oscillation of the Solar system relative to the galactic disk is suggestive. However, any model involving cosmogenic processes modulated by the Sun's midplane crossing or its maximal vertical distance from the galactic plane predicts a half-period cycle, i.e. about 32 My.

Medvedev & Melott propose that the diversity cycle is caused by the anisotropy of cosmic ray (CR) production in the galactic halo/wind/termination shock and the shielding effect of the galactic magnetic fields.

CRs influence cloud formation, can affect climate and harm live organisms directly via increase of radiation dose.

The CR anisotropy is caused by the galactic north-south asymmetry of the termination shock due to the interaction with the “warm-hot intergalactic medium” as our galaxy falls toward the Virgo cluster (nearly in the direction of the galactic north pole) with a velocity of order 200 km/s.

After a revision of the mechanism of CR propagation in the galactic magnetic fields it was show that the shielding effect is strongly position-dependent. It varies by a factor of a hundred and reaches a minimum at the maximum northward displacement of the Sun. Very good phase agreement between maximum excursions of the Sun toward galactic north and minima of the fossil diversity cycle further supports the model.

[**Reference**: M.V. Medvedev & A.L. Melott, “Do extragalactic cosmic rays induce cycles in fossil diversity?,” astro-ph/0602092 (Feb. 4, 2006).]

A note

If the Medvedev-Melott model is right we have a very good new instrument for studying CR time variations.

Selected recent determinations of Z

Reference	Z (ps)	Sample
Conti & Vacca (1990)	15 ± 3	WR stars (N = 101) within 4.5 kpc of Sun
Cohen (1995)	15.5 ± 0.7	IRAS point-source counts + point-source sky model
Humphreys & Larsen (1995)	20.5 ± 3.5	Galactic-pole star counts (N ~ 10,000) plus Bahcall-Soneira galaxy model
Mendez & van Altena (1998)	27 ± 3	Solar-neighborhood reddening model plus star counts
Binney et al. (1997)	14 ±4	COBE/DIRBE surface-brightness analysis; double-exponential disk + power-law bulge
Reed (1997)	~10–12	OB stars with | b | < 10°; averaged M_B values for rough OB classes; assumed extinction model
Chen et al. (1999)	27.5 ± 6.0	COBE/IRAS-based extinction model
Ma'z-Apell‡niz (2001)	24.2 ± 1.7	*Hipparcos* parallaxes for 3382 O-B5 stars (|b| > 5°) within ~ 350 pc, plus distribution model
Joshi (2005)	22.8 ± 3.3	extinction analysis for ~ 600 open clusters with |b| < 5°

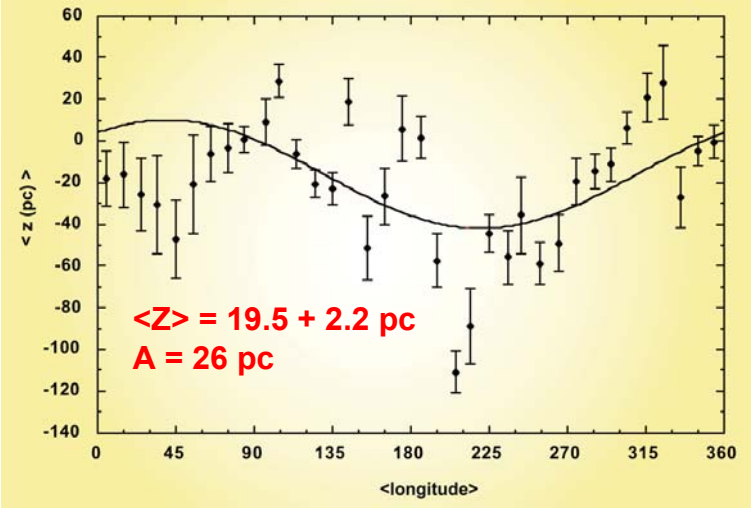

The data on the Sun's displacement from the galactic plane are quite uncertain. Therefore the above difference between 62 and 64 My does not seem essential.

[Reference: B.C. Reed, "The Sun's displacement from the galactic plane from spectroscopic parallaxes of 2400 OB stars," astro-ph/0507655 (Jul. 2005), submitted to J. Roy. Astron. Soc. Canada.]

Solar Wind and Aurora Polaris

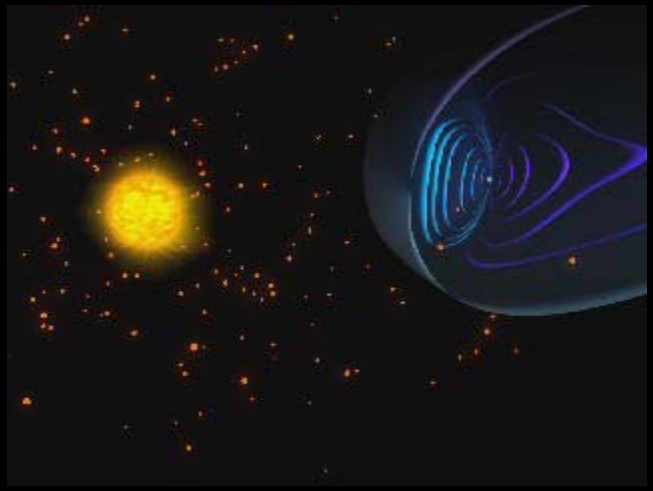

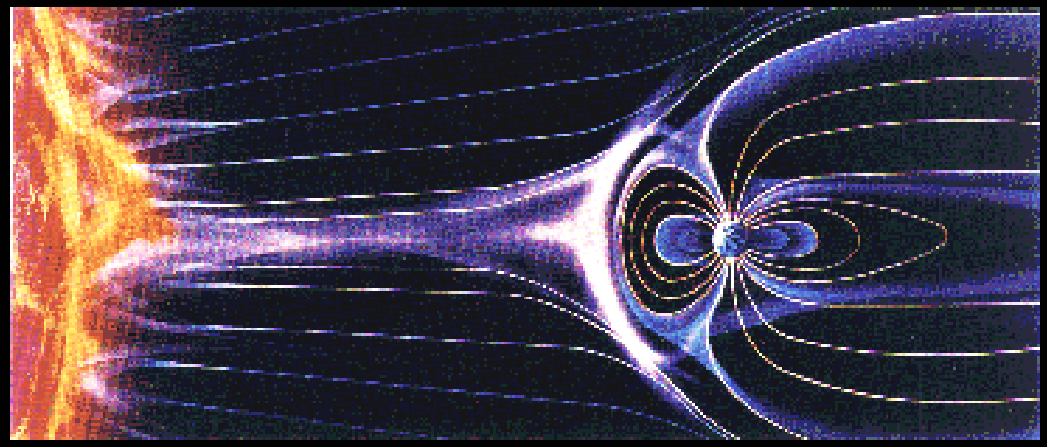

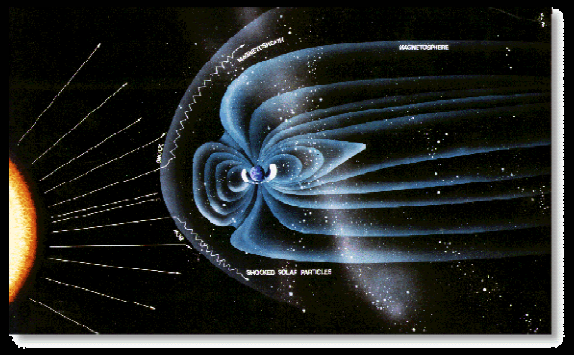

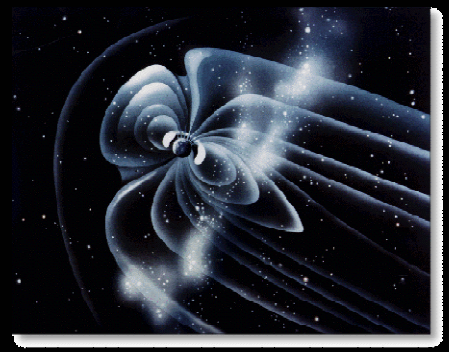

SN-GRB Connection

The collapsar model of a gamma-ray burst posits an event very like a Type Ic supernova. When a massive star collapses into a black hole surrounded by a disk of accreting matter, streaming particle jets along the rotation axis could give rise to the supernova and the GRB.

[**From:** SWIFT Satellite animation, Jet Propulsion Laboratory and NASA]

Gamma-ray Bursts (GRBs) are bright flashes of high energy (~1 keV to ~10 MeV) photons.

"The largest bangs in the Universe since the Big one"
(Brian Schmidt)

The GRBs can last from a few milliseconds up to ~10 minutes. Their origin and nature have puzzled the scientific community for about 25 years until 1997, when the first X-ray afterglows of long (> 2 s duration) bursts were detected and the first optical and radio counterparts were found. These measurements established that long GRBs are typically at high redshift (***z* ~1.6**) and are in sub-luminous star-forming host galaxies. They are likely produced in core-collapse explosions of a class of massive stars that give rise to highly relativistic jets (collapsar model).

Internal inhomogeneities in the velocity field of the relativistic expanding flow lead to collisions between fast moving and slow moving fluid shells and to the formation of internal shock waves. These shocks are believed to produce the observed prompt emission in the form of irregularly shaped and spaced pulses of gamma-rays, each pulse corresponding to a distinct internal collision. The expansion of the jet outward into the circumstellar medium is believed to give rise to "external" shocks, responsible for producing the smoothly fading afterglow emission seen in the X-ray, optical and radio bands.

[**Reference:** G. Cusumano *et al.*, "Detection of a huge explosion in the early Universe," astro-ph/0509737 (submitted to Nature).]

An off-axis Type Ic supernova 2003jd as observed by the Australian National Observatory.

More often than not, supernovae are asymmetric. Thus, when you look at Type Ic supernovae from different angles, they look different.

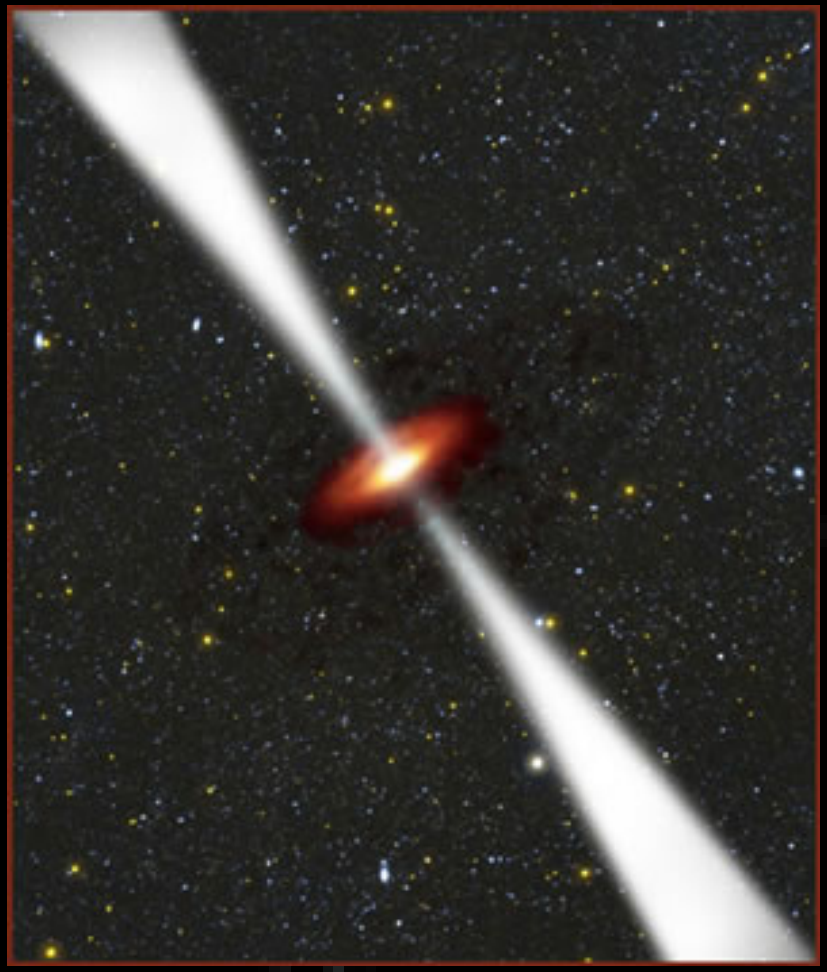

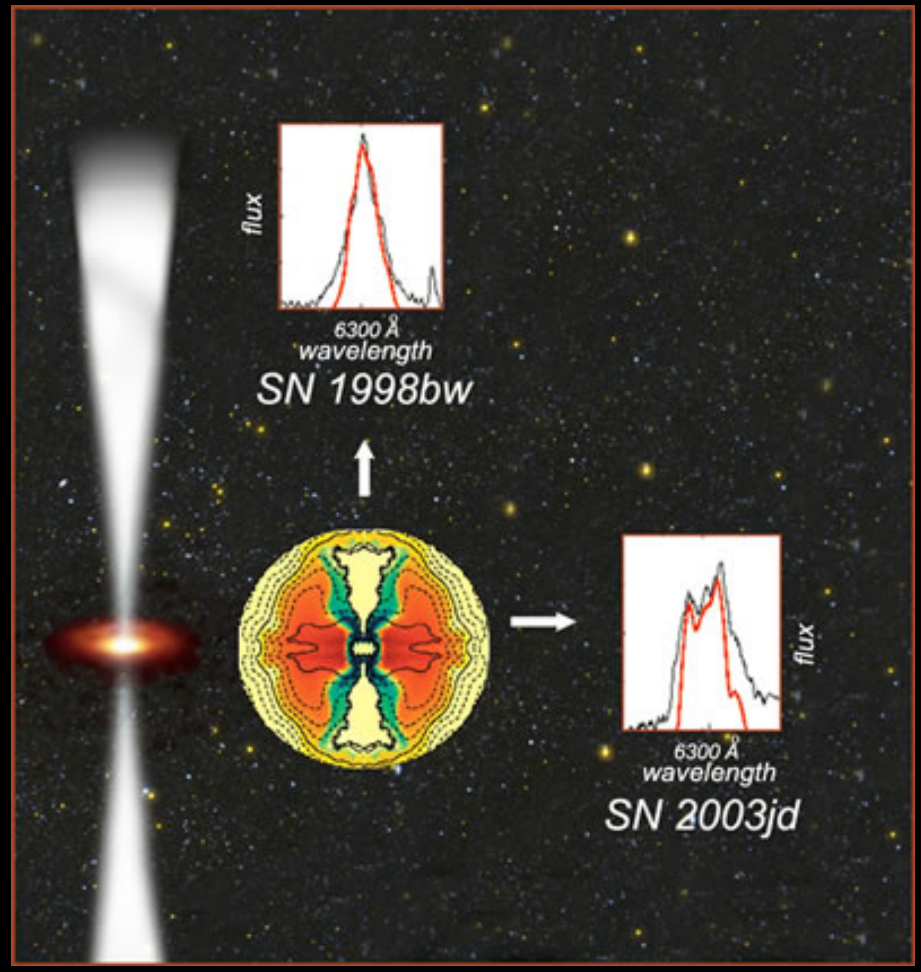

Some (long-duration) gamma-ray bursts may be associated with Type Ic supernovae, which occur when a massive star collapses to form a black hole or neutron star.

[**From:** Paul Preuss, "It's an exceptional supernova, but is it a GRB?" **science@berkeley lab**, August 5, 2005]

Whether a Type Ic supernova is seen as a gamma-ray burst could depend upon how the asymmetric object is viewed. SN 1998bw may have been viewed along the axis of the jets; its spectrum showed a strong, single peak in the oxygen emission line. SN 2003jd may have been viewed from the side, through a rapidly rotating disk that caused the oxygen line to split.

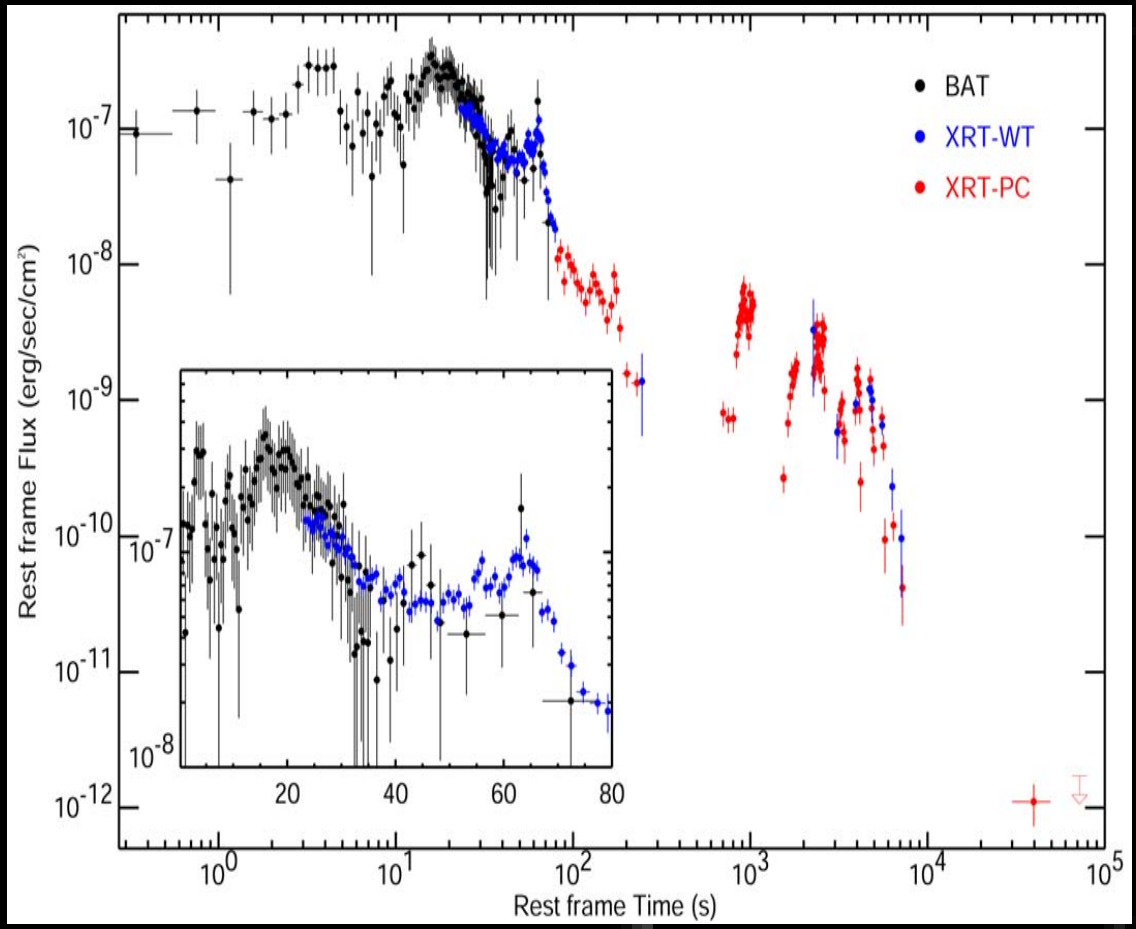

Light curve of **GRB 050904** as observed by the Swift Burst Alert Telescope (**BAT**) and X-ray Telescope (**XRT**). **WT** is windowed timing mode data, and **PC** is photon counting data.

This plot shows the evolution of the GRB flux in the source rest frame. The rest frame flux is calculated from the 0.2-10 keV observed flux by multiplying by $(1+z)^2$ with z=6.29, and corresponds to flux emitted in the 1.4-73 keV energy band. The observed XRT count rates were converted into observed flux using the best fit spectral parameters. The BAT data (originally in the 14-150 keV band) were first extrapolated into the XRT 0.2-10 keV band using a conversion factor evaluated from the BAT best fit spectral model and then converted to rest frame.

The horizontal axis shows the time in seconds starting from the BAT trigger in the rest frame, obtained by applying the correction factor $1/(1+z)$ to the observer frame time. The gaps in the XRT-PC data correspond to the part of the orbit when the satellite was not observing this GRB.

The inset shows the first 80 seconds of the burst, with the excellent match between the XRT and the extrapolated BAT fluxes.

Lower and upper limits to the isotropic-equivalent radiated energy E_{iso} up to 300 seconds from the burst onset are obtained to be **6.6×10^{46} J** **3.2×10^{47} J**, respectively in the full 1-10^4 keV band.

The redshift of **6.29** translates to a distance of **13 billion light-years** from Earth, corresponding to a time when the Universe was just **700 million** to **750 million years** old.

[**Reference:** G. Cusumano *et al.*, "Detection of a huge explosion in the early Universe," astro-ph/0509737 (submitted to Nature).]

Models of Short-Duration GRBs

Colliding Binary Neutron Stars

Short GRBs (less than two seconds in duration) may be caused by mergers of binary systems with black holes or neutron stars. While uncertainty remains, most astrophysicists believe in either scenario a new black hole is born.

[from Chandra X-ray Observatory Photo Album]

Black Hole Devours a Neutron Star

Astrophysicists say they have seen tantalizing, first-time evidence of a black hole eating a neutron star-first stretching the neutron star into a crescent, swallowing it, and then gulping up crumbs of the broken star in the minutes and hours that followed.

[from Chandra X-ray Observatory Photo Album]

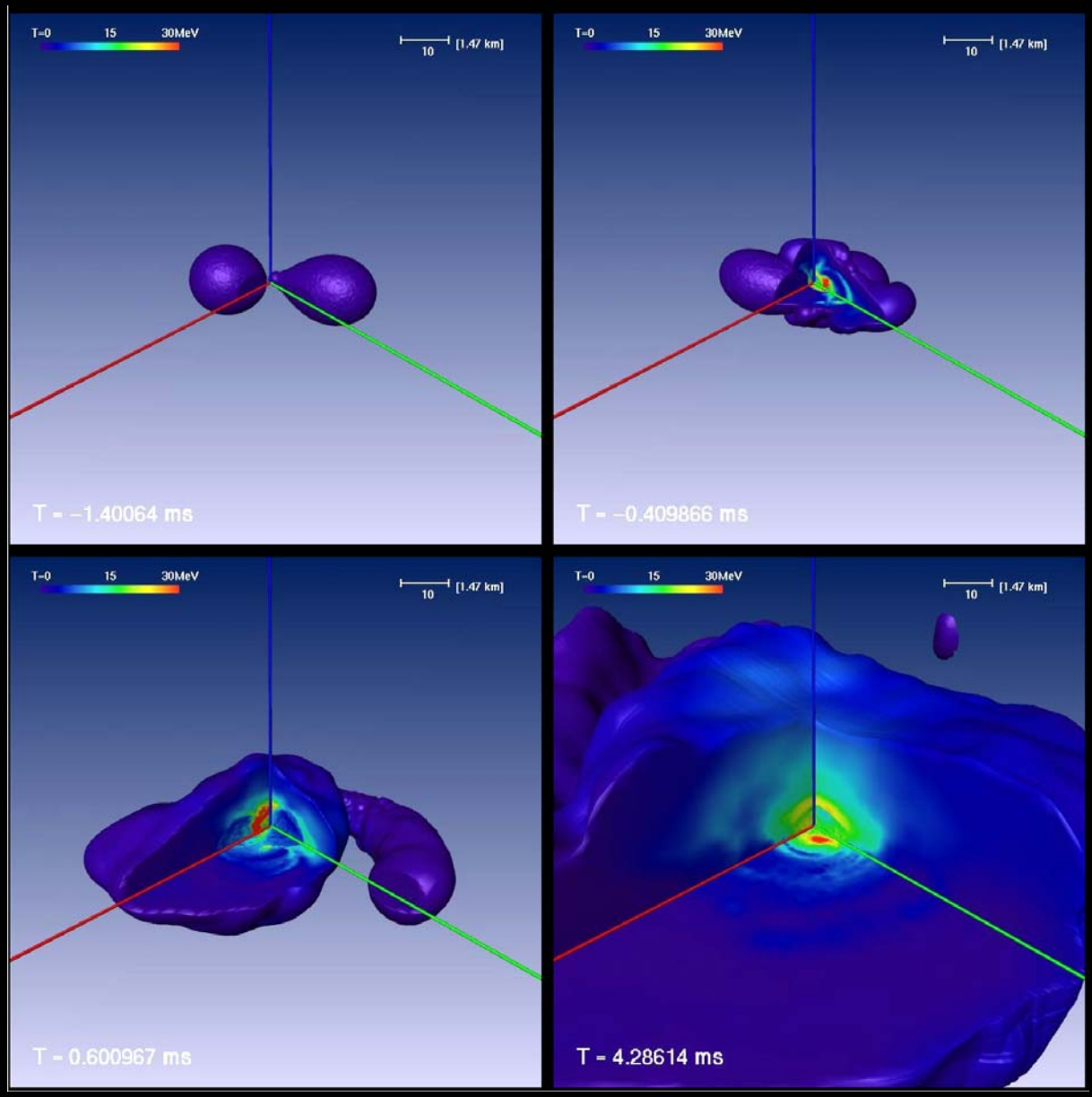

Four stages of the NS+NS merger Model S1216. The surface is chosen to correspond to a density of 10^{10} g/cm^3, the temperature distribution is visible color coded in the octant cut out from the 3-dimensional mass distribution. Temperatures up to 30 MeV are reached at the center only milliseconds after the two neutron stars have merged. Time is given in the lower left corner of the panels, and length is measured in units of 1.47 km (top right corner of each panel).

Upon colliding with each other, the two merging neutron stars heat up by shocks and compression to central temperatures of several 10 MeV. Within only a few milliseconds after the final plunge, the neutrino emission reaches luminosities of 10^{53} ergs/s or higher and the post-merger object should start losing mass in the neutrino-driven wind.

[**From** R. Oechslin and H.-Th. Janka, “Torus formation in neutron star mergers and well-localized short gamma-ray bursts,” astro-ph/0507099 (accepted by MNRAS).]

The energy range of our interest is
~100 MeV to (at least) 10 YeV

International System of Units (SI)

value	SI prefix	symbol
10	deca	da
10^2	hecto	h
10^3	kilo	k
10^6	mega	M
10^9	giga	G
10^{12}	tera	T
10^{15}	peta	P
10^{18}	exa	E
10^{21}	zetta	Z
10^{24}	yotta	Y

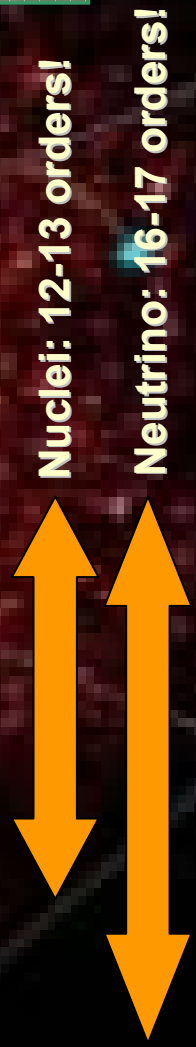

SEVERAL DEFINITIONS

One of the main characteristics of cosmic rays is their differential intensity = differential energy spectrum = differential flux:

$$F_a = \frac{dN_a}{dS dt d\Omega dE} \qquad \left([F_a] = \frac{\text{particles}}{\text{cm}^2 \cdot \text{s} \cdot \text{sr} \cdot \text{GeV}} \right).$$

So $dN_a = F_a dS dt d\Omega dE$ is the number of particles a with the total energies E to $E + dE$ which cross the area dS (perpendicular to the direction of observation) in time dt coming within the solid angle $d\Omega = d\varphi \sin\vartheta d\vartheta$.

In the general case, $F_a = F_a(E, \mathbf{\Omega}, \mathbf{r}, t) = F_a(\mathbf{p}, \mathbf{r}, t)$ with

$$\mathbf{\Omega} = (\sin\vartheta\cos\varphi, \sin\vartheta\sin\varphi, \cos\vartheta) = \frac{\mathbf{p}}{|\mathbf{p}|} = \frac{\mathbf{v}}{|\mathbf{v}|}$$

the unit vector directed along the particle momentum $\mathbf{p}$ (or velocity $\mathbf{v}$) and $\mathbf{r}$ the point of observation. But usually, for simplicity, we will write only the first argument.

The integral energy spectrum is defined by

$$F_a(>E) = \int_E^\infty F_a(E')dE'.$$

From this definition it follows that

$$F_a(E) = -\left[\frac{\partial F_a\,(>E)}{\partial E}\right].$$

Similar way one can define the differential and integral momentum spectra,

$$F_a(p) = \frac{dN_a}{dSdtd\Omega dp} \quad \text{and} \quad F_a\,(>p) = \int_p^\infty F_a(p')dp'$$

(where $p = |\mathbf{p}|$). These are related to the energy spectra as

$$F_a(p) = (p/E)F_a(E) \quad \text{and} \quad F_a(>p) = F_a(>E).$$

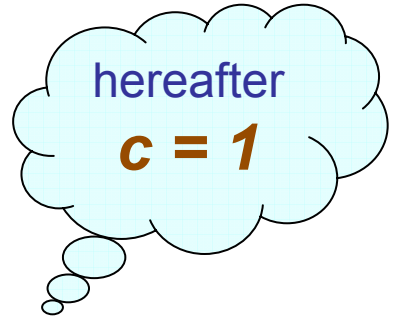

This immediately follows from the relation

$$pdp = EdE,$$

the consequence of the relativistic law $E^2 = p^2 + m_a^2$ (m_a is the mass of particle a).

In addition, one can introduce the differential and integral spectra

$F_a(E_\mathrm{k})$ and $F_a(>E_\mathrm{k})$, where $E_k \equiv E_\mathrm{kin} = E - m_a$ is the kinetic energy

and (for charged particles with the charge of $Z_a|e|$)

$F_a(R)$ and $F_a(>R)$, where $R = p/Z_a|e|$ is the magnetic rigidity ([R]=GV).

The flux of particles a whose differential intensity is $F_a(E)$ is defined by

$$\Phi_a\left(E,\Omega,\mathrm{r},t\right)=\int F_a\left(E,\Omega',\mathrm{r},t\right)\cos\vartheta d\Omega',$$

In particular, for an isotropic radiation from a semisphere, the flux is

$$\Phi_a(E)=\int_0^{\pi/2}F_a(E)\cos\vartheta\sin\vartheta d\vartheta=\pi F_a(E).$$

Note

since (for the isotropic radiation) the value of Φ_a is simply proportional to the F_a, the term flux is frequently used also for F_a, instead of the correct term differential intensity or differential spectrum. Sometimes this can be a source of confusions.

A Bird‘s Eye View of the All-particle CR Spectrum

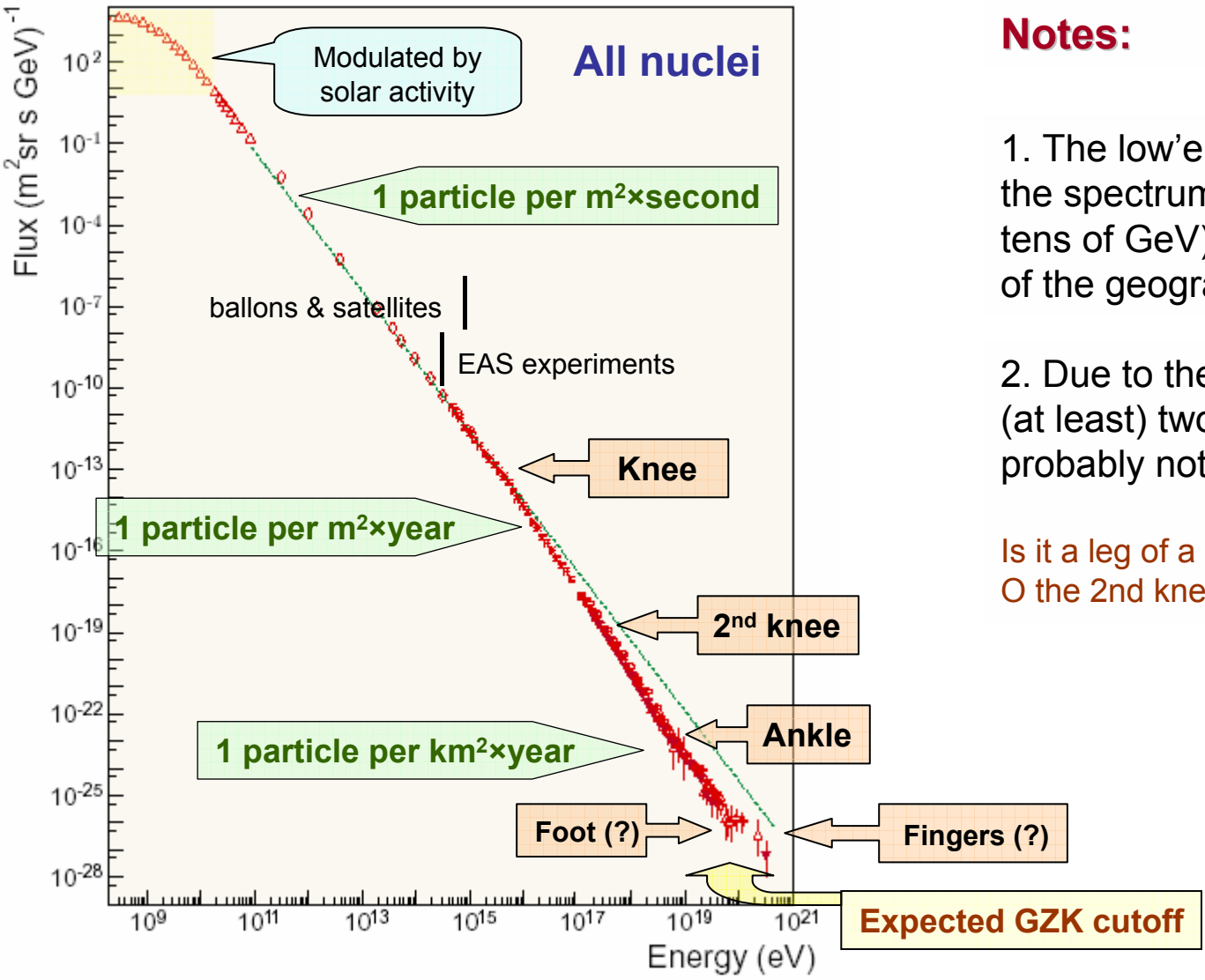

Notes:

1. The low’energy part of the spectrum (below some tens of GeV) is dependent of the geographycal position.

2. Due to the presence of (at least) two knees this is probably not a human leg.

Is it a leg of a bug?
O the 2nd knee is a bug?

UHECR Puzzles

(before HiRes & Auger)

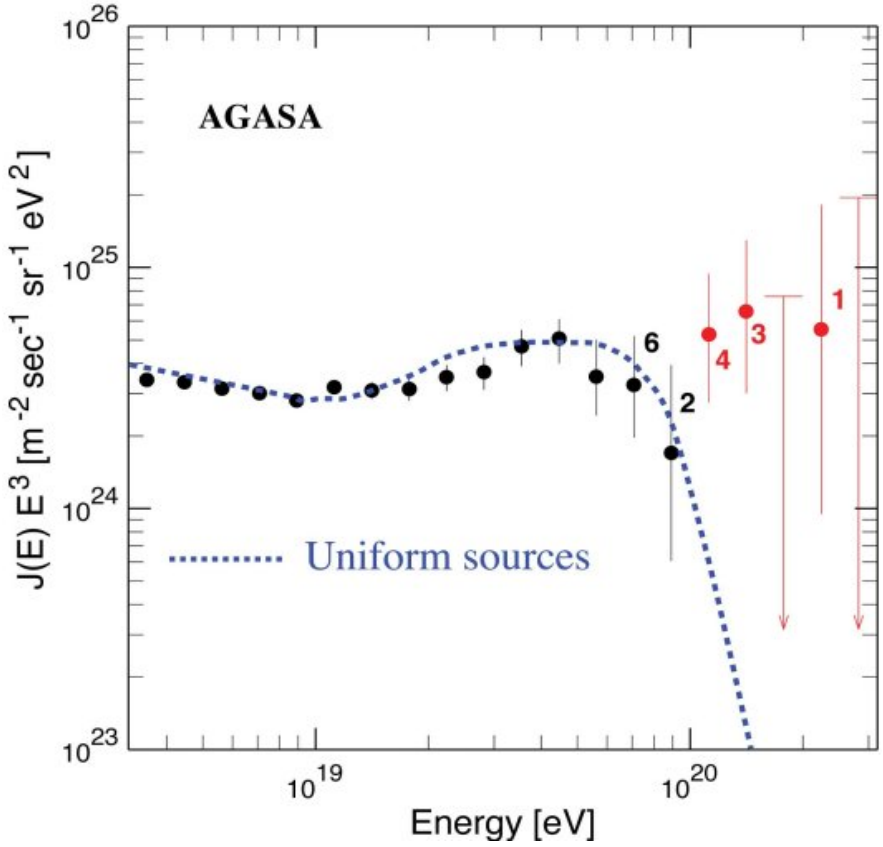

A zoom on the highest energy range of the cosmic ray spectrum (from the AGASA experiment). The dotted line shows the expected cutoff if the cosmic ray sources were uniformly distributed in the universe. The few events above the cutoff have no explanation as to their origin in the framework of conventional astrophysics.

There are a few observational facts to prove that the UHECR are indeed a mystery as of today.

- The fact that their sources (whatever they are) are expected to be in our close neighbourhood and yet we do not see them.

- That their energy is so huge that no conventional astrophysical acceleration mechanism seems capable of producing them;

- That during more than four decades of observation we did not succeed in giving them an identity (what kind of particles they are?).

One Piece of the Puzzle, the GZK feature

$p + \gamma \rightarrow n + \pi^+$

$p + \gamma \rightarrow p + \pi^\circ$

$(p + \gamma \rightarrow p + e^+ + e^-)$

Pion photoproduction

Greisen (1966), Zatsepin & Kuz'min (1966)

Pair production

(Blumenthal, 1970)

$A + \gamma \rightarrow (A-1) + N$

$A + \gamma \rightarrow (A-2) + 2N$

$(A + \gamma \rightarrow A + e^+ + e^-)$

Photodisintegration

(Puget *et al.,* 1976)

Pair production

(Blumenthal, 1970)

As an example, if the largest energy cosmic ray ever detected (320 EeV, i.e. more that 50 joules!) was a proton produced with an initial energy of 10 ZeV, the distance of its source should be less than 50 Mpc (roughly 150 millions of light-years). Although such a distance may look enormous, at cosmological scales it is more or less the size of the local super-cluster of galaxies, i.e. the "suburbs" of the Milky Way.

Cosmic Microwave Background

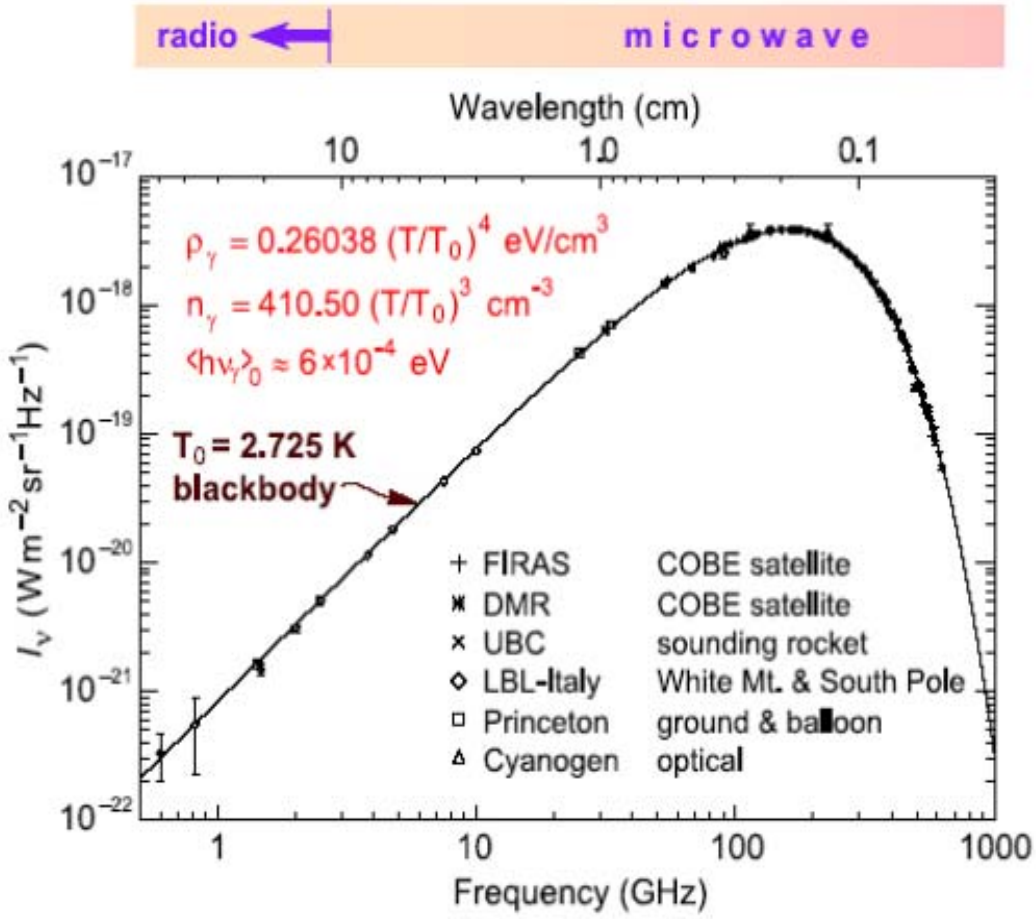

Solar velocity with respect to CMB is 369.3 ± 2.5 km/s.

Precise measurements of the CMB (= CBR = RR) spectrum. The line represents a 2.73 K blackbody (present-day value), which describes the spectrum very well, especially around the peak of intensity. The spectrum is less well constrained at 10 cm and longer wavelengths.

When you tune your TV set between channels, *a few percent* of the "snow" that you see on your screen is noise caused by the background of microwaves.

GZK Kinematics

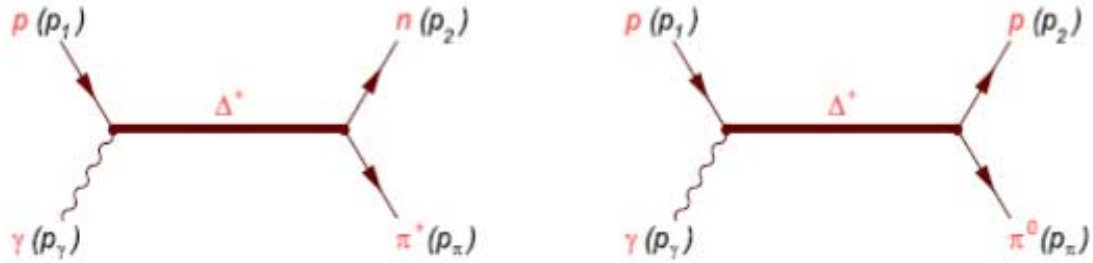

The reaction threshold can be found from the condition

$$s = (p_1 + p_\gamma)^2 = m_p^2 + 2E_\gamma \left(E_1 - P_1 \cos\theta\right) \geq (p_2 + p_\pi)^2_{\min} = (m_p + m_\pi)^2 .$$

The minimum occures for head-on collisions ($\cos\theta = -1$). Neglecting $\mathcal{O}\left(m^2/E_1^2\right)$ contributions yields

$$E_1 > \frac{2m_p m_\pi + m_\pi^2 + m_N^2 - m_p^2}{4E_\gamma} \simeq \frac{m_\pi \left(m_p + m_\pi/2\right)}{2E_\gamma}.$$

Therefore, taking $\langle h\nu_\gamma \rangle = 6 \times 10^{-4}$ eV (CMB) we have

$$E_{\text{th}} \simeq \begin{cases} 1.13 \times 10^{20} \ \dfrac{\langle h\nu_\gamma \rangle}{E_\gamma} \text{ eV} & \text{for} \quad p\gamma \to n\pi^+ \\ 1.17 \times 10^{20} \ \dfrac{\langle h\nu_\gamma \rangle}{E_\gamma} \text{ eV} & \text{for} \quad p\gamma \to p\pi^0. \end{cases}$$

Gamma-Ray Absorption by CMB (GSJ cutoff)

Similar way one can find the thereshold for $\gamma\gamma_{\rm CMB} \to e^+e^-$ [R. J. Gould & G. P. Schréder (1966), J. V. Jelley (1966)]:

$$E_{\rm th} = \frac{m_e^2}{E_\gamma} \simeq 4.35 \times 10^{14} \, \frac{\langle h\nu_\gamma \rangle}{E_\gamma} \ {\rm eV}.$$

The total cross section is well known:

$$\sigma_{\gamma\gamma} = \frac{1}{2}\pi r_0^2 (1-v^2) \left[(3-v^4) \ln\left(\frac{1+v}{1-v}\right) - 2v(2-v^2) \right],$$

where $r_0 = e^2/m_e$ is the classical electron radius and v is the electron (and positron) velocity in the center-of-mass system. The differential CMB photon density at energy ϵ and angle θ is (for an isotropic distribution)

$$dn = \frac{1}{2} n(\epsilon) \sin\theta d\epsilon d\theta, \quad \text{where} \quad n(\epsilon) = \frac{\epsilon^2}{\pi^2 \left(e^{\epsilon/kT} - 1\right)}.$$

Then the absorption probability per unit path length is

$$\frac{d\tau_{\rm abs}}{dx} = \int\int \frac{1}{2} \sigma_{\gamma\gamma} n(\epsilon)(1-\cos\theta) d\epsilon d\cos\theta,$$

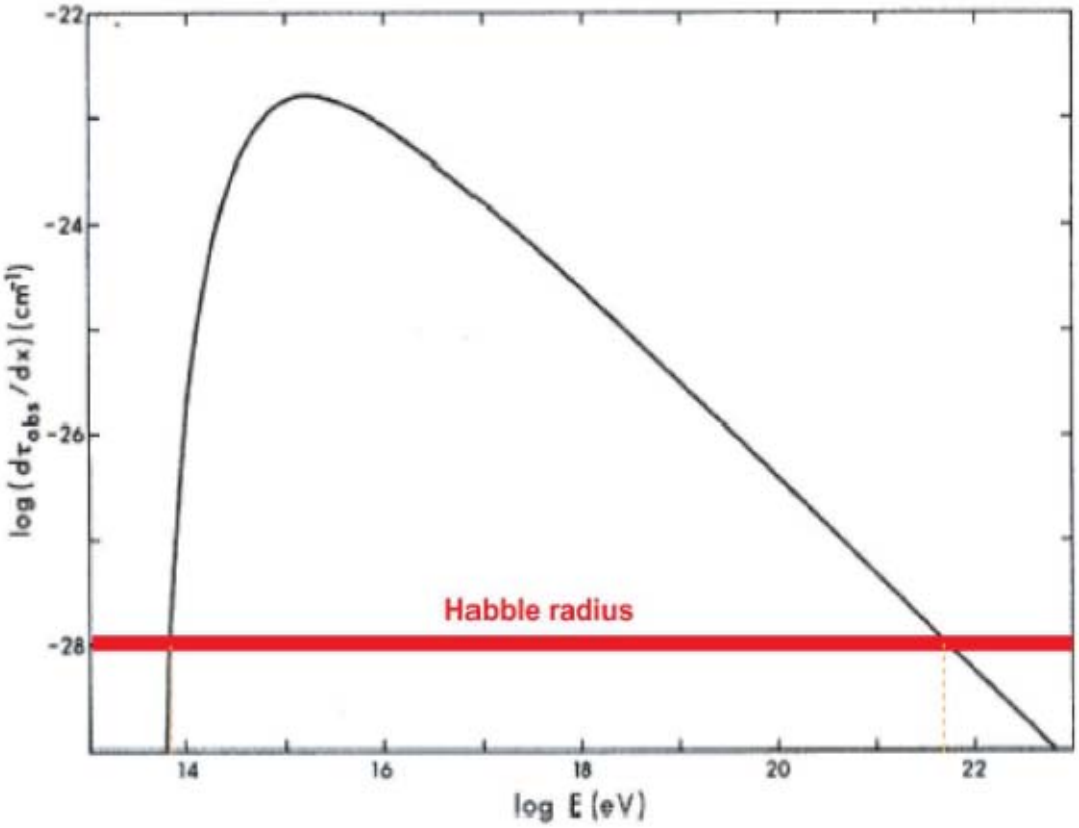

It is seen that the absorption probability is greater than the reciprocial of the "Hubble radius" or "radius of the Universe" for $10^{14} \lesssim E \lesssim 10^{22}$ eV. For photons in this energy range, the absorption optical depth to the edge of the Universe would be > 1.

That is, we could "see" only out to a distance $d \sim (d\tau_{\text{abs}}/dx)^{-1}$ in the Universe.

Note: The figure[a] is a bit obsolete since (a) it has been calculated for $T = 3.5\ K$ and (b) it takes no account for the readshift. However the qualitative result remains the same.

[a] Borrowed from R. J. Gould & G. P. Schréder, "Opacity of the universe to high-energy photons," Phys. Rev. Lett. **16** (1966) 252-254.

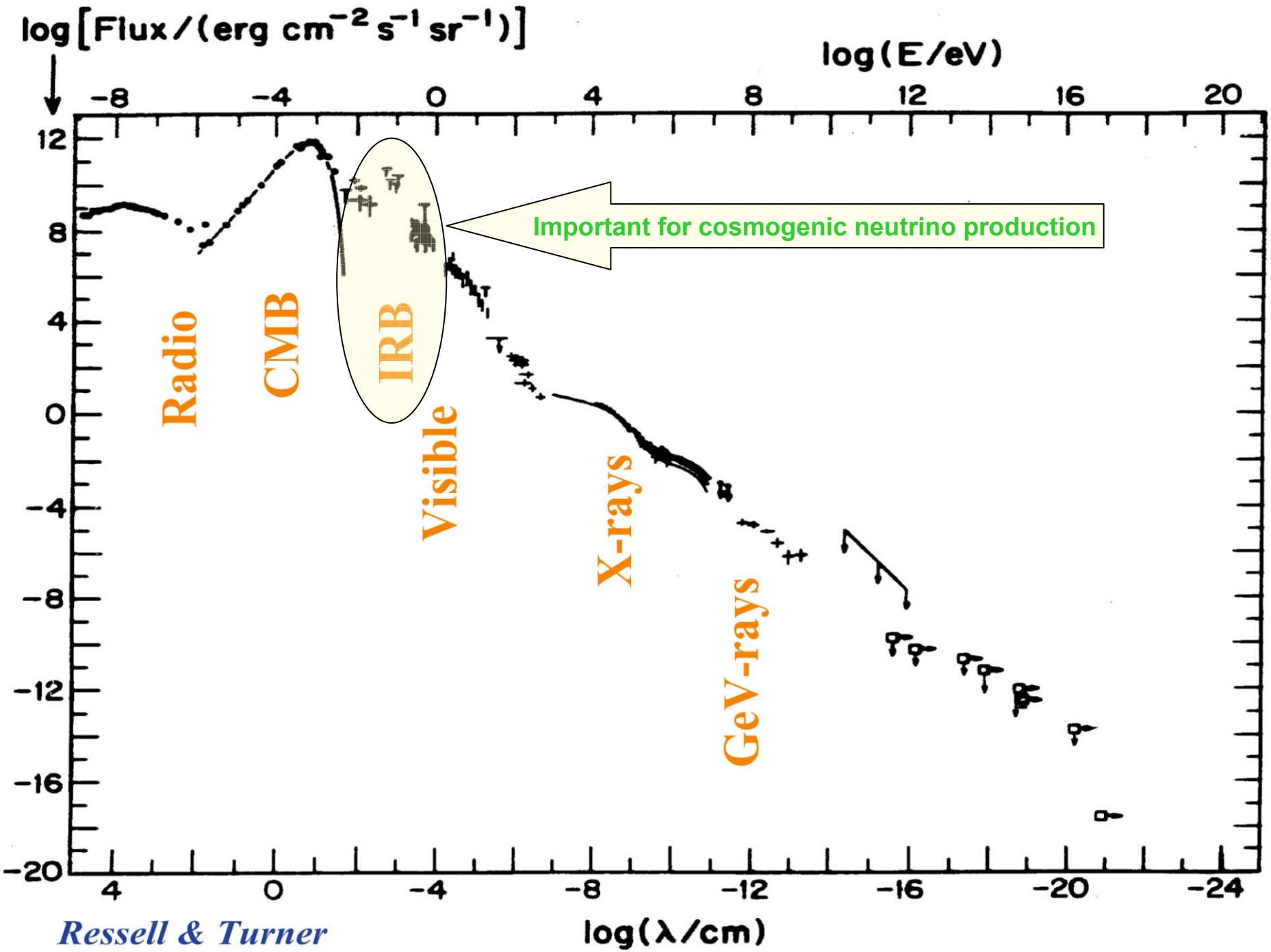
log [Flux / (erg cm^{-2} s^{-1} sr^{-1})]
log (E/eV)
-8
-4
0
4
8
12
16
20
12
8
4
0
-4
-8
-12
-16
-20
Radio
CMB
IRB
Visible
X-rays
GeV-rays
Important for cosmogenic neutrino production
4
0
-4
-8
-12
-16
-20
-24
log (λ/cm)
Ressell & Turner

Cosmic Infrared Background

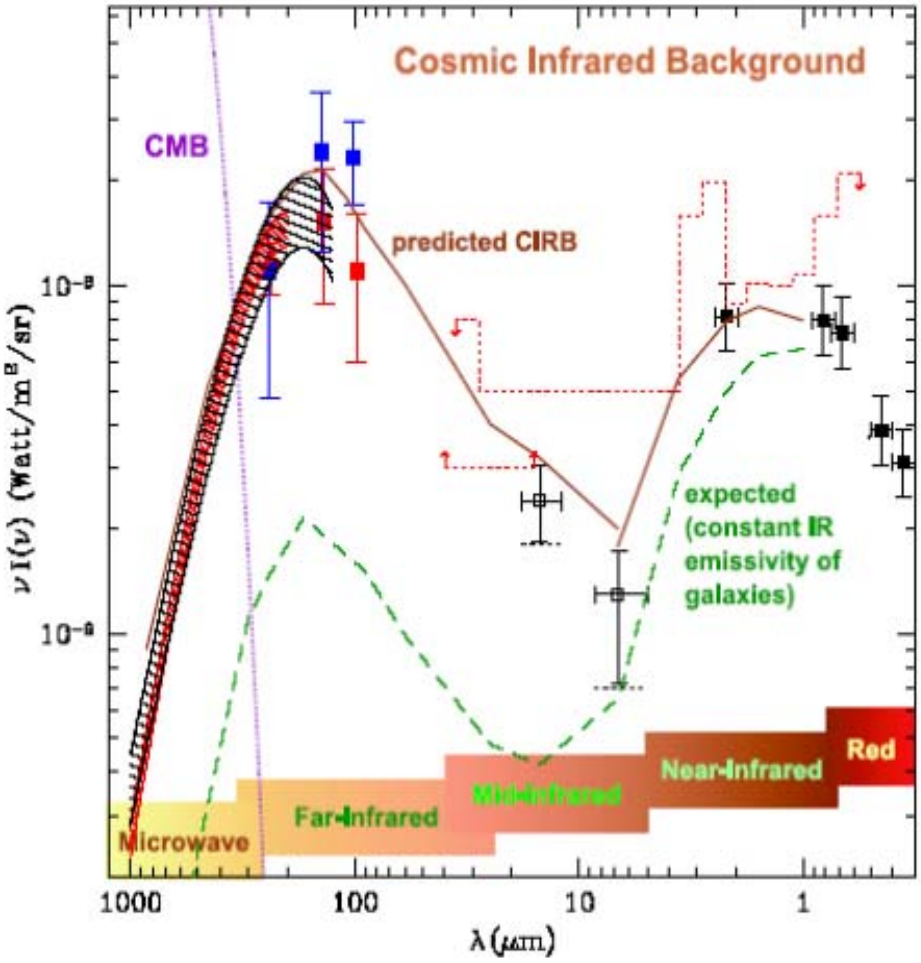

The CIRB spectrum as measured by independent groups in the all-sky COBE maps, compared with estimates of the optical extragalactic background based on ultradeep optical integrations by the Hubble Space Telescope. The dashed histograms are limits set by TeV cosmic opacity measurements. The lower dashed line is the expected intensity based on the assumption that the IR emissivity of galaxies does not change with cosmic time. The thick line is the predicted CIRB spectrum of a model for IR galaxy evolution.

[From A. Franceschini *et. al.*, "A long-wavelength view on galaxy evolution from deep surveys by the infrared space observatory," astro-ph/0108292.]

Optical view of the Galactic Center

[From Howard McCallon]

The Galaxy taken by the COBE satellite as a composite of Far-IR wavelengths of 60, 100, and 240 μm. The Galactic Center shines brightly in the Far-IR because of the thick concentration of stars embedded in dense clouds of dust. These stars heat up the dust and cause it to glow.

[From Michael Hauser, COBE/DIRBE Sci. Team & NASA]

Near-IR view of the Galactic Center

[from the 2 Micron All Sky Survey "2MASS"]

Spectral Region	Wavelength Range (μm)	Temperature Range (K)	What we see
Near-Infrared	**(0.7-1) to 5**	**740 to (3,000-5,200)**	• Cooler red stars • Red giants • Dust is transparent
Mid-Infrared	**5 to (25-40)**	**(92.5-140) to 740**	• Planets, comets, asteroids • Dust warmed by starlight • Protoplanetary disks
Far-Infrared	**(25-40) to (200-350)**	**(10.6-18.5) to (92.5-140)**	• Emission from cold dust • Central regions of galaxies • Very cold molecular clouds

[From IPAC, NASA , URL: http://www.ipac.caltech.edu/Outreach/Edu/Regions/irregions.html]

Cosmic X-ray & γ-ray Backgrounds

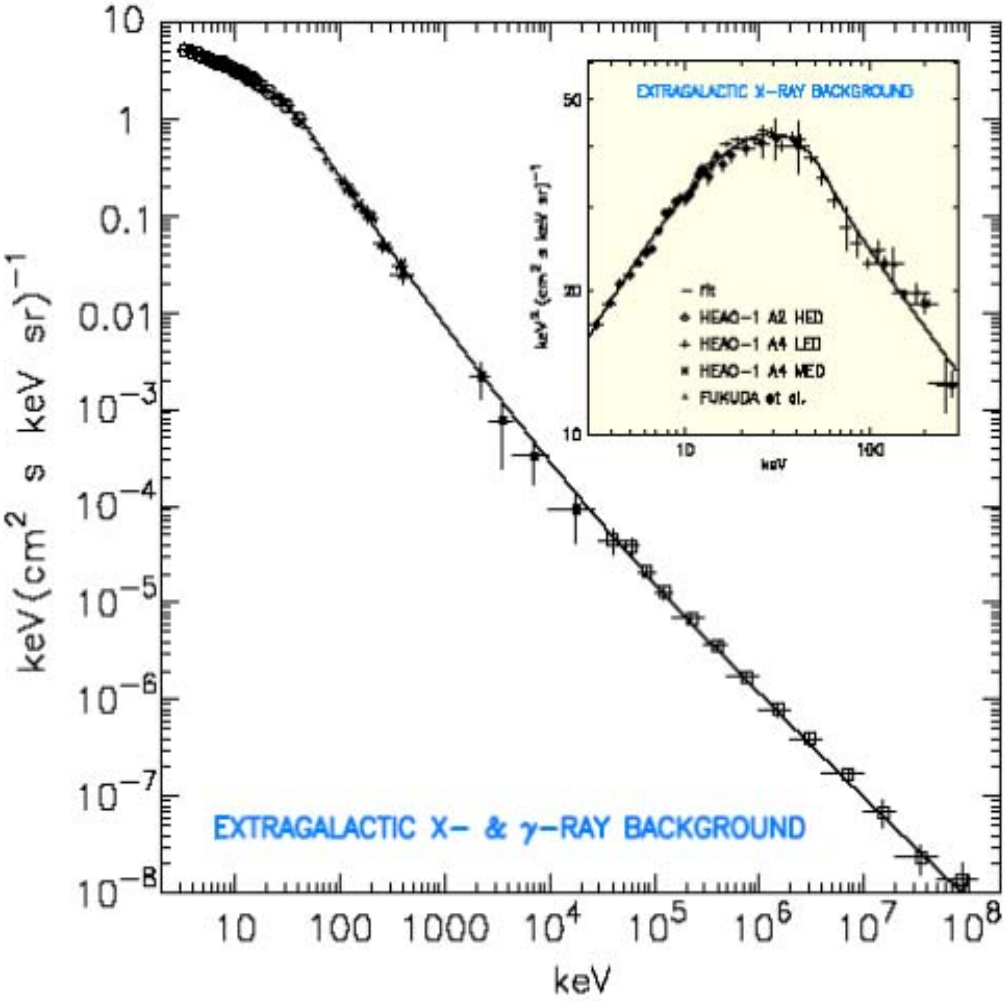

Selected results on the intensity spectrum of the diffuse cosmic component over the 3 keV to 100 GeV range. The results are fitted to simple empirical exponential and power-law functions. The reduced χ^2 of the fit is about 1.3, over almost eight decades of photon energy. Various source classes and physical processes are postulated to dominate in different spectral ranges. Comptel and Egret data are marked with filled and open squares, respectively. The data in inset are multiplied with energy.

[From D. E. Gruber *et. al.*, "The spectrum of diffuse cosmic hard X-rays measured with HEAO-1," ApJ **520** (1999) 124 (astro-ph/9903492).]

List of explanations (very incomplete)

- Origin in nearby (z<0.01) Seyfert galaxies.
- Origin in distant radio galaxy jets and hot spots.
- Origin in colliding galaxy systems.
- Origin in large-scale structures (pancakes, filaments, flow shocks to clusters of galaxies)
- Links with (cosmological) gamma-ray bursts.
- Microquasars, magnetars, quark novae.
- Photons, electrons and nucleons initiated by UHE cosmic neutrinos on relic neutrino background (Z-bursts).
- Decay of metastable superheavy relic particles trapped in the Galactic halo (long-lived neutralinos, etc.).
- UHE SUSY candidates (gluinos, glubolinos, neutralinos, shadrons, sgoldstionos, etc.).
- Evaporation of primordial black holes.
- Decay of topological defects (monopoles, vortons, cosmic strings, necklaces, etc.) created in the early Universe, crypton decays.
- Topological defects themselves as UHECR particles.
- Space-time's unseen dimensions, KK-modes, branes, and all that.
- Lorentz symmetry violations with anomalous kinematics, modified dispersion relation from q-deformed noncommutative theory.
- Other exotica and science fiction:
  - Stranglets / quark nuggets / nuclearities;
  - New hadrons, uchecrons, superbaryons made of color sextet quarks;
  - WIMPZILLAs and other superheavy relic X particles (X-bursts);
  - Photon-Axion mixing (for UHE photons);
  - Non-linearity in quantum mechanics, discrete space, quasi-static Universe,…

Z-bursts resulting from the resonant annihilation of ultrahigh-energy cosmic neutrinos on relic antineutrinos are among proposed wittily explanations of the UHECR puzzle.

This solution has the same drawback as the explanation of the origin of life by panspermia…

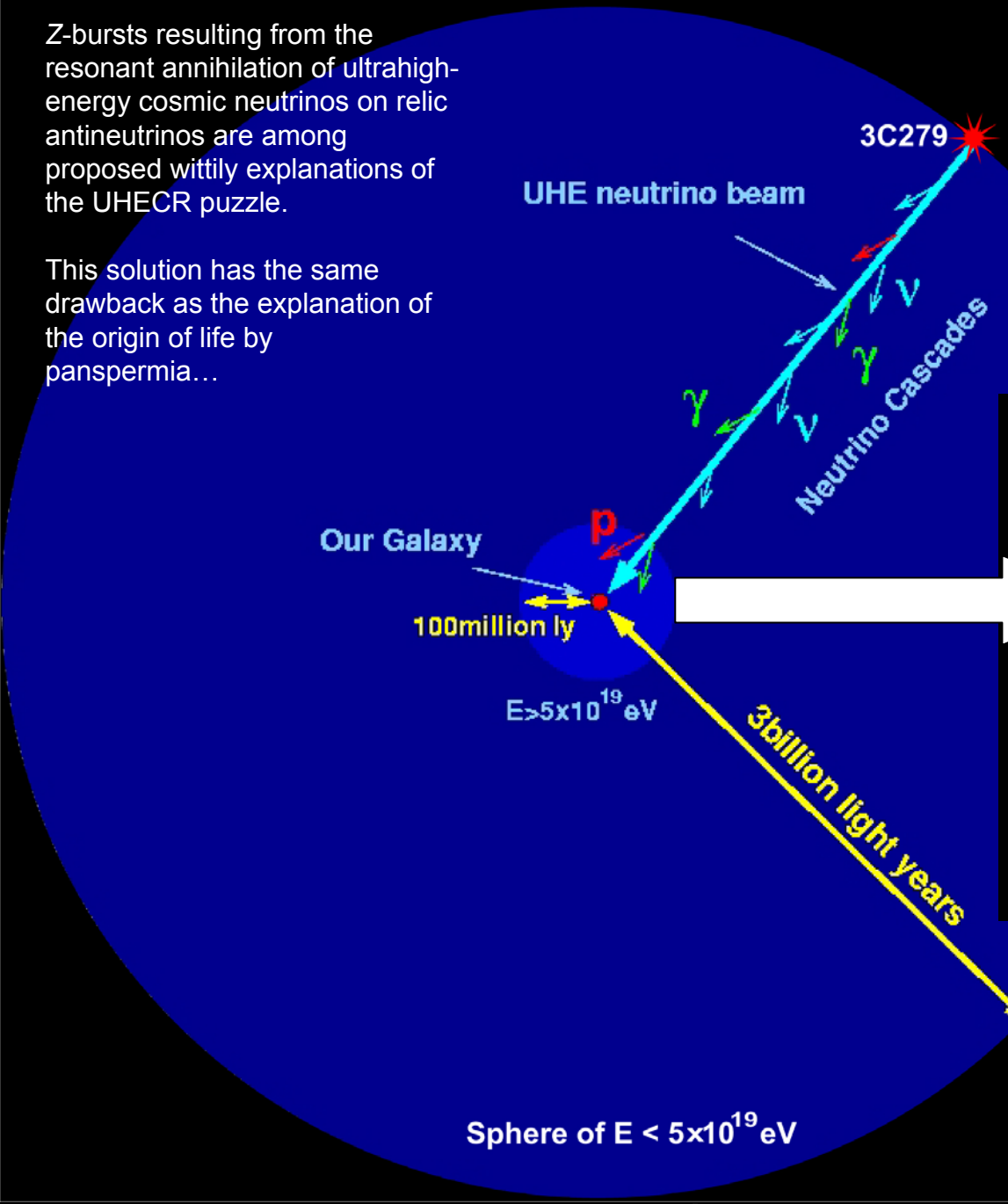

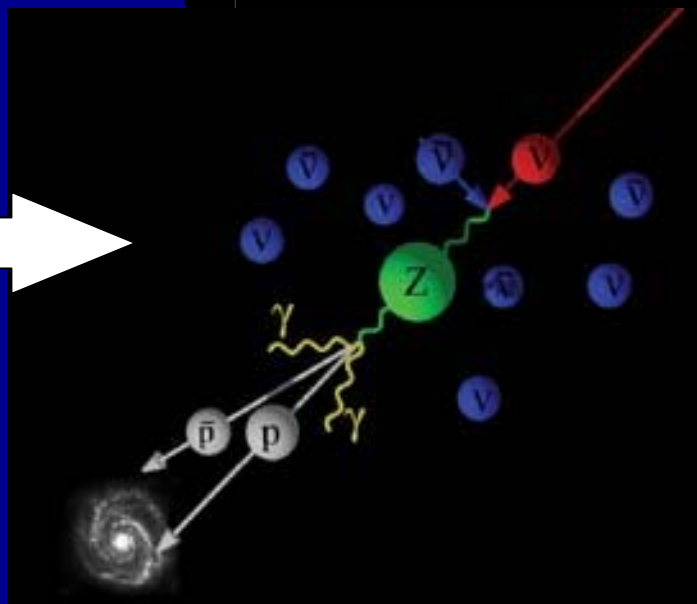

Note: **3C279** (a.k.a. *3C 279*) a gamma-ray quasar, is one of the few known blazars in existence. It is located at a redshift of $z = 0.5362$.

The name signifies that it was the 279th object (ordered by right ascension) of the Third Cambridge Catalog of Radio Sources (**3C**), published in 1959.

It seems the gale subsided

after HiRes and after Pierre Auger

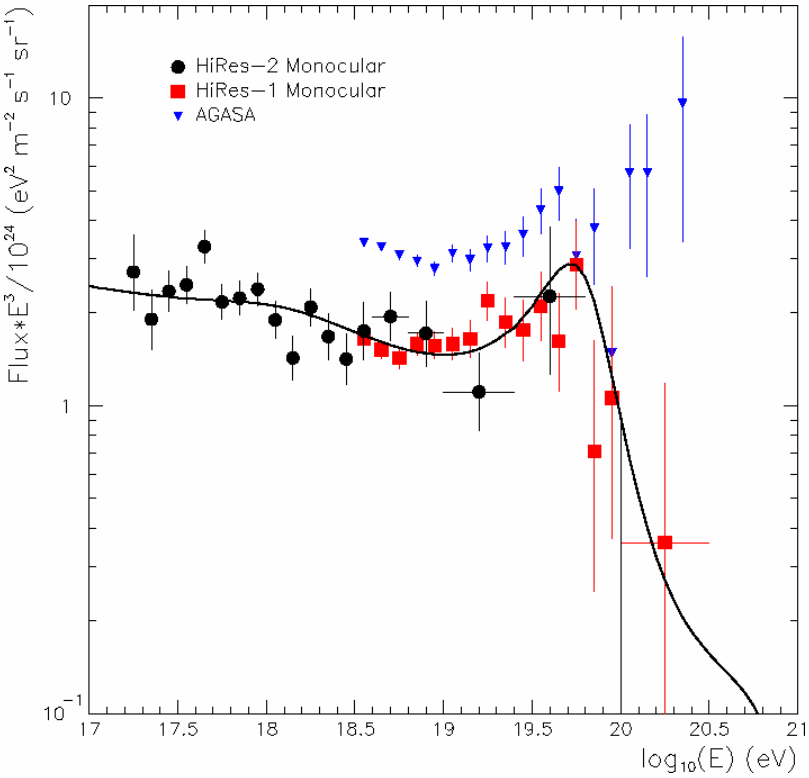

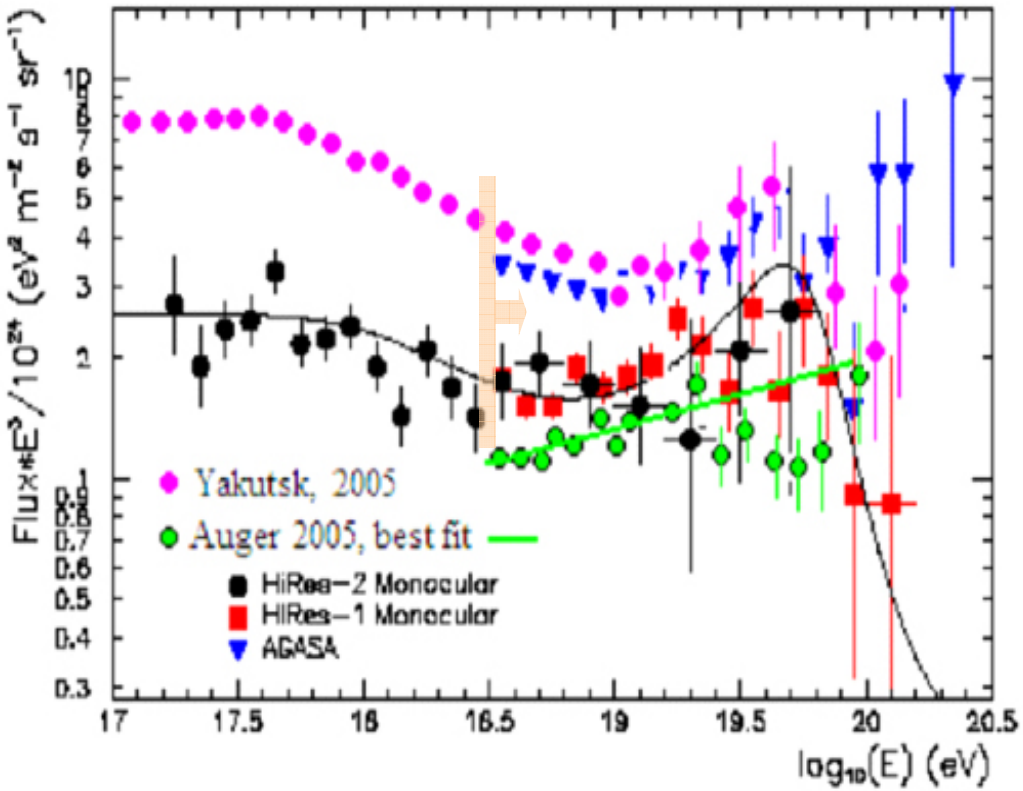

Number of events above 3 EeV:

Yakutsk – 1303 **Auger – 3525**
AGASA – 7000 **HiRes I – 1616**

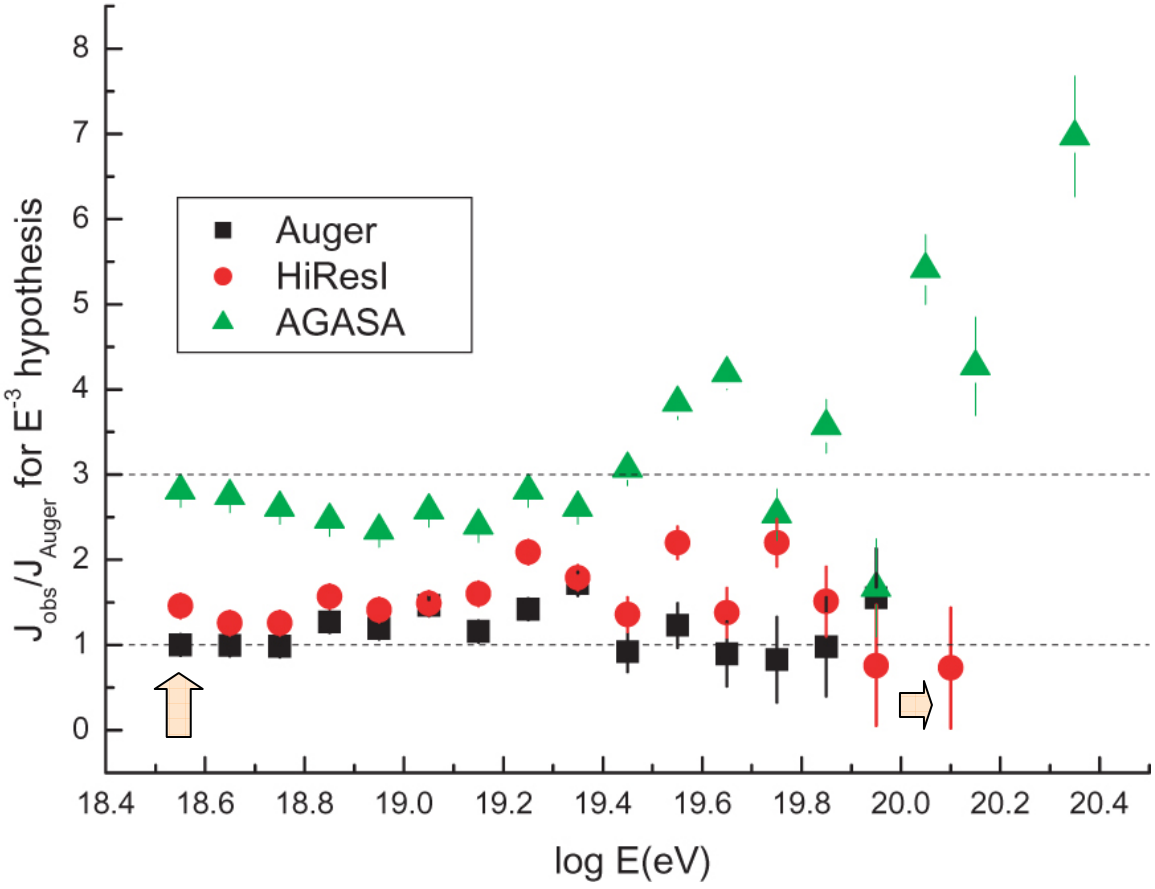

The ratio of the values of each point with respect to a fit of E^{-3} to the first point of the **Auger** spectrum at **3.55 EeV** which contains **1216 events**.

The purpose of the plot is to illustrate the differences between the different measurements in a straight-forward manner.

Yakutsk data are not included in this plot as they are so discordant (see previous slide).

The differences between the fluorescence measurements by **Auger** and **HiRes I** are relatively small except at the highest energies where the **Auger** statistics are presently too low to comment on the flux above 100 EeV.

The difference between **AGASA** and the fluorescence measurements probably arises, at least in part, because of the mass and hadronic model assumptions.

[**Reference:** A.A. Watson, "Observations of Ultra-High Energy Cosmic Rays," a talk given at 9th International Conference on Astroparticle & Underground Physics ("TAUP 2005"), Zaragoza, September 10-14, 2005 (astro-ph/0511800).]

One surprise from ultra-high energy

All particles, including meson and baryon resonances, become (quasi)stable.
Does our extrapolation of known physics of particle interactions remain correct in the UHE region?

Particle	Mass, m (MeV/c^2)	Mean life, τ (s)	$c\tau$ (cm)	Decay length at E = 100 EeV
n **(neutron)**	939.6	8.857×10^{2}	2.655×10^{13} (1.775 au)	2.826×10^{24} cm (0.916 Mpc)
μ (muon)	105.7	2.197×10^{-6}	6.586×10^{4}	6.234×10^{16} cm (4167 au)
τ (tauon)	1777	2.906×10^{-13}	8.711×10^{-3}	4.902×10^{8} cm (4902 km)
D^+	1869	1.051×10^{-12}	3.150×10^{-2}	1.685×10^{9} cm (16,851 km)
$\rho(770)$	771	9.82×10^{-20} (Γ= 149.2 MeV)	2.944×10^{-9}	382 cm
$\Delta(1232)$	1232	7.9×10^{-20} (Γ= 120 MeV)	2.368×10^{-9}	192 cm

1 au = 149 597 870 660 m, 1 pc = 1 au/(1 arc sec) = 3.085 677 580 7 × 10^{16} m = 3.262 ly

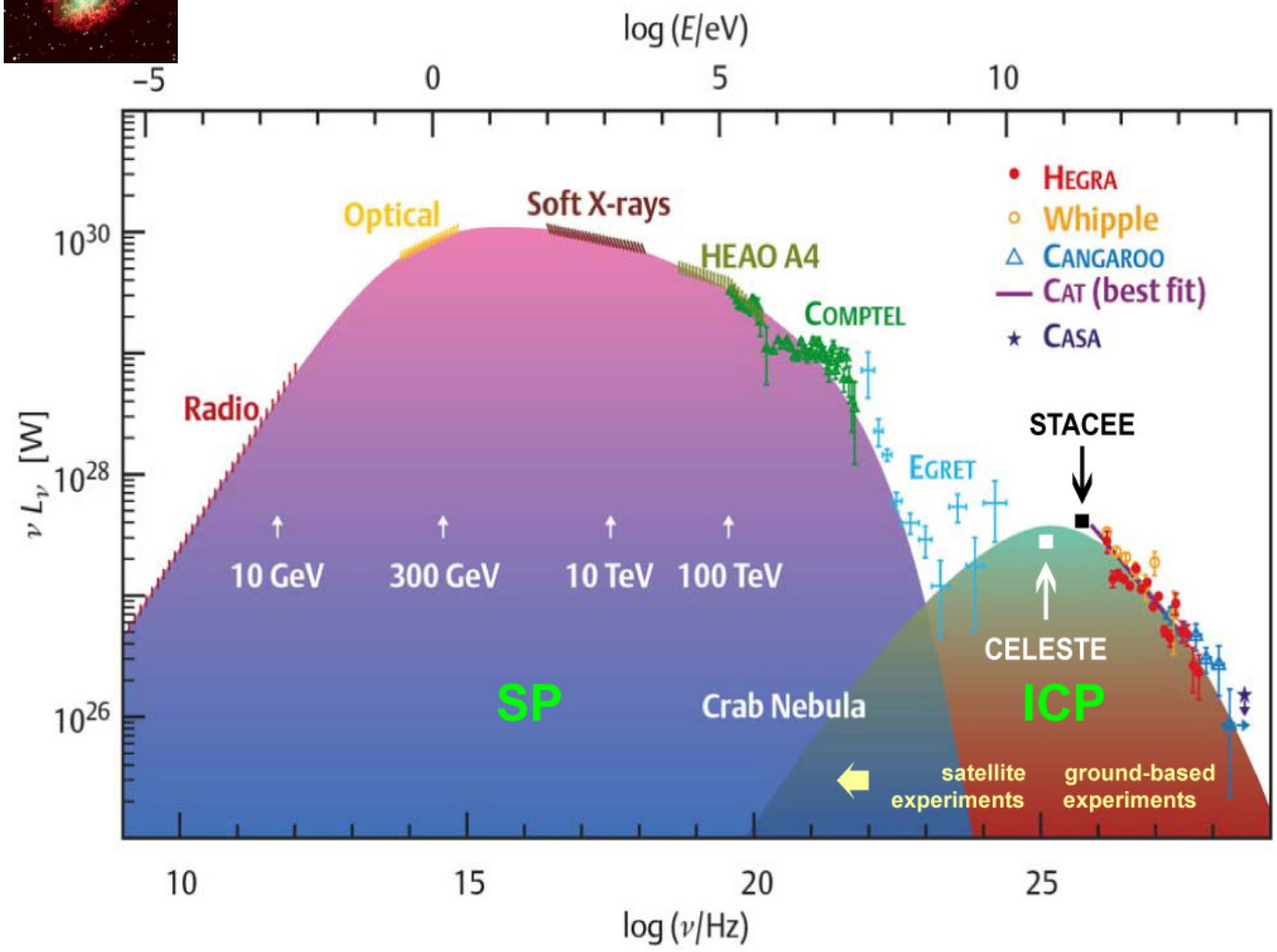

Spectral energy distribution of the unpulsed electromagnetic emission from the Crab Nebula.
(Two recent data points from CELESTE and STACEE measurements are added to the original figure.)

[From von H. Völk, "Gamma-Astronomie mit abbildenden Cherenkov-Teleskopen," Sterne und Weltraum **38** (1999) 1064-1070; see also F.A. Aharonian and A.M. Atoyan, "Nonthermal Radiation of the Crab Nebula," astro-ph/9803091.]

Wide-range spectrum from the Crab nebula shows two peaks, **SP** and **ICP**, which are interpreted as **synchrotron emission** from high energy electrons and **inverse Compton scattering** of synchrotron photon by the same electrons.

The electron energies producing the dominant SP at lower energies are indicated by the arrows. The Compton Gamma Ray Observatory (CGRO) telescopes COMPTEL and EGRET determine the synchrotron fall-off and the transition to the ICP expected at some tens of GeV and indicated by the Cherenkov telescope measurements.

The gap between the satellite and ground-based experiments are now being filled by Cherenkov telescopes using large-area solar power collectors.

Composite image of the Crab Nebula by the Chandra X-ray Observatory showing
- X-ray (in blue),
- optical (in green), and
- radio (in red)

images superimposed. The inner blue ring is about one light year across.

From the Chandra Photo Album, URL: http://chandra.harvard.edu/photo/index.html

The energetic nonthermal particles of the very compact pulsar near the center of this object generate the nebula and the diffuse continuum of synchrotron emission. The size of the X-ray image is smaller those of optical and radio. This is because the higher energy X-ray emitting electrons radiate away their energy more quickly than the lower energy radio and optically emitting electrons as they move.

Contribution of nearby Pulsars to CR observed at Earth

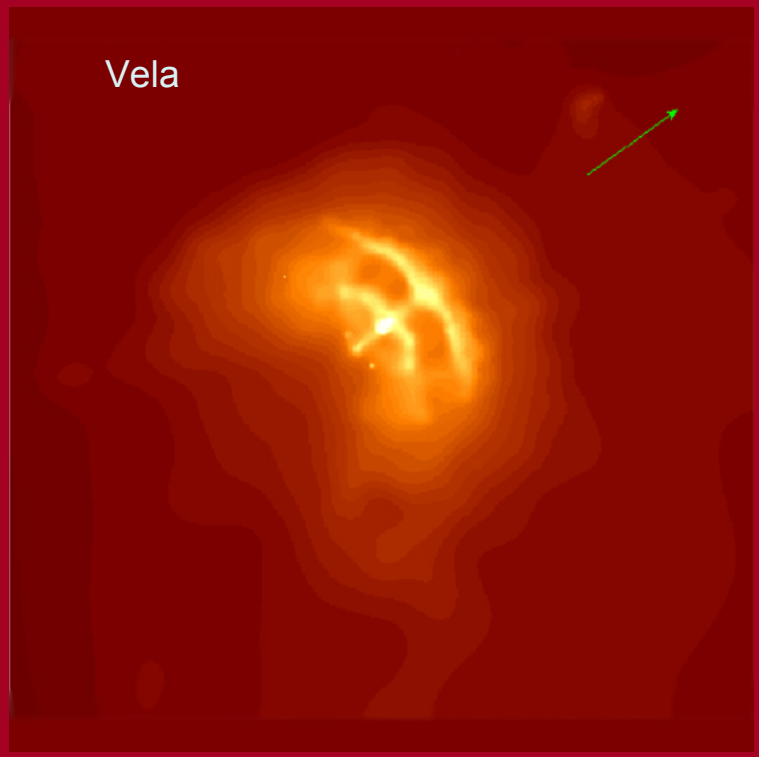

Vela (X-ray image) was found by SAS-2 as the brightest object in the gamma-ray sky. It is comparatively close to the Earth and so the surrounding nebula is well studied. Its characteristic age is around 10,000 years with periodicity P = 89.3 ms, slow down rate is dP/dt = 1.25×10^{-13}, and the surface magnetic field is around 3.4×10^{12} Gauss. The distance of the object from the Earth is around 500 pc though recent works suggest a smaller value of 300 pc.

[From http://heasarc.gsfc.nasa.gov/]

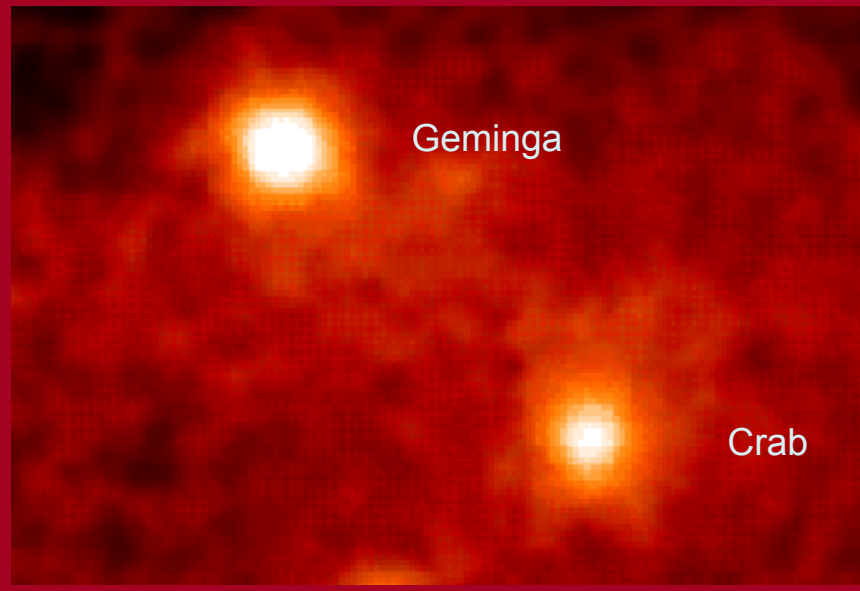

Geminga or PSR J0633+1746 (Gamma-ray image) discovered by the SAS-2 group and later confirmed by the COS-B group, about 150 pc away from the Earth. Its radial velocity is unknown, but if it were 200 km/s, it could have been within 100 pc of Earth at 340,000 years ago. Geminga is a unique object: a highly compressed, spinning neutron star which does not emit radio waves like the other well-known pulsars. Yet it is a powerful source of pulsating gamma-rays and X-rays. Geminga is now known to be a rotation-powered pulsar with period P = 0.237 s, dP/dt = 1.0975×10^{-14}, and surface magnetic field B = 1.6×10^{12} Gauss.

[From http://antwrp.gsfc.nasa.gov/]

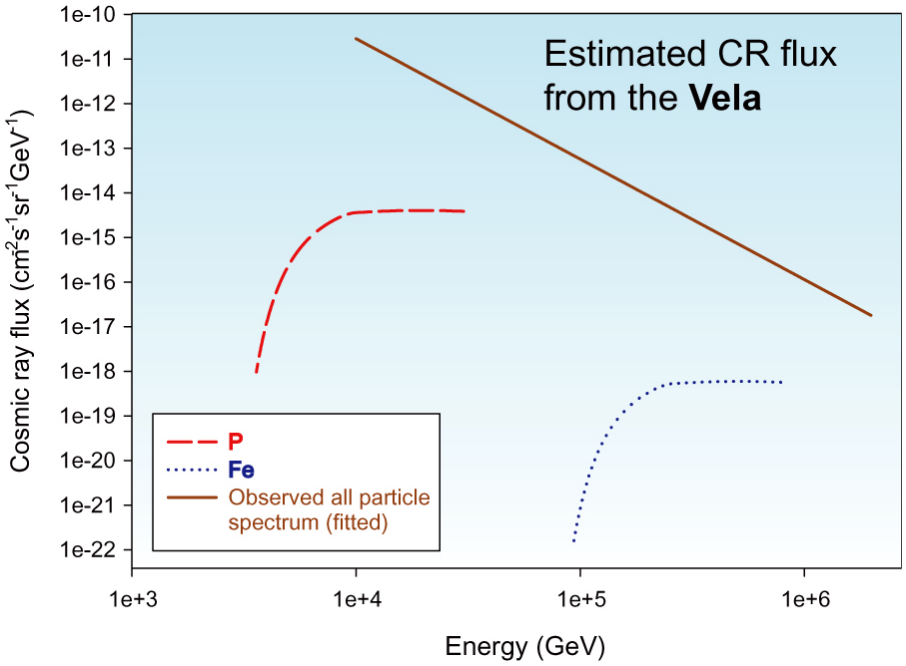

The maximum energy estimated:
~$3Z\times10^{13}$ eV.

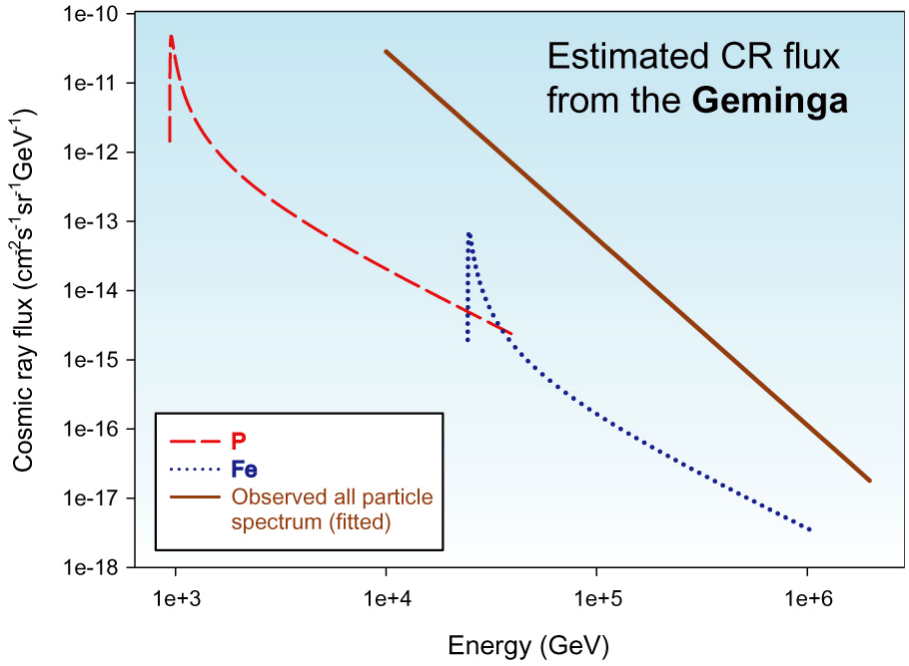

The maximum energy estimated:
~$4Z\times10^{13}$ eV.

[**Reference:** A. Bhadra, “Contribution of a nearby Pulsar to Cosmic Rays observed at Earth,” Astropart. Phys. 25 (2006) 226-232 (astro-ph/0602301).]

Observational data on Primary CR Spectrum

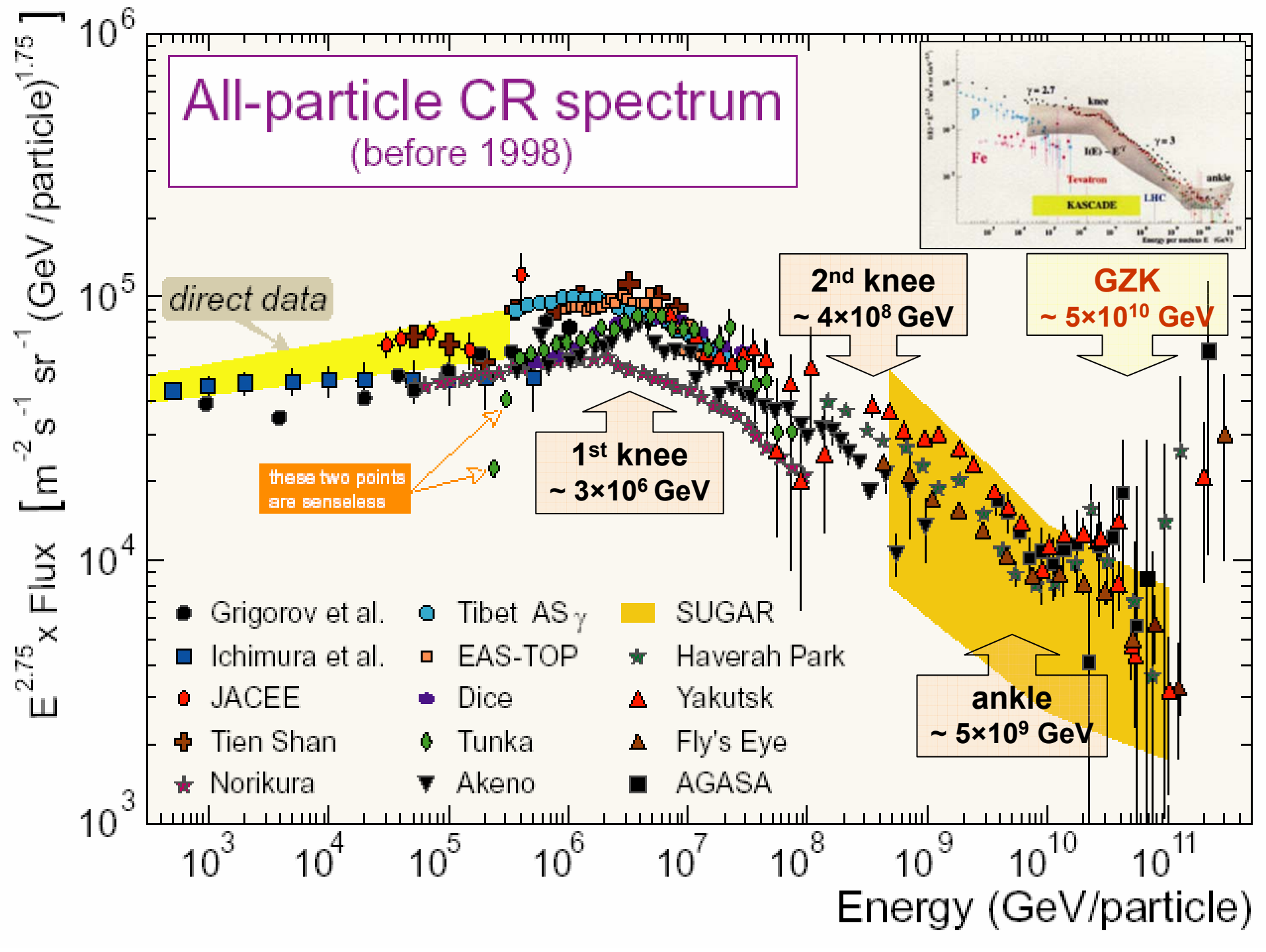
All-particle CR spectrum
(before 1998)
direct data
these two points are senseless
1st knee
~ 3×10^6 GeV
2nd knee
~ 4×10^8 GeV
GZK
~ 5×10^10 GeV
ankle
~ 5×10^9 GeV
Grigorov et al.
Ichimura et al.
JACEE
Tien Shan
Norikura
Tibet AS γ
EAS-TOP
Dice
Tunka
Akeno
SUGAR
Haverah Park
Yakutsk
Fly's Eye
AGASA
E^2.75 x Flux [m^-2 s^-1 sr^-1 (GeV /particle)^1.75]
Energy (GeV/particle)
γ = 2.7
knee
γ = 3
ankle
p
Fe
Tevatron
LHC
KASCADE

All-particle Spectrum 2005

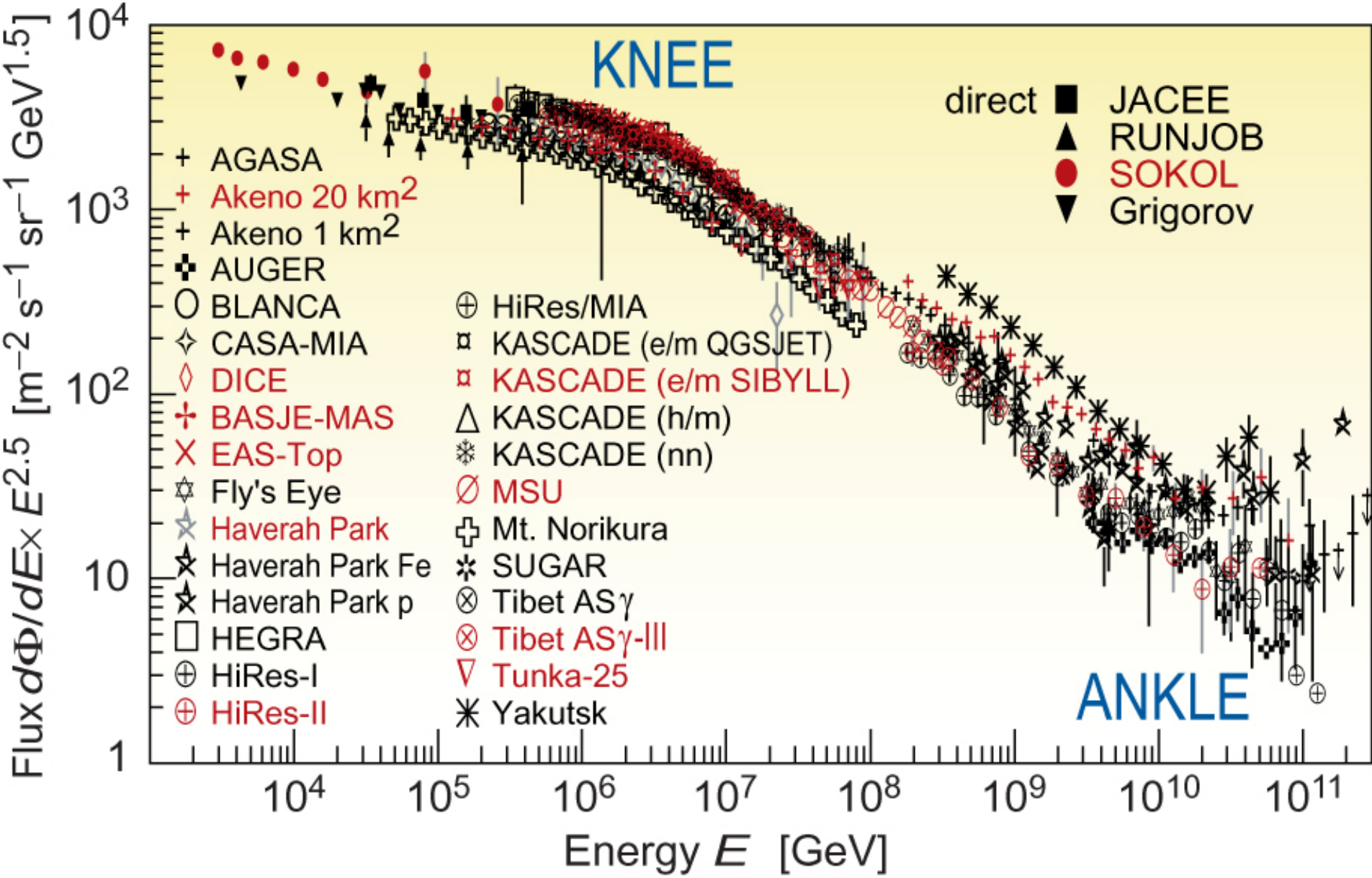

CR composition at low energies

Particle abundances in CR (at E > 2.5 GeV/particle, minimum SA) and in Universe

Nuclear group	Particle charge, Z	Integral Intensity in CR ($m^{-2}\ s^{-1}\ sr^{-1}$)	Number of particles per 10^4 protons	
			CR	Universe
Protons	1	1300	10^4	10^4
Helium	2	94	720	1.6×10^3
L	3-5	2	15	10^{-4}
M	6-9	6.7	52	14
H	10-19	2	15	6
VH	20-30	0.5	4	0.06
SH	>30	10^{-4}	10^{-3}	7×10^{-5}
Electrons	-1	13	100	10^4
Antiprotons	-1	>0.1	5	?

The abundances of primary CR is essentially different from the standard abundances of nuclei in the Universe. The difference is biggest for the light nuclear group **L** (Li, Be, B).

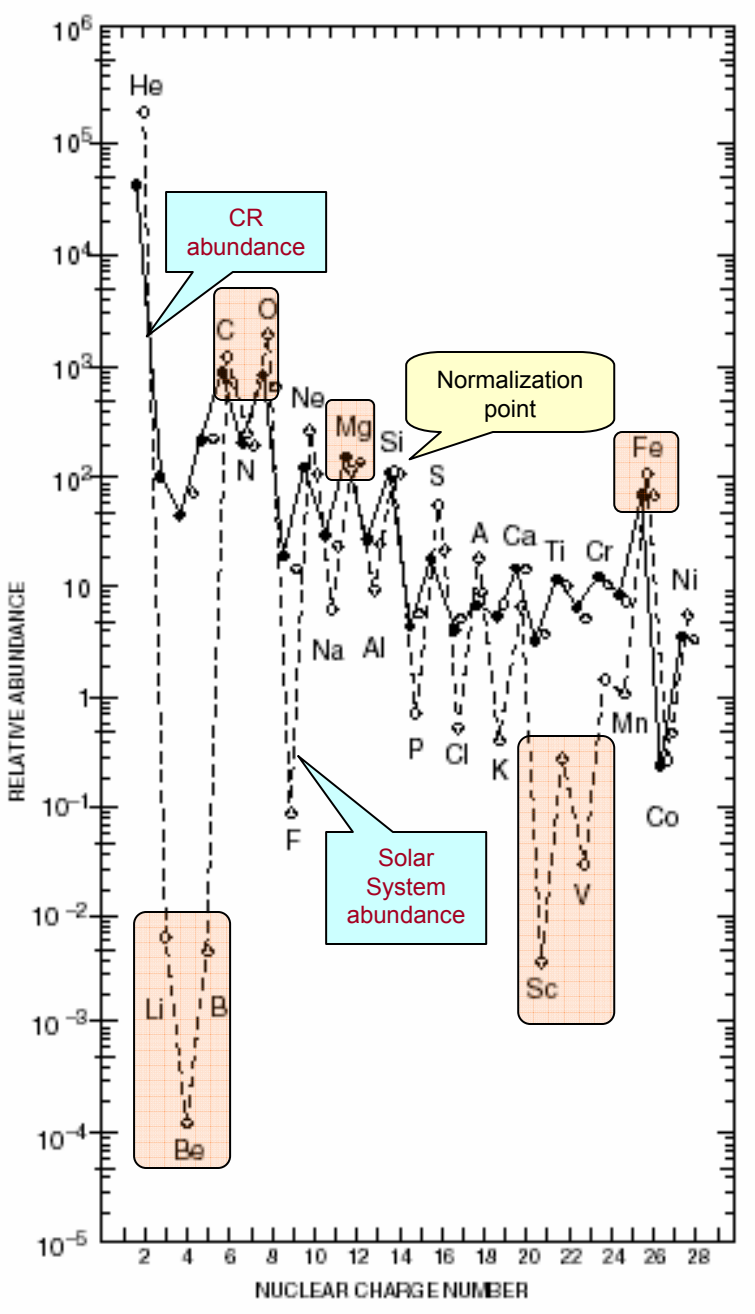

Over the charge region Z=1–28 (H–Ni), CR experiments in space can resolve the individual elements over an extended energy range. A summary of these data shows the relative abundance of CR at ~1 AU (solid line) along with the Solar System abundance (dashed line) for two different energy regimes, 70–280 MeV/nucleon and 1–2 GeV/nucleon. All abundances are normalized at one for silicium (**Si**) and the later is taken to be 100.

[**Reference:** J.A. Simpson, Ann. Rev. Nucl. Part. Sci. **33** (1983) 323.]

• Hydrogen (**H**) and helium (**He**) are the dominant elements, constituting some 98% of the CR ions, but are still under-abundant in the CR relative to the Solar System abundance.

• There is reasonably good agreement between the CR and Solar System abundance data for most of the even elements particularly for carbon (**C**), oxygen (**O**), magnesium (**Mg**) and iron (**Fe**).

• The light elements lithium (**Li**), beryllium (**Be**) and boron (**B**) as well as scandium (**Sc**) and vanadium (**V**) in the sub-iron region are greatly over-abundant when compared to the Solar System abundance. This is a result of nuclear spallation in interstellar space by nuclei of higher charge. The secondary nuclei generated by these reactions with the interstellar gas will have essentially the same velocity as the incident primary nuclei and hence the same energy per nucleon. Their energy spectra tend to be steeper than those of the primaries due to energy-dependent escape of the higher-energy primaries from the Galaxy.

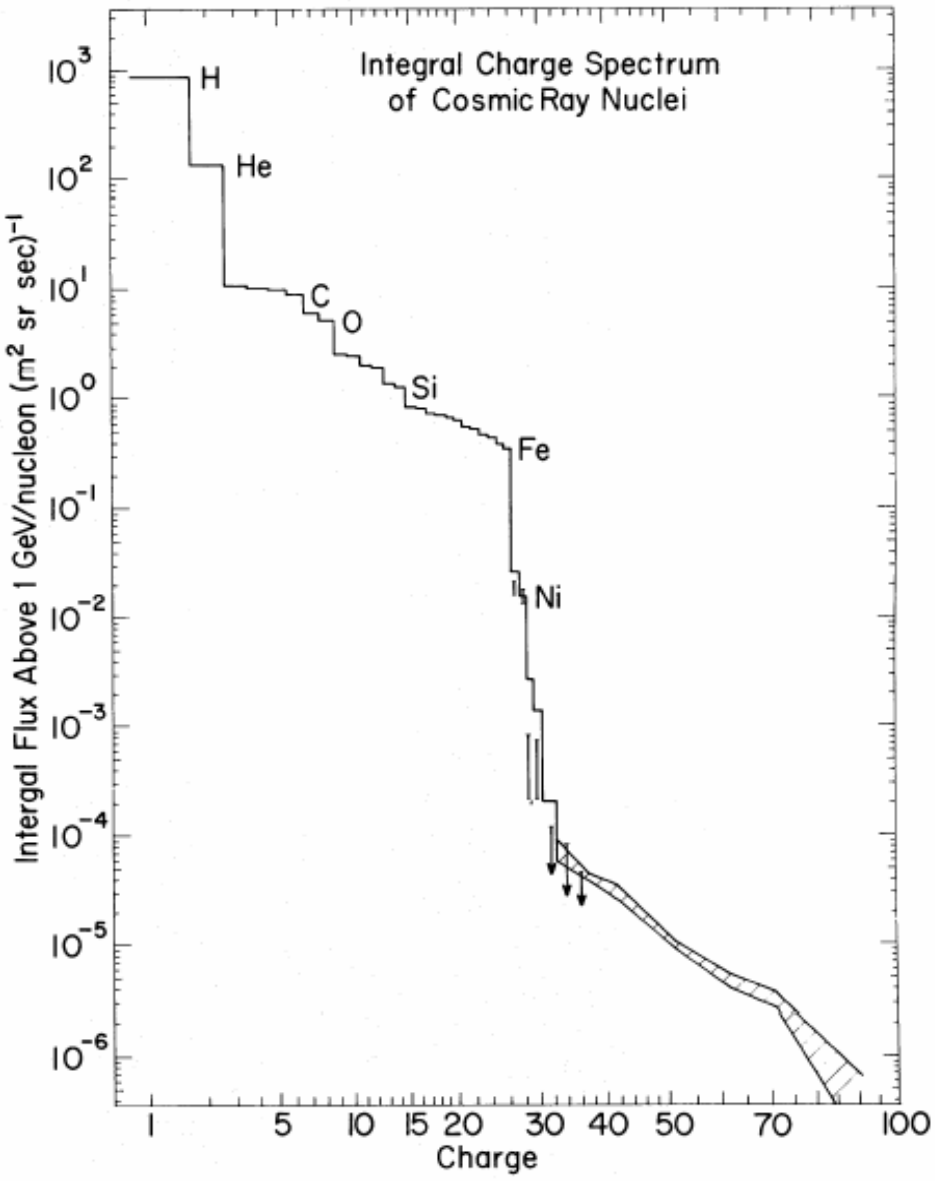

The integral charge spectrum of CR nuclei having energies > 1 GeV/nucleon.

[**Reference**: E. Juliusso and P. Meyer, ApJ **201** (1975) 76.]

Z	Element	F	Z	Element	F
1	H	540	13–14	Al-Si	0.19
2	He	26	15–16	P-S	0.03
3–5	Li-B	0.40	17–18	Cl-Ar	0.01
6–8	C-O	2.20	19–20	K-Ca	0.02
9–10	F-Ne	0.30	21–25	Sc-Mn	0.05
11–12	Na-Mg	0.22	26–28	Fe-Ni	0.12

Relative abundances F of cosmic-ray nuclei at 10.6 GeV/nucleon normalized to oxygen (=1). The oxygen differential flux at kinetic energy of 10.6 GeV/nucleon is 3.26 10^{-6} cm^{-2} s^{-1} sr^{-1} (GeV/nucleon)$^{-1}$.

[**Reference**: T.K. Gaisser & T. Stanev, “Cosmic rays,” pages 228-234 of the Review of Particle Physics, Phys. Lett. B **592** (2004) 1.]

The Sun in short
(photospheric features, sunspot cycle, etc.)

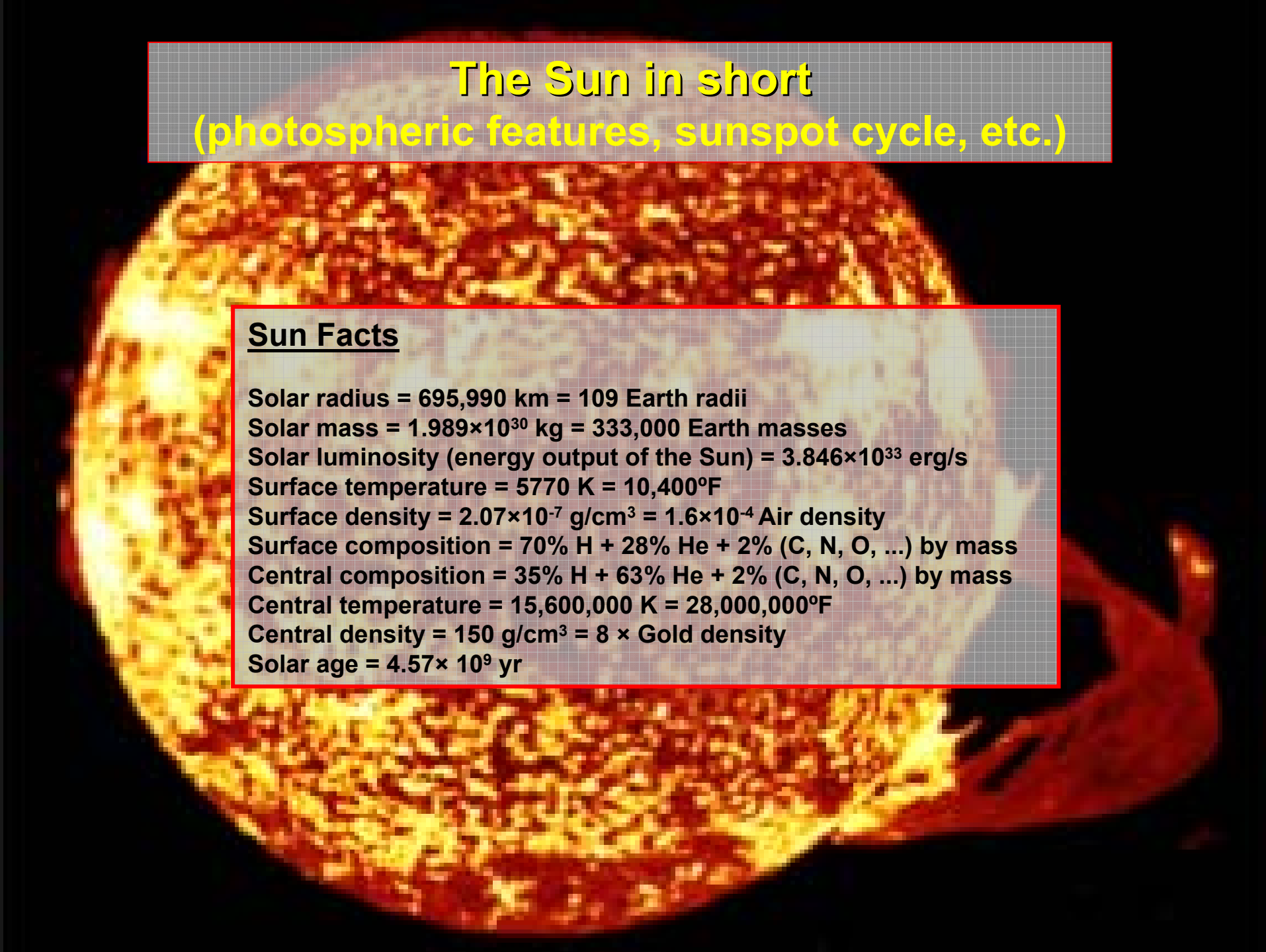

Sun Facts

Solar radius = 695,990 km = 109 Earth radii
Solar mass = 1.989×10^{30} kg = 333,000 Earth masses
Solar luminosity (energy output of the Sun) = 3.846×10^{33} erg/s
Surface temperature = 5770 K = 10,400ºF
Surface density = 2.07×10^{-7} g/cm^3 = 1.6×10^{-4} Air density
Surface composition = 70% H + 28% He + 2% (C, N, O, ...) by mass
Central composition = 35% H + 63% He + 2% (C, N, O, ...) by mass
Central temperature = 15,600,000 K = 28,000,000ºF
Central density = 150 g/cm^3 = 8 × Gold density
Solar age = 4.57×10^9 yr

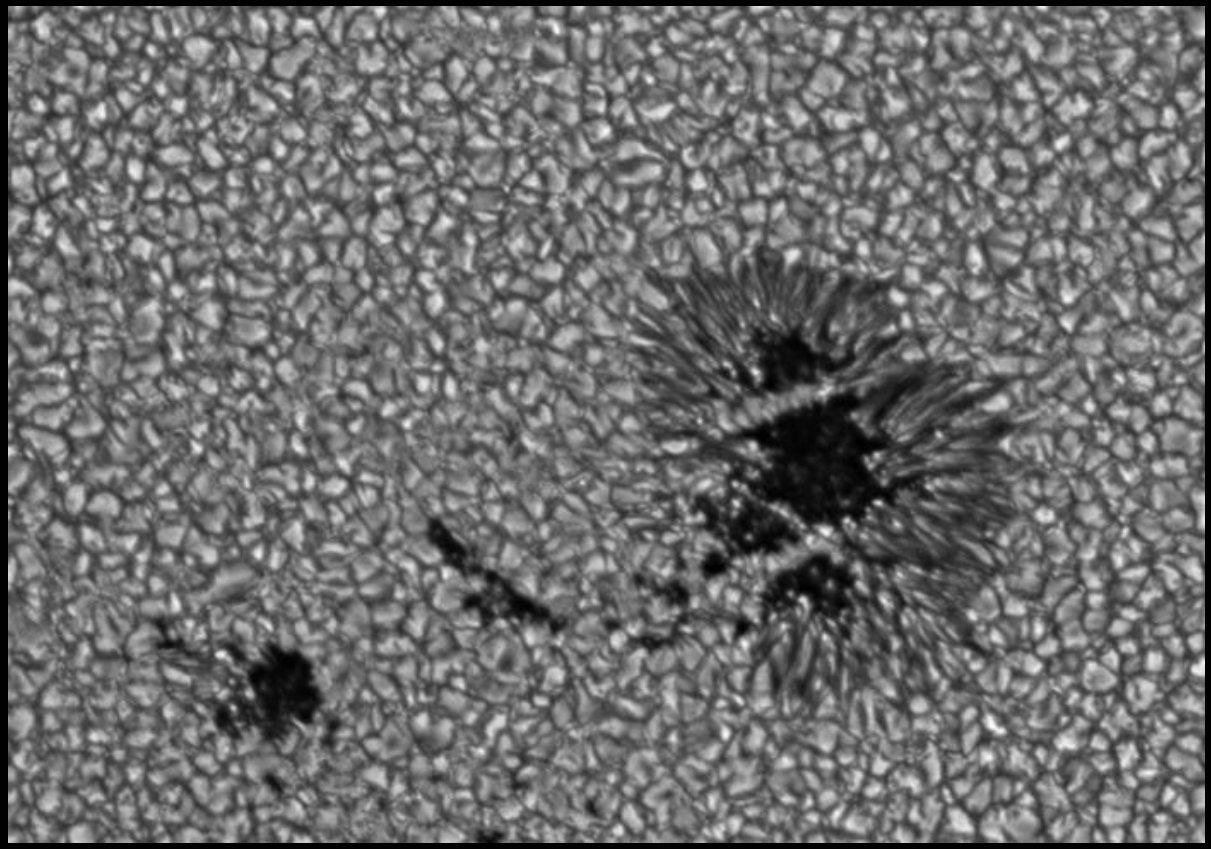

Sunspots

Sunspots appear as dark spots on the surface of the Sun. Temperatures in the dark centers of sunspots drop to about **3700 K** (compared to **5700 K** for the surrounding photo-sphere). They typically last for several days, although very large ones may live for several weeks.

Sunspots are magnetic regions on the Sun with magnetic field strengths thousands of times stronger than the Earth's magnetic field. Sunspots usually come in groups with two sets of spots. One set will have positive or north magnetic field while the other set will have negative or south magnetic field. The field is strongest in the darker parts of the sunspots - the umbra. The field is weaker and more horizontal in the lighter part – the penumbra.

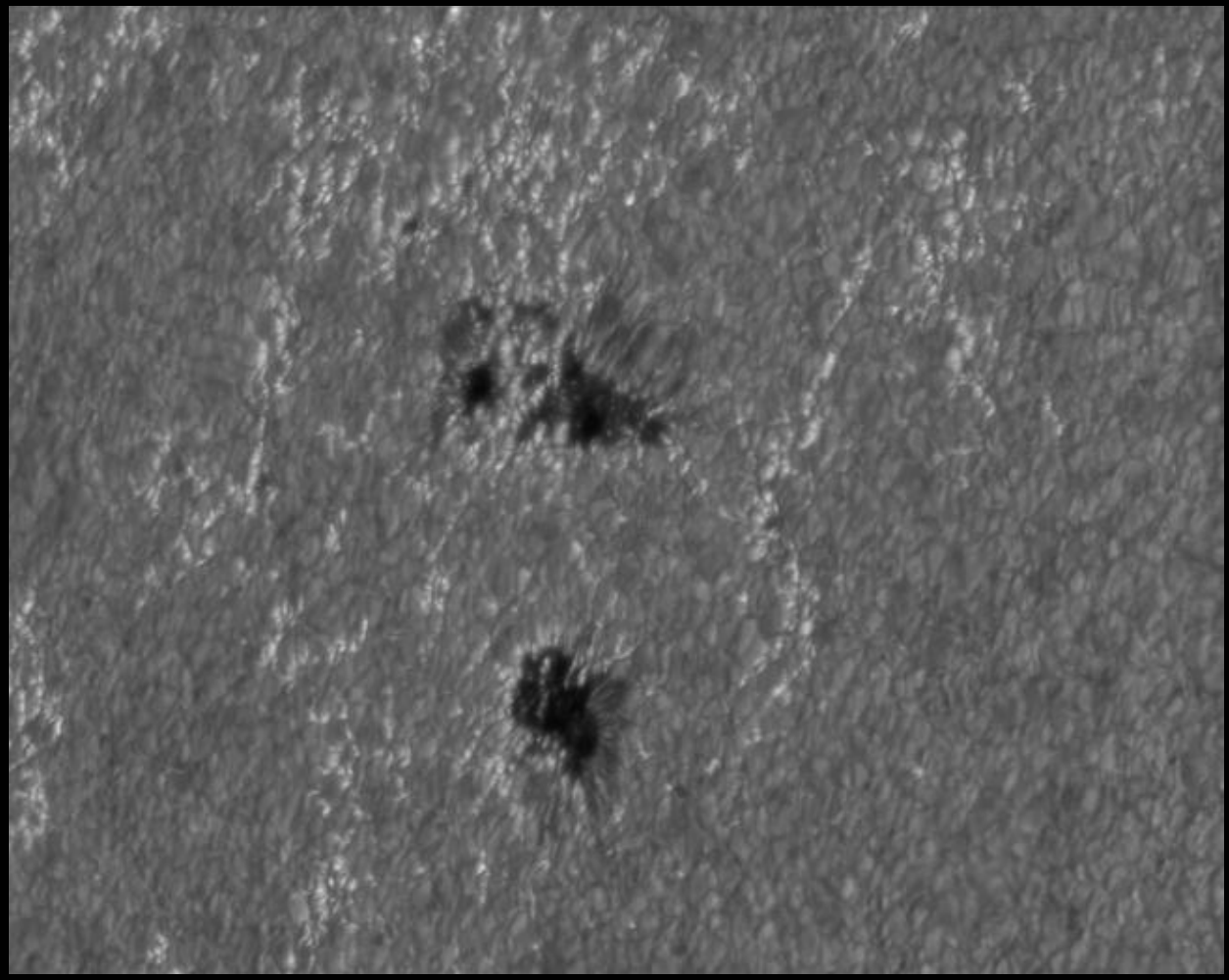

Faculae:

Faculae are bright areas that are usually most easily seen near the limb, or edge, of the solar disk. These are also magnetic areas but the magnetic field is concentrated in much smaller bundles than in sunspots.

While the sunspots tend to make the Sun look darker, the faculae make it look brighter. During a sunspot cycle the faculae actually win out over the sunspots and make the Sun appear slightly (about 0.1%) brighter at sunspot maximum that at sunspot minimum.

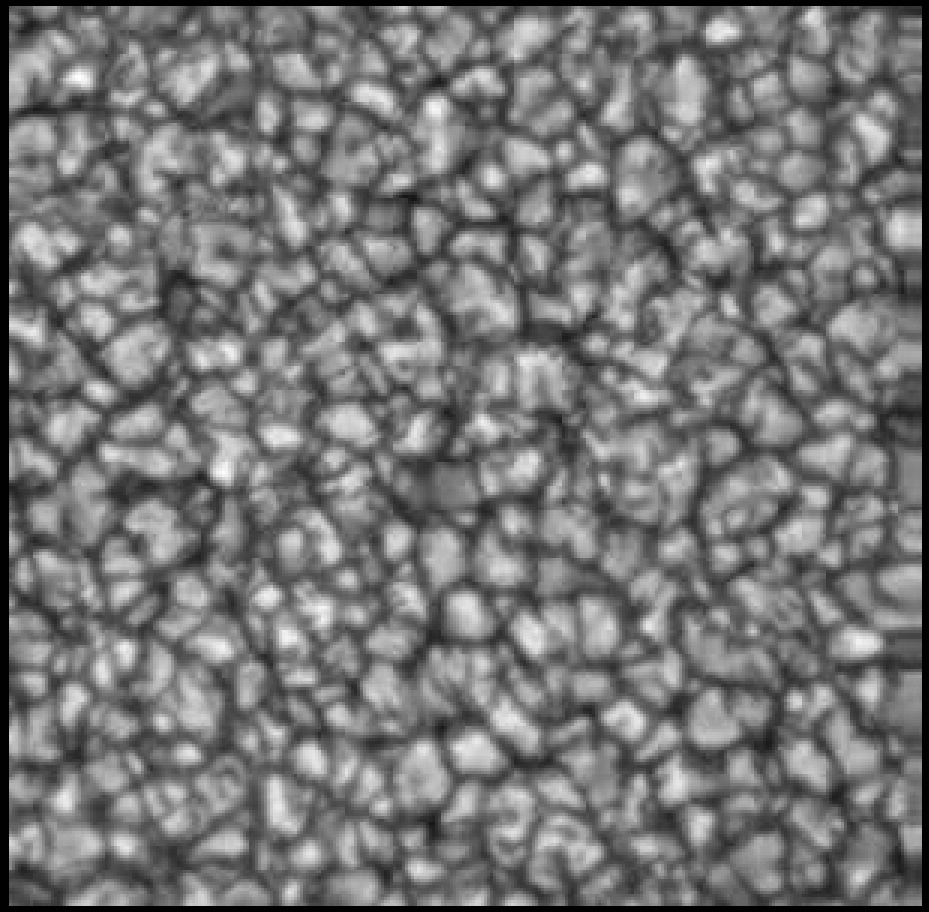

Granules:

Granules are small (about **1000 km** across) cellular features that cover the entire Sun except for those areas covered by sunspots. These features are the tops of convection cells where hot fluid rises up from the interior in the bright areas, spreads out across the surface, cools and then sinks inward along the dark lanes. Individual granules last for only about 20 minutes.

The granulation pattern is continually evolving as old granules are pushed aside by newly emerging ones. The flow within the granules can reach supersonic speeds of more than 7 km/s and produce sonic "booms" and other noise that generates waves on the Sun's surface. [The movie from Swedish Vacuum Solar Telescope.]

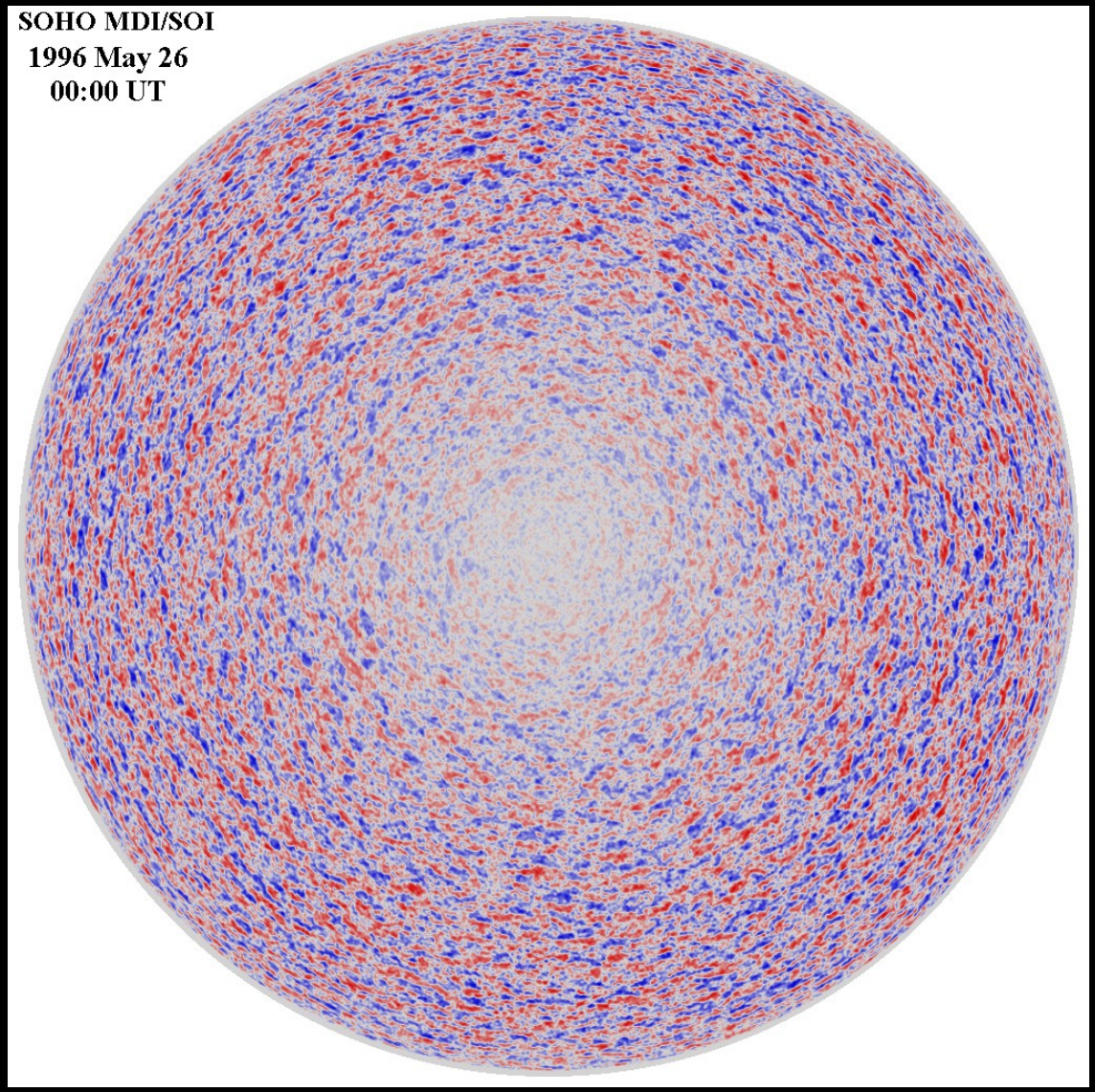

Supergranules:

Supergranules are much larger versions of granules (~ **35,000 km** across) but are best seen in measurements of the Doppler shift where light from material moving toward us is shifted to the blue while light from material moving away from us is shifted to the red. These features also cover the entire Sun and are continually evolving.

Individual supergranules last for a day or two and have flow speeds of about **0.5 km/s**

The fluid flows observed in supergranules carry magnetic field bundles to the edges of the cells where they produce the chromospheric network.

Animated Sun

[Borrowed from **Stanford Solar Center** URL http://solar-center.stanford.edu/].

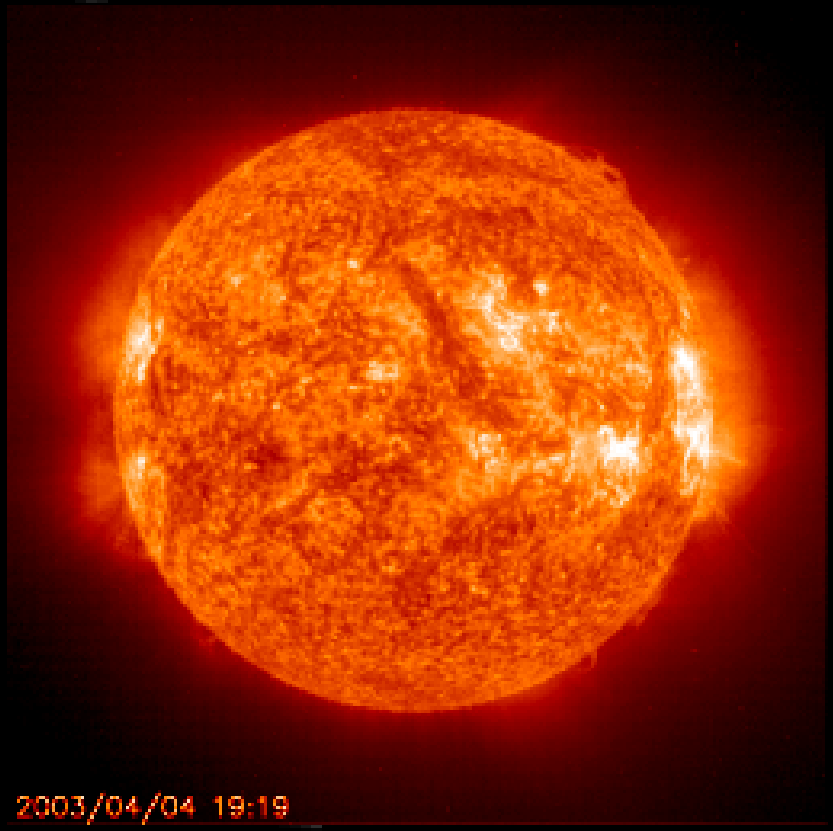

April-May 2003

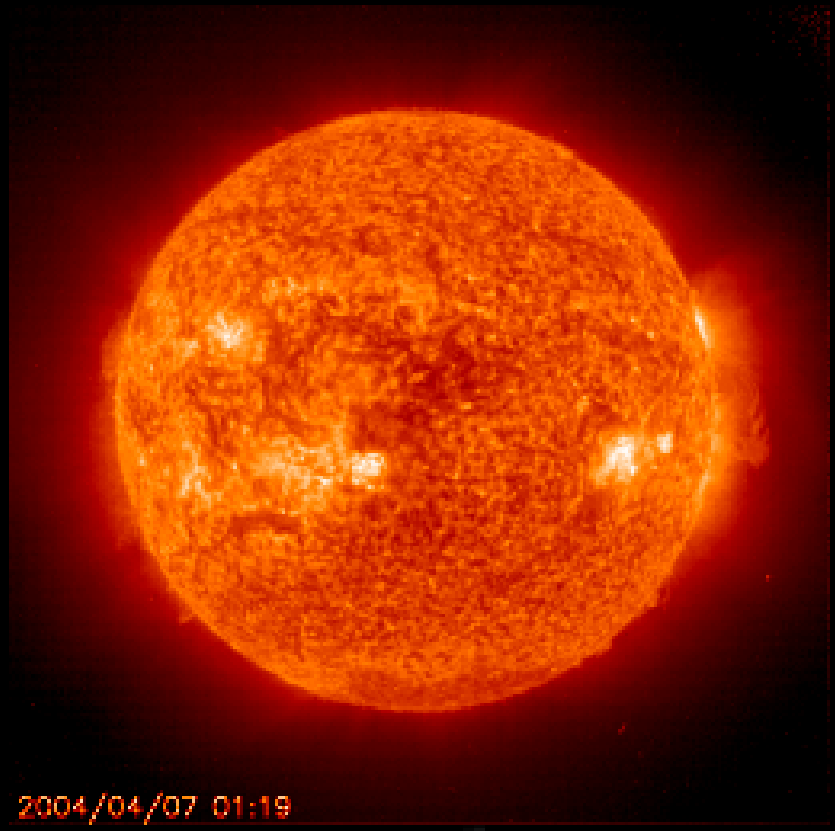

April-May 2004 (last 30 days)

The Sunspot Cycle

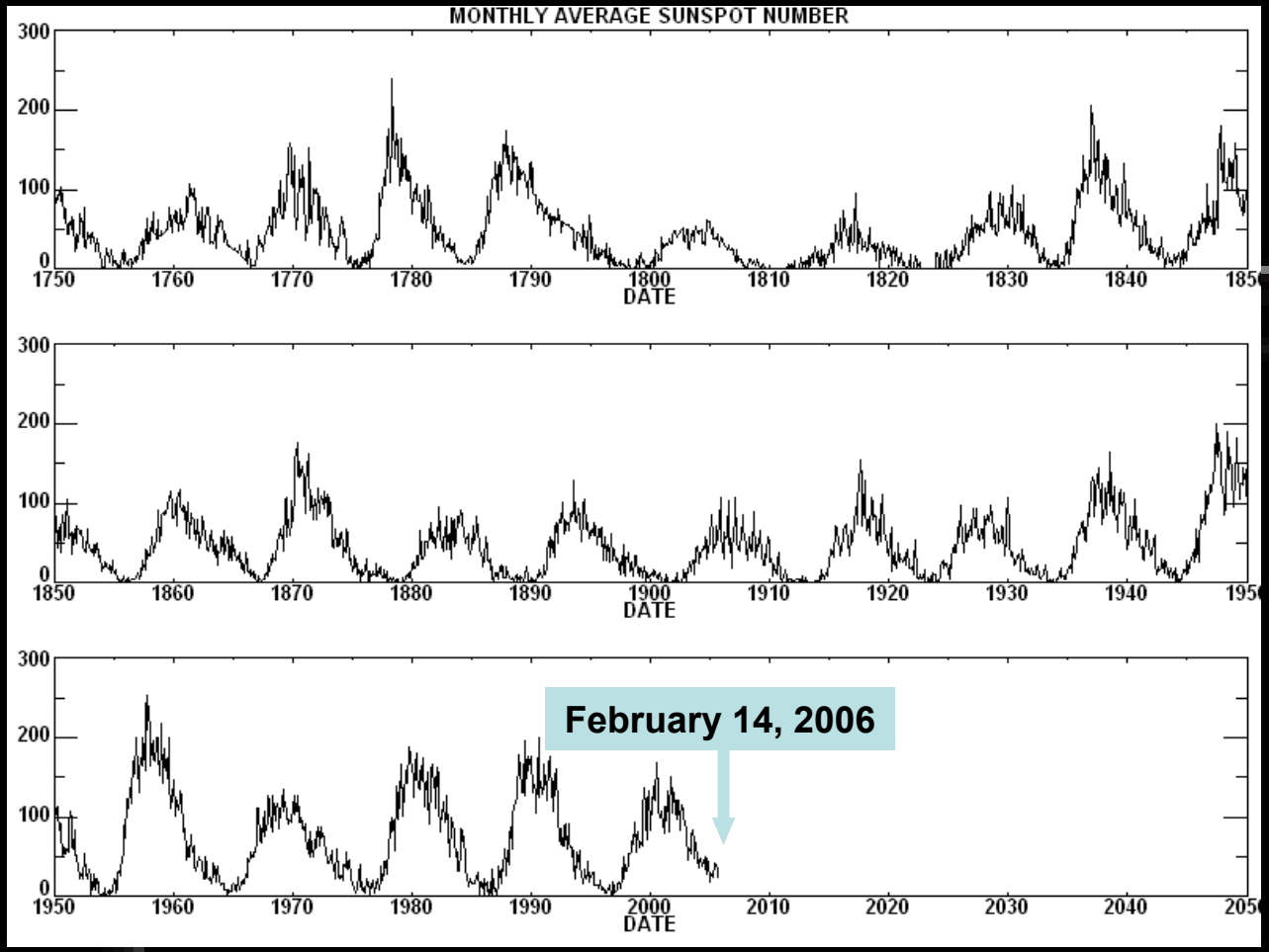

Monthly averages of the sunspot numbers show that the number of sunspots visible on the sun waxes and wanes with an approximate 11-year cycle. The figure is updated **monthly** by The Solar Physics Group at NASA's Marshall Space Flight Center [URL: http://science.nasa.gov/ssl/PAD/SOLAR/].

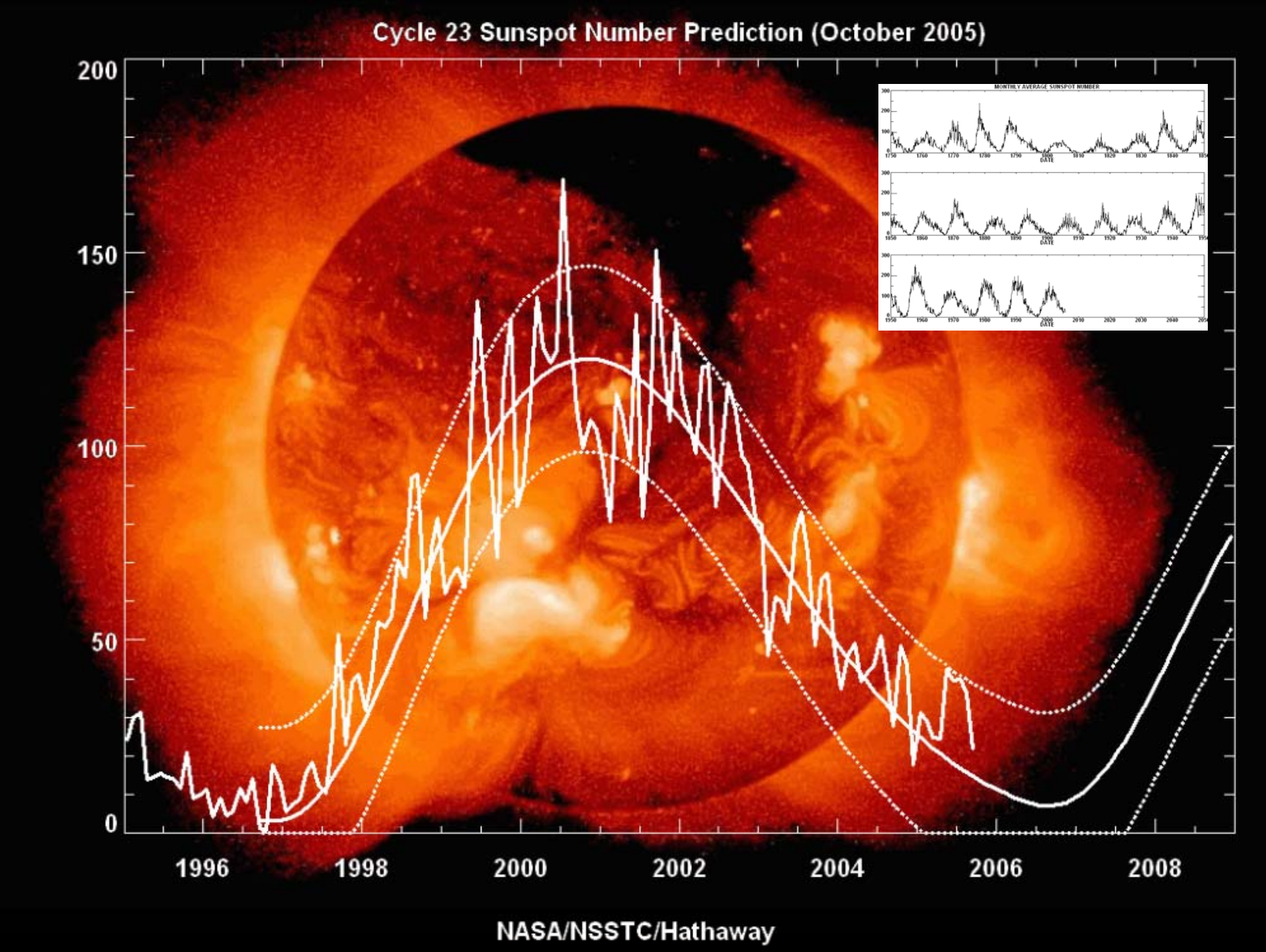
Cycle 23 Sunspot Number Prediction (October 2005)
200
150
100
50
0
1996
1998
2000
2002
2004
2006
2008
MONTHLY AVERAGE SUNSPOT NUMBER
DATE
NASA/NSSTC/Hathaway

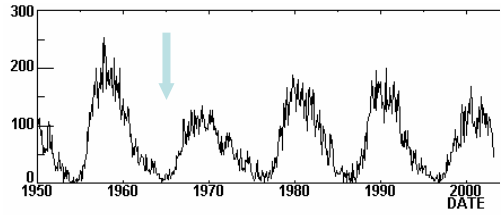

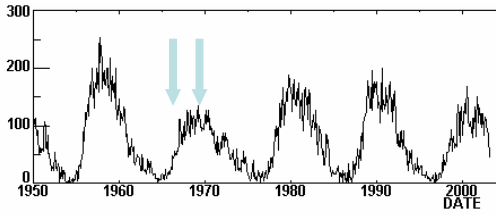

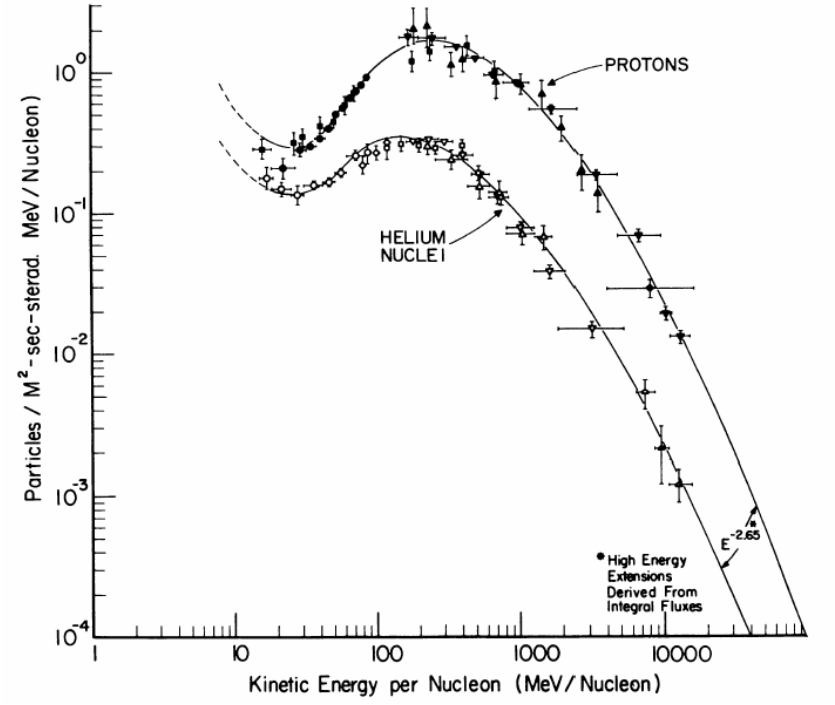

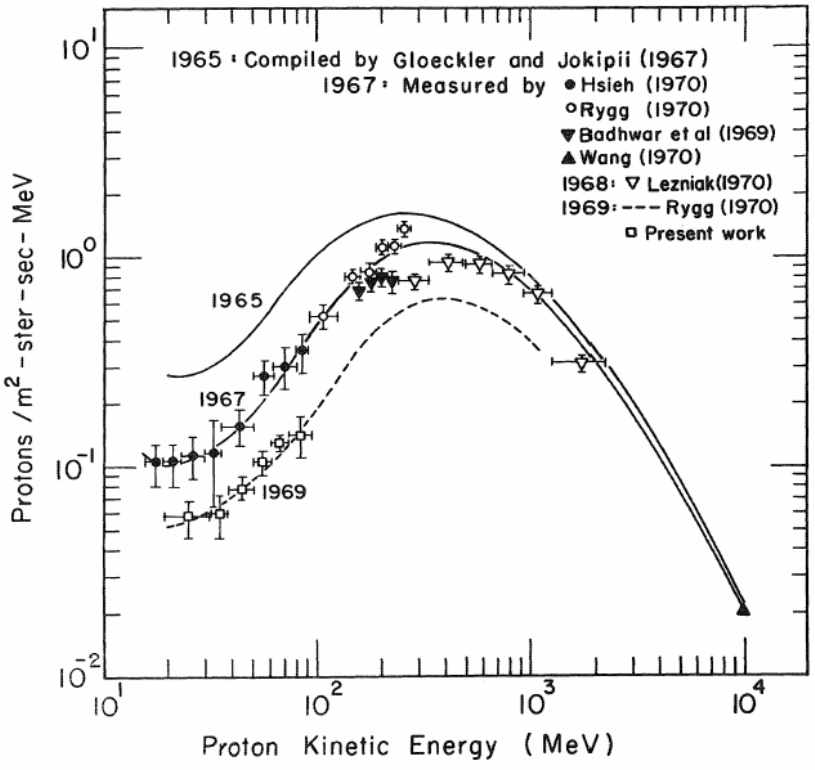

Primary differential kinetic-energy/nucleon spectra of CR protons and helium nuclei obtained near Earth near the solar minimum in 1965.

[**Reference**: G. Gloeckler & J.P. Jokipi, ApJ **148** (1967) L41.]

Primary differential kinetic-energy spectra of protons in 1965, 1967, and 1969. The 1965 spectrum is taken from the compilation of Gloeckler and Jokipi.

[**Reference**: K.C. Hsieh et al., ApJ **166** (1971) 221.]

Low and intermediate energy part of the CR spectrum for the main nuclear groups

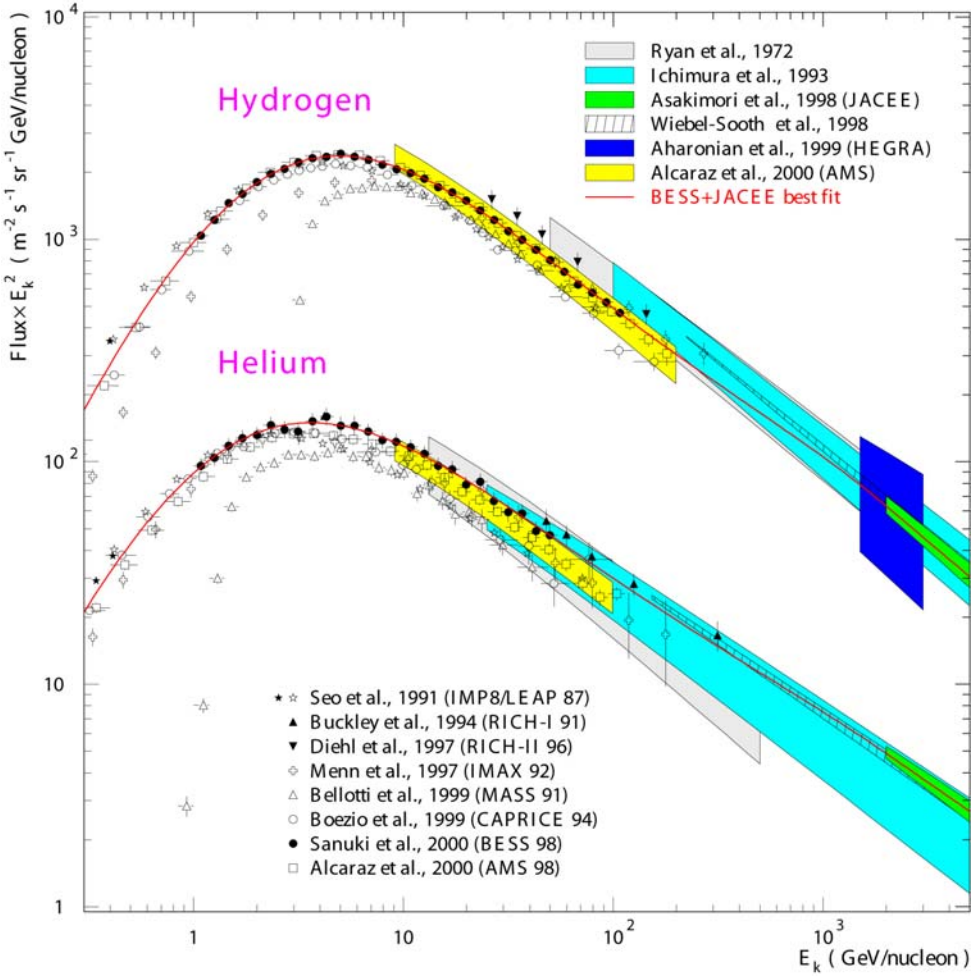

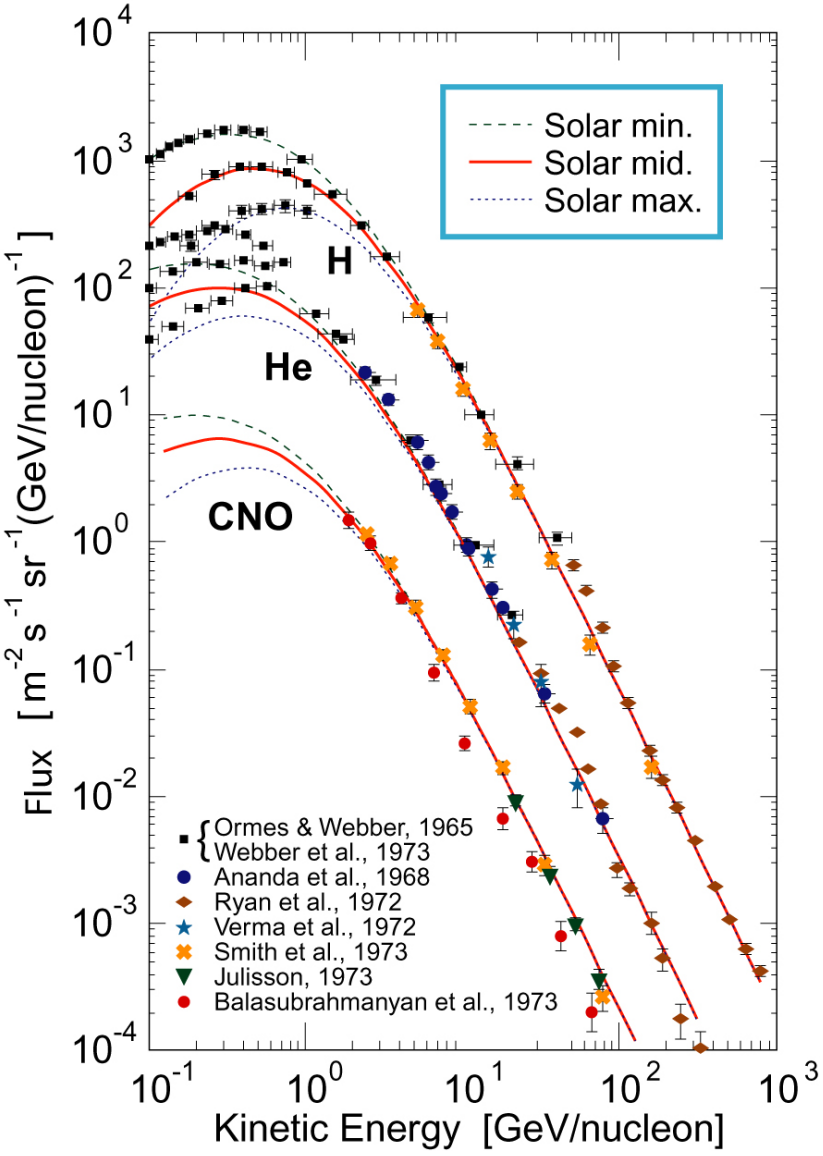

CR Neutron Monitoring
(in short)

The cosmic ray lab of University of Delaware at McMurdo Station, Ross Island, Antarctica. →

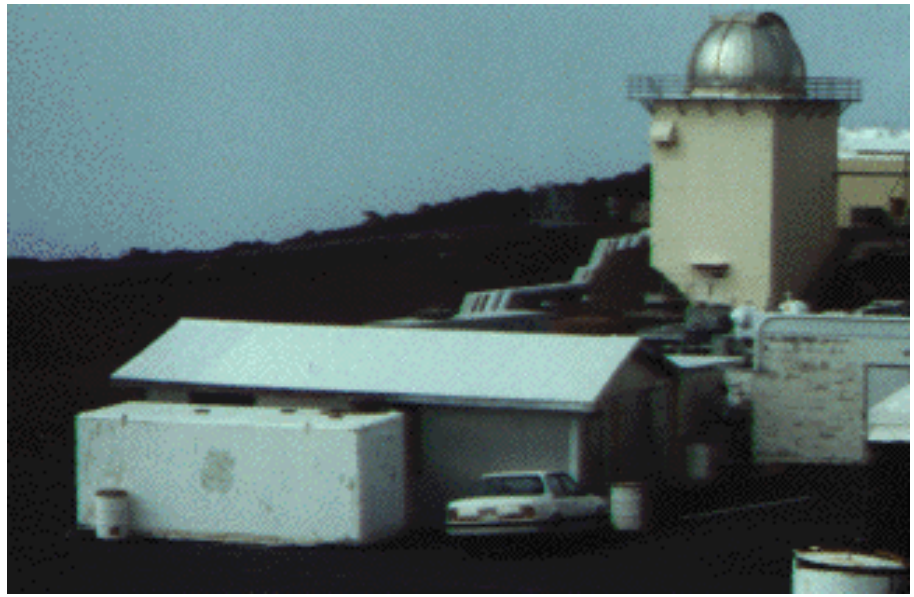

University of New Hampshire cosmic ray labs at Huancayo, Peru (**left**) and Haleakala, Hawaii (**right**).

Cosmic Ray Neutron Monitors, 1997

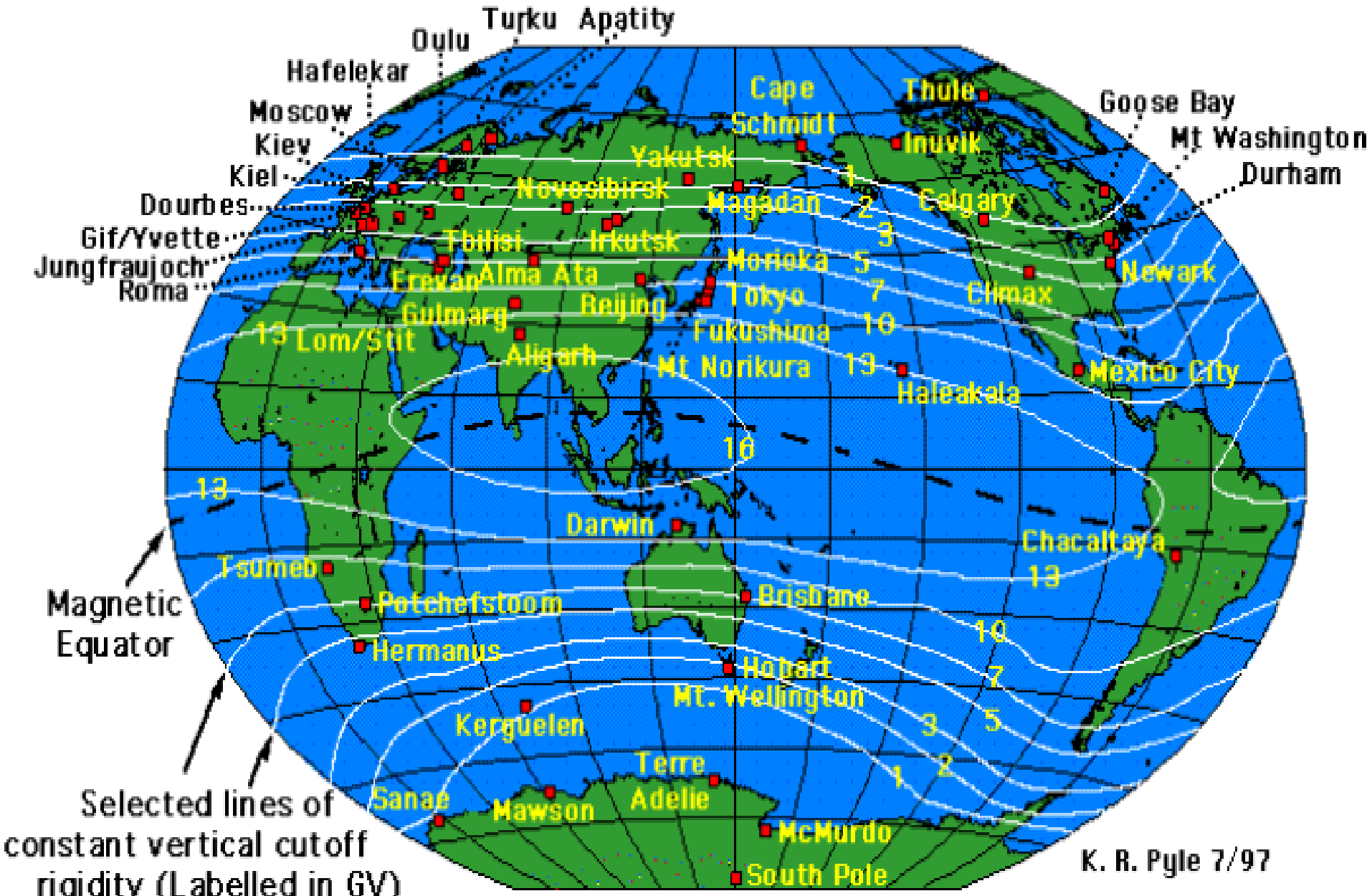

From University of New Hampshire, URL: http://ulysses.sr.unh.edu/NeutronMonitor/neutron_mon.html

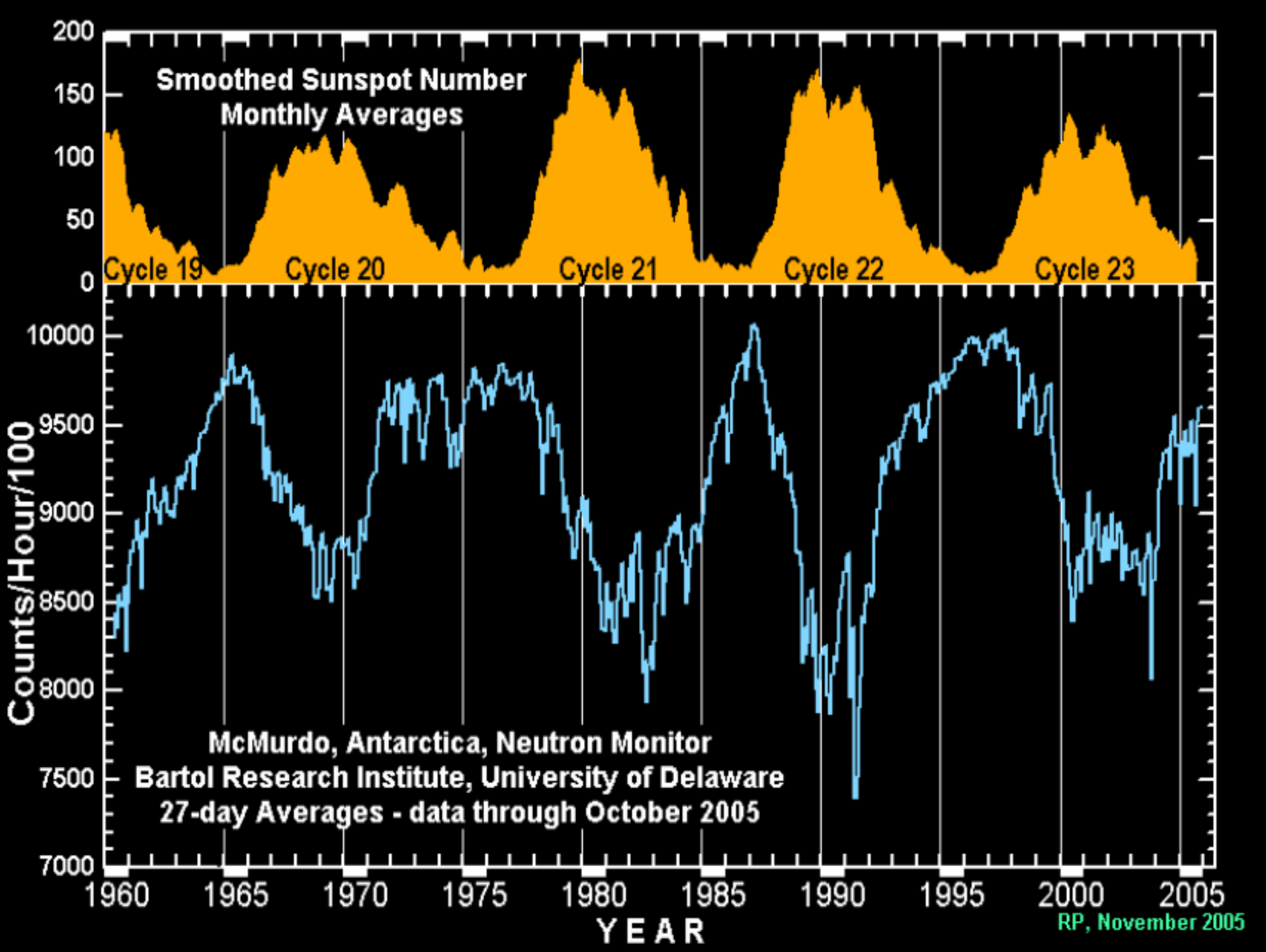
Smoothed Sunspot Number
Monthly Averages
200
150
100
50
0
Cycle 19
Cycle 20
Cycle 21
Cycle 22
Cycle 23
Counts/Hour/100
10000
9500
9000
8500
8000
7500
7000
McMurdo, Antarctica, Neutron Monitor
Bartol Research Institute, University of Delaware
27-day Averages - data through October 2005
1960
1965
1970
1975
1980
1985
1990
1995
2000
2005
YEAR
RP, November 2005

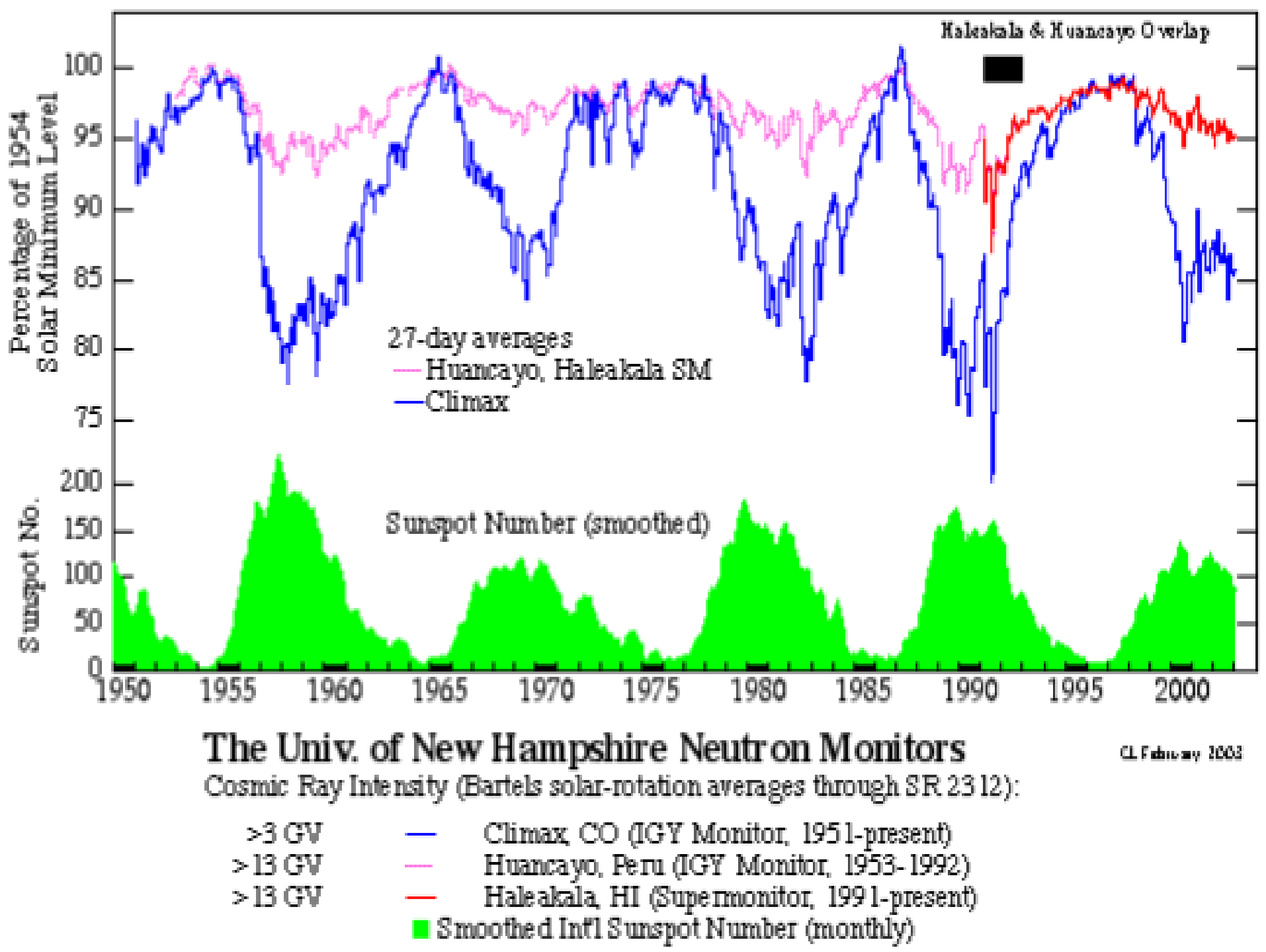

The Univ. of New Hampshire Neutron Monitors

Cosmic Ray Intensity (Bartels solar-rotation averages through SR 2312):

>3 GV	—	Climax, CO (IGY Monitor, 1951-present)
>13 GV	—	Huancayo, Peru (IGY Monitor, 1953-1992)
>13 GV	—	Haleakala, HI (Supermonitor, 1991-present)
	■	Smoothed Intl Sunspot Number (monthly)

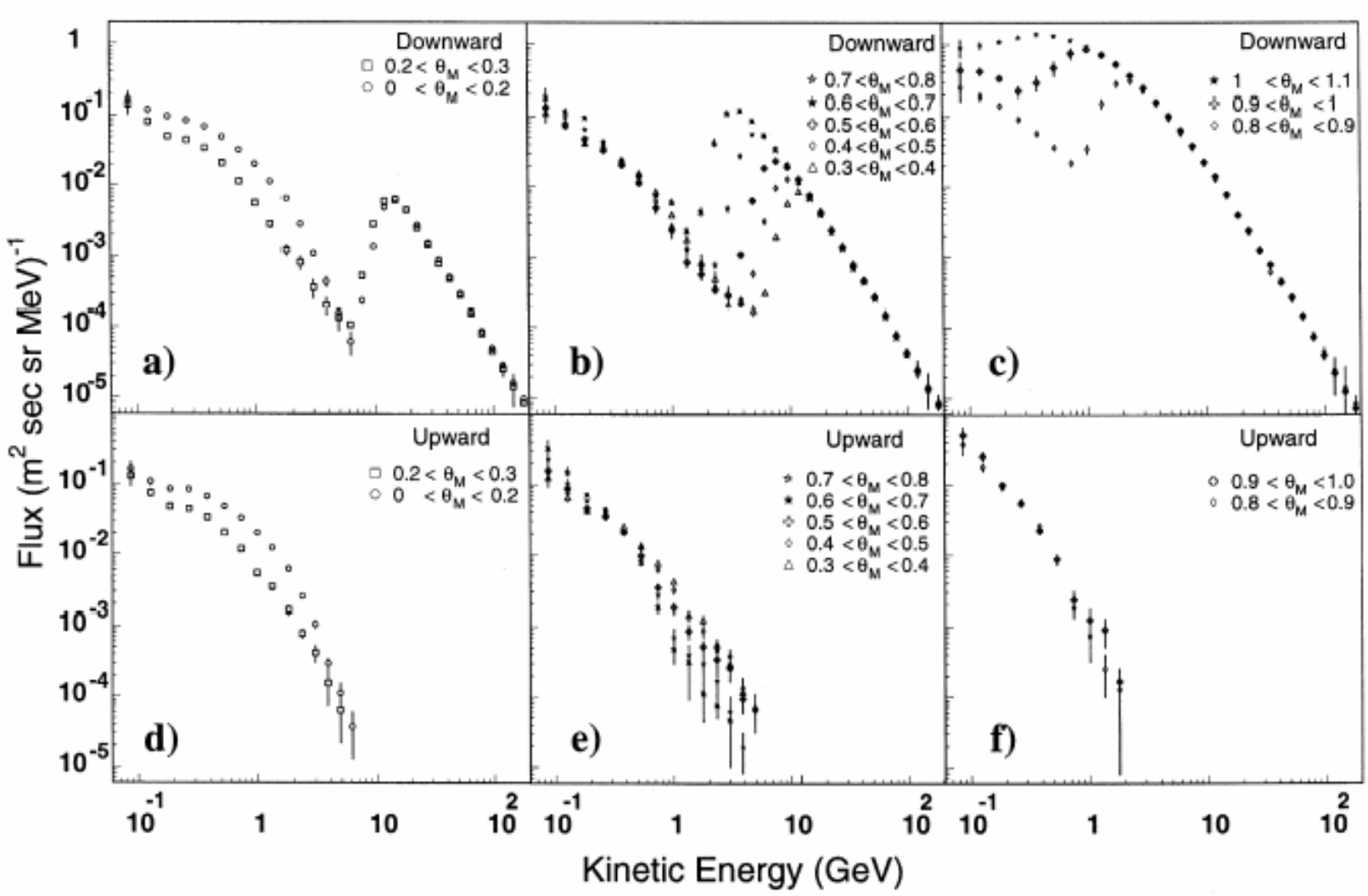

Flux spectra for downward going (**a,b,c**) and upward going (***d,e,f***) protons separated according to the geomagnetic latitude, Q_M, at which they were detected with AMS during the space shuttle flight STS-91 at an altitude of 380 km.

[**Reference**: J. Alcaraz et al. (AMS Collaboration), Phys. Lett. B **472** (2000) 215-226 (hep-ex/0002049).]

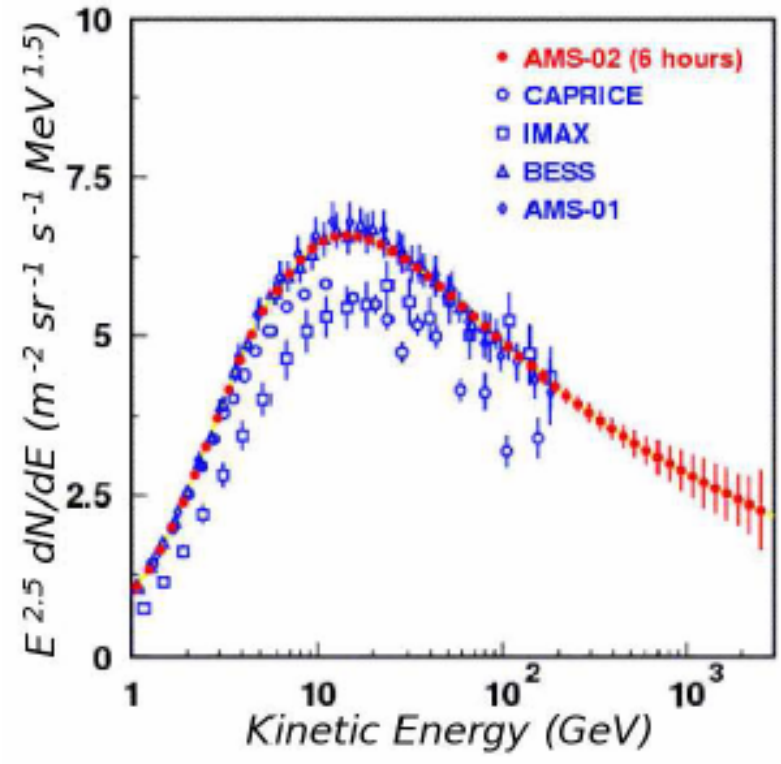

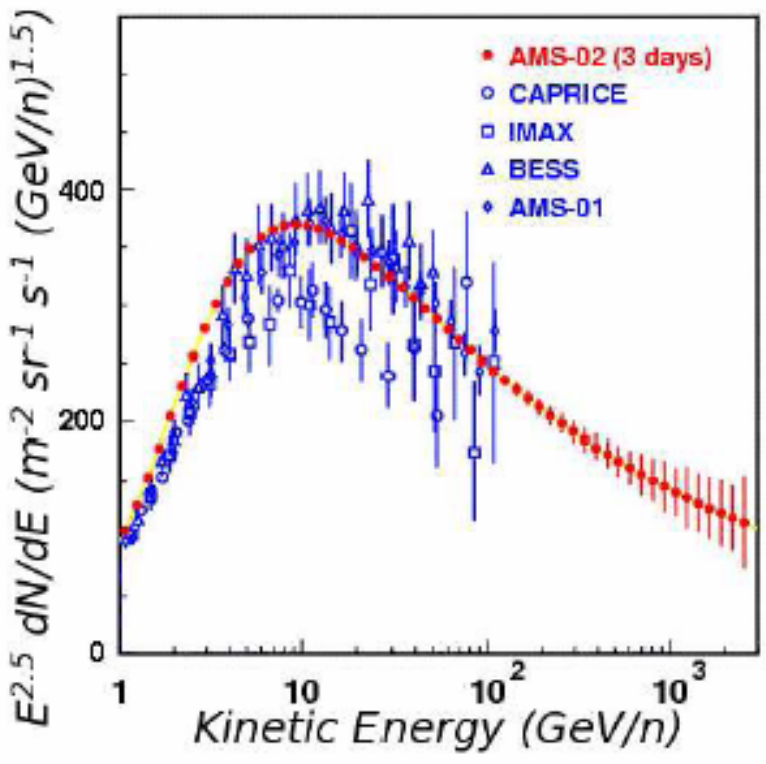

CR proton (**left panel**) and helium (**right panel**) flux measurements are compared to the expected AMS-02. A two-phases cylindrical model of the Galaxy has been used to simulate the propagation of Protons and helium nuclei in the interstellar medium where they diffuse for roughly **2×10^7** years. These nuclei are the dipest charged probes of the Galaxy since they diffuse on the average through **one third** of the Galactic disk and in the halo before being measured.

[Reference: D. Casadei (for the AMS Collaboration), “Cosmic ray astrophysics with AMS-02,“ astro-ph/0404529.**]**

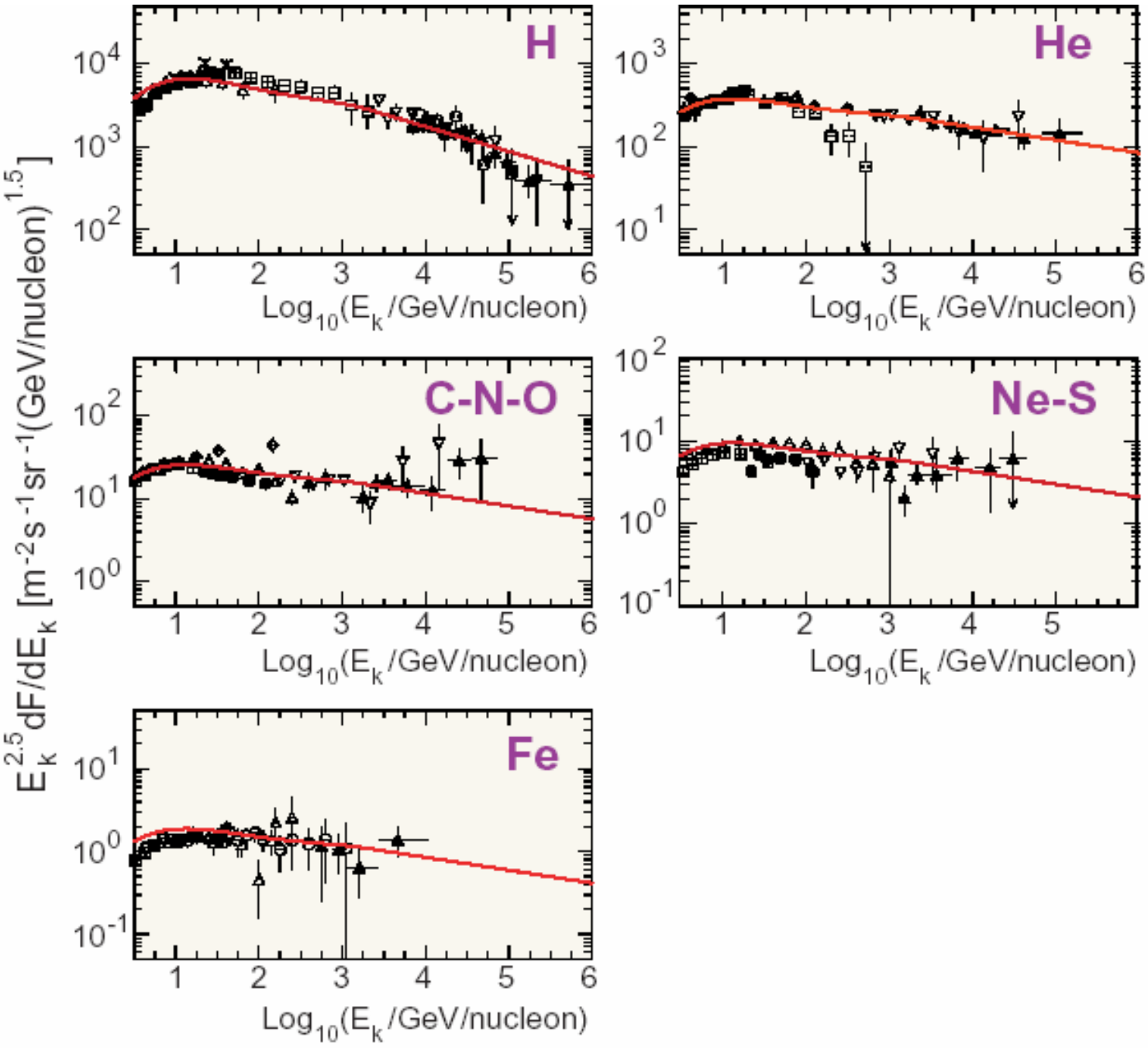
H
He
C-N-O
Ne-S
Fe
$E_k^{2.5} dF/dE_k$ [$m^{-2} s^{-1} sr^{-1} (GeV/nucleon)^{1.5}$]
$Log_{10}(E_k/GeV/nucleon)$

Isotopic Composition

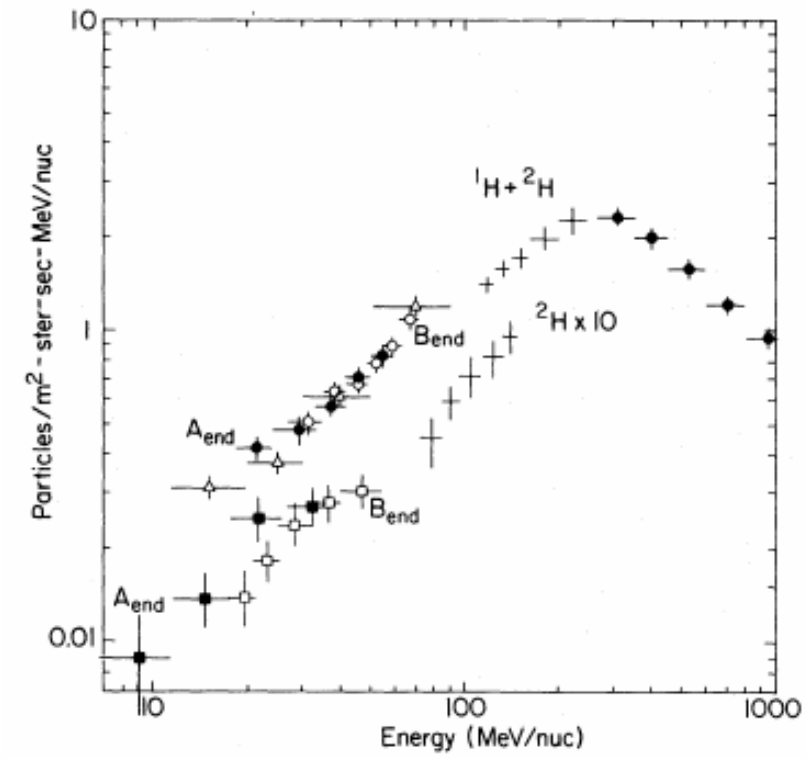

Kinetic-energy spectra of ^{1}H and ^{2}H obtained from balloon and spacecraft (Voyager) experiments at sunspot minimum modulation conditions in 1977.

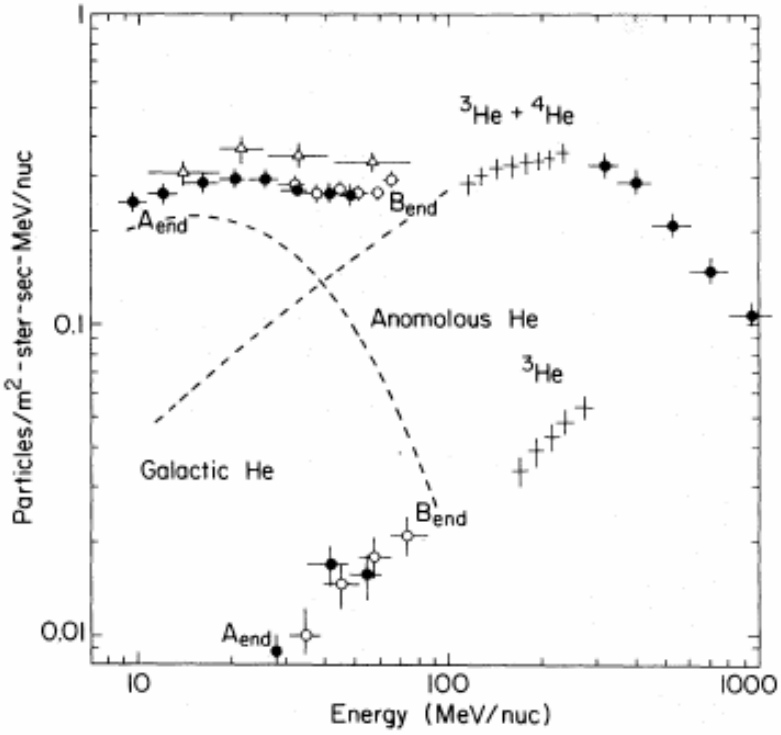

Kinetic-energy spectra of ^{3}He and ^{4}He obtained from the same experiments. Estimated magnitude of anomalous He component and galactic He are shown by dashed lines at low energies.

In both panels, the data points designated by triangles are from Bastian et al. (1979) for a similar time period.

[**Reference**: W.R. Webber and S.M. Yushak, ApJ **275** (1983) 391.]

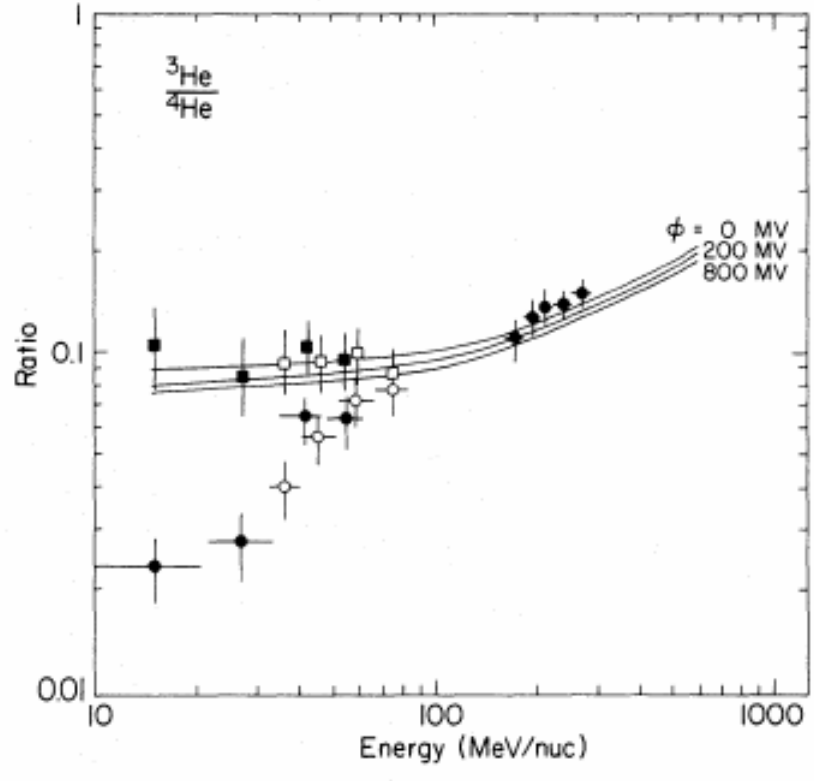

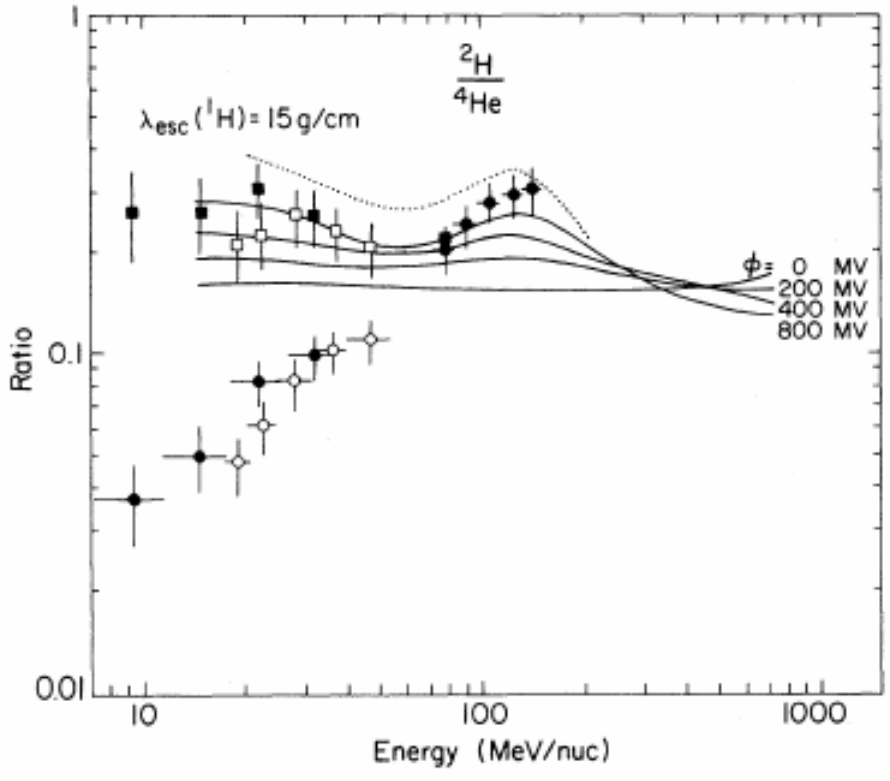

The $^3He/^4He$ ratios measured as a function of kinetic energy in the balloon and spacecraft experiments. Predictions of an interstellar propagation model for various values of the modulation parameter are shown as solid lines. Corrections to the $^3He/^4He$ ratios for the presence of anomalous ^4He are shown by open and solid squares.

Measured $^2H/^4He$ ratios at low energies and predictions based on the same interstellar propagation model and local modulation as for He. Ratios corrected for anomalous ^4He are shown by open and solid squares at low energies.

[**Reference**: W.R. Webber and S.M. Yushak, ApJ **275** (1983) 391.]

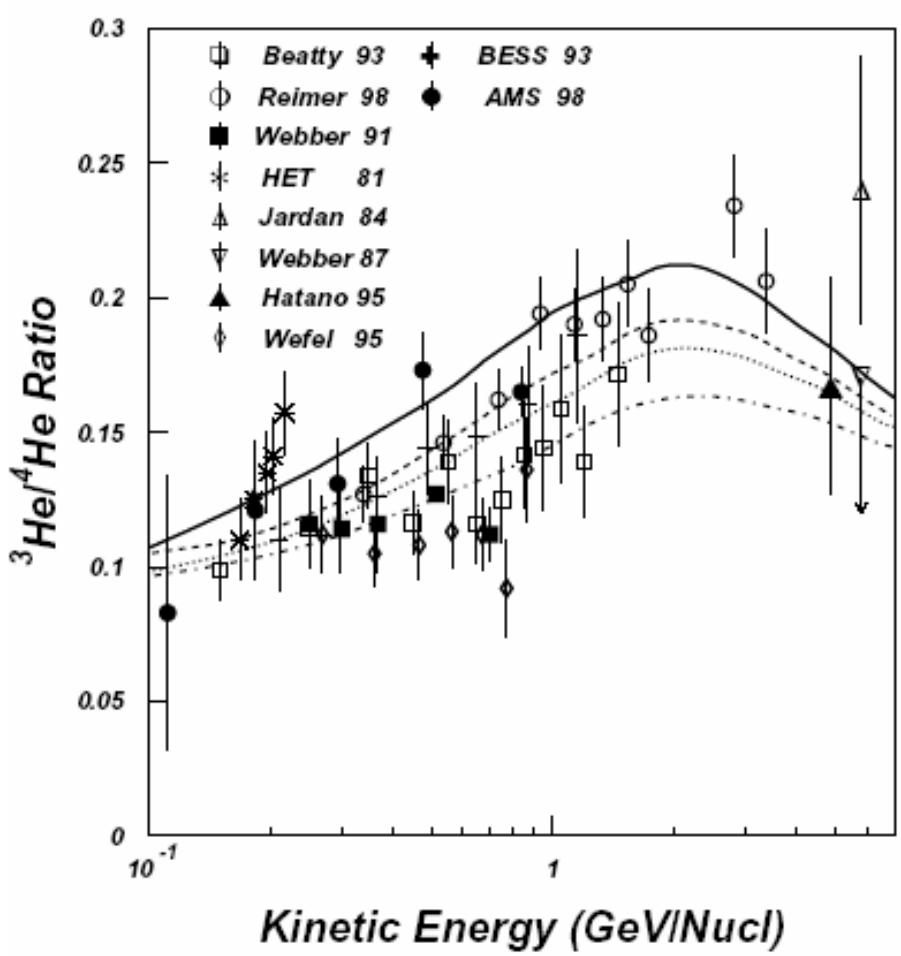

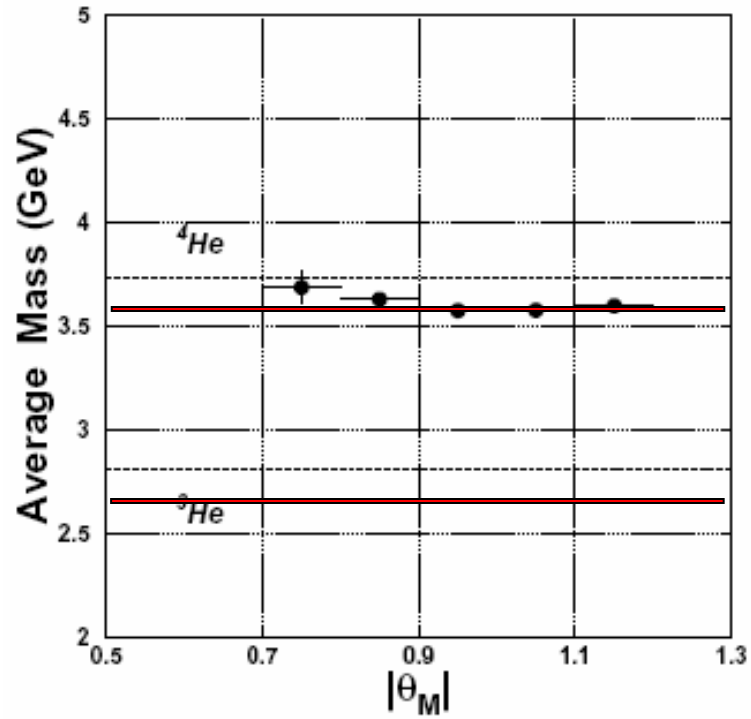

The $^3He/^4He$ ratios with measured in different experiments. The model predictions for various solar modulation levels are also shown with solid (φ = 0.35 GV), dashed (φ = 0.5 GV), dot line (φ = 1.0 GV), and dot-dashed (φ = 1.5 GV) lines.

[**Reference**: Z. Xiong et al., JHEP **11** (2003) 048.]

The dependence of average helium mass on the geomagnetic latitude measured with AMS.

[**Reference**: Z. Xiong et al., JHEP **11** (2003) 048.]

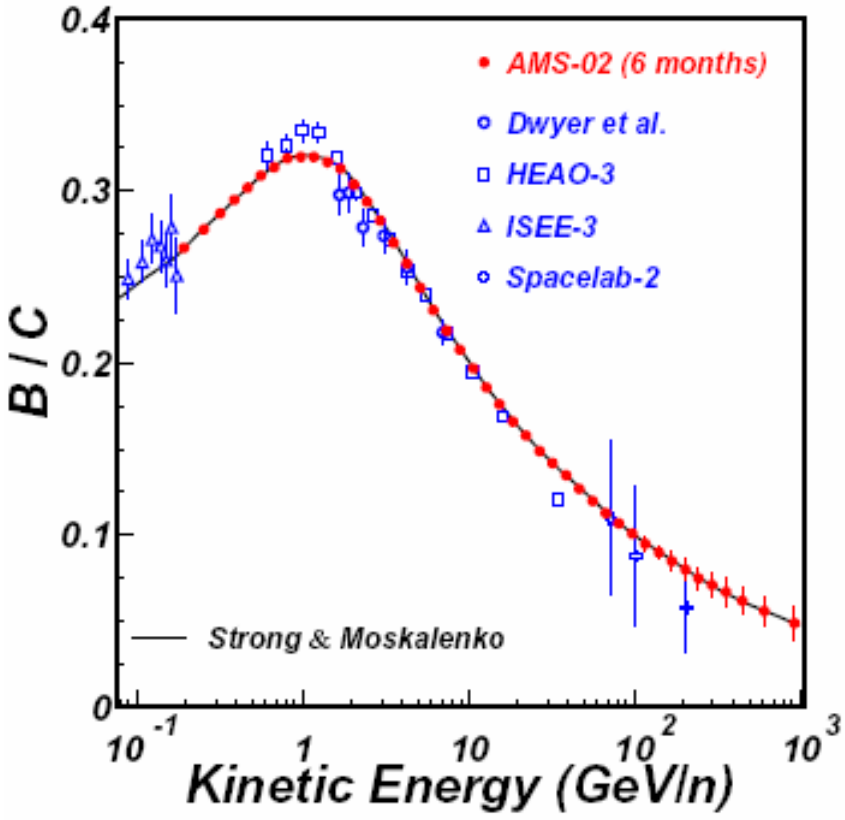

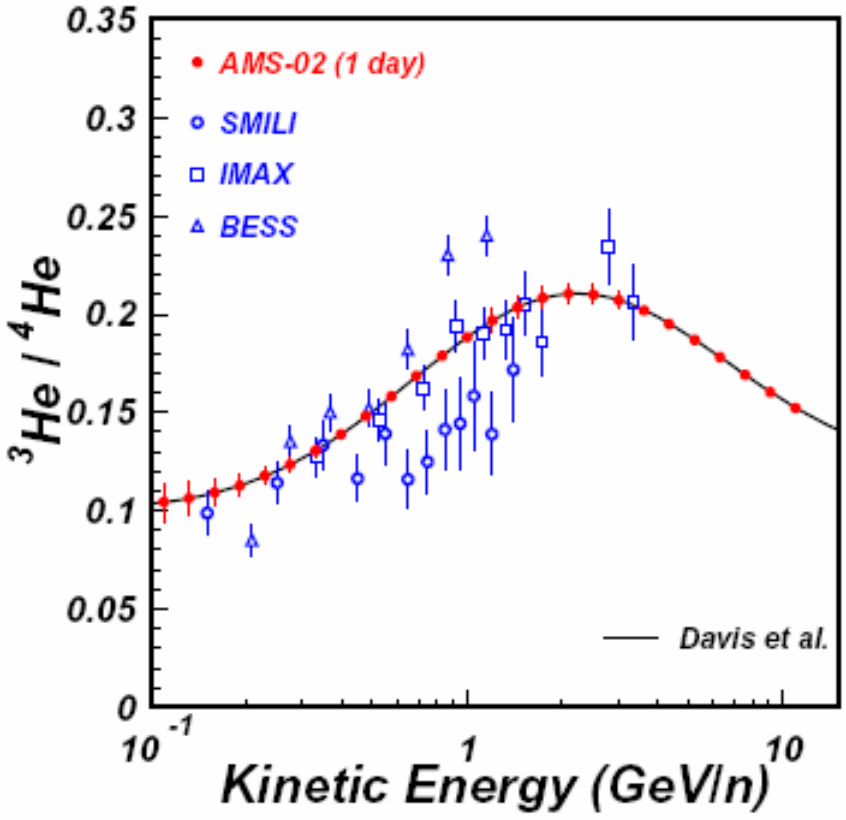

AMS-02 expected performance on **B/C** ratio (**left panel**) after six months of data taking and **^{3}He/^{4}He** ratio (**right panel**) after one-day of data taking compared to recent measurements. The **B/C** ratio was simulated according to a ***diffuse-reacceleration model*** (Strong & Moskalenko, 2001) with Alfvèn speed **v_A = 20 km/s**, propagation region bounded by a galactocentric radius **R_h = 30 kpc**, distance from the galactic plane **z_h = 1 kpc**. The **^{3}He/^{4}He** ratio has been simulated according to the classical cosmic-ray transport ***Leaky Box Model*** with a rigidity dependent path-length distribution (Davis et al, 1995).

[**Reference**: G. Lamanna, Mod. Phys. Lett. A **18** (2003) 1951-1966.]

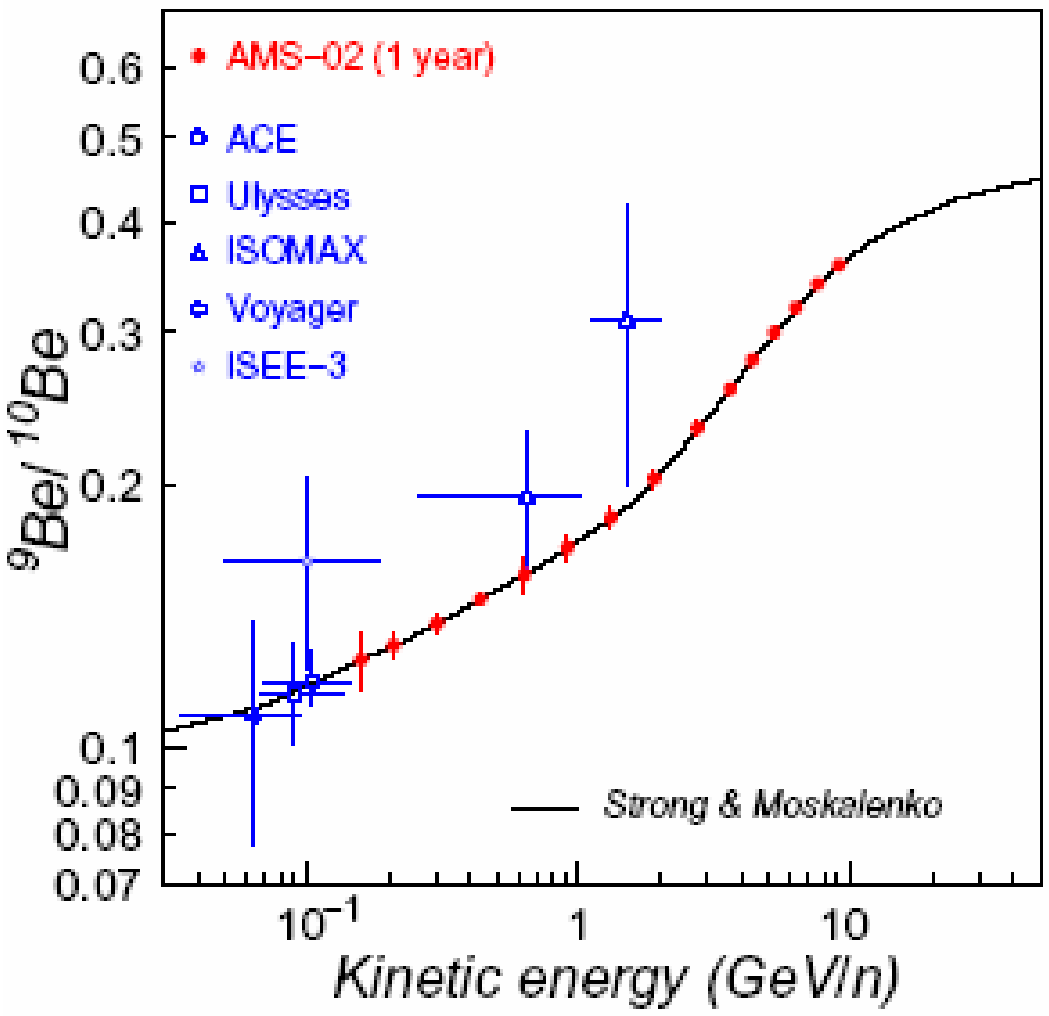

Beryllium measurements.
The expected AMS-02 1 year statistics is also shown assuming a model by Strong and Moskalenko.

[**Reference**: D. Casadei (for the AMS Collaboration), “Cosmic ray astrophysics with AMS-02,” astro-ph/0404529.]

Around the knee
("poly-gonato"[a] model by Jorg Hörandel[b])

The Poly-Gonato Model (PGM) is an empirical model to systematize and fit the data on primary spectra of all CR nuclei at high energies. It is assumed that the cutoff energy for each individual element depends on its charge Z. The following ansatz is adopted to describe the energy dependence of the flux for particles with charge Z.

$$F_Z(E) = \Phi_Z^0 E^{\gamma_Z} \left[1 + \left(\frac{E}{E_Z}\right)^{\epsilon_c}\right]^{\frac{\gamma_c - \gamma_Z}{\epsilon_c}}$$

The absolute flux normalization, Φ_Z^0 and the spectral index γ_Z quantify the power law. The flux above the cutoff energy is modeled by a second and steeper power law. Parameters γ_c and ϵ_c characterize the change in the spectrum at the cutoff energy E_Z. Both parameters are assumed to be identical for all spectra, γ_c being the hypothetical slope beyond the knee and ϵ_c describes the smoothness of the transition from the first to the second power law.

---

[a] Greek "many knees".

[b] **Reference**: J. R. Hörandel, Astropart. Phys. 19 (2003) 193.

Z		Φ_Z^0	$-\gamma_Z$	Z		Φ_Z^0	$-\gamma_Z$	Z		Φ_Z^0	$-\gamma_Z$
1^2	H	$8.73 \cdot 10^{-2}$	2.71	32^4	Ge	$4.02 \cdot 10^{-6}$	2.54	63^4	Eu	$1.58 \cdot 10^{-7}$	2.27
2^2	He	$5.71 \cdot 10^{-2}$	2.64	33^4	As	$9.99 \cdot 10^{-7}$	2.54	64^4	Gd	$6.99 \cdot 10^{-7}$	2.25
3^3	Li	$2.08 \cdot 10^{-3}$	2.54	34^4	Se	$2.11 \cdot 10^{-6}$	2.53	65^4	Tb	$1.48 \cdot 10^{-7}$	2.24
4^3	Be	$4.74 \cdot 10^{-4}$	2.75	35^4	Br	$1.34 \cdot 10^{-6}$	2.52	66^4	Dy	$6.27 \cdot 10^{-7}$	2.23
5^3	B	$8.95 \cdot 10^{-4}$	2.95	36^4	Kr	$1.30 \cdot 10^{-6}$	2.51	67^4	Ho	$8.36 \cdot 10^{-8}$	2.22
6^3	C	$1.06 \cdot 10^{-2}$	2.66	37^4	Rb	$6.93 \cdot 10^{-7}$	2.51	68^4	Er	$3.52 \cdot 10^{-7}$	2.21
7^3	N	$2.35 \cdot 10^{-3}$	2.72	38^4	Sr	$2.11 \cdot 10^{-6}$	2.50	69^4	Tm	$1.02 \cdot 10^{-7}$	2.20
8^3	O	$1.57 \cdot 10^{-2}$	2.68	39^4	Y	$7.82 \cdot 10^{-7}$	2.49	70^4	Yb	$4.15 \cdot 10^{-7}$	2.19
9^3	F	$3.28 \cdot 10^{-4}$	2.69	40^4	Zr	$8.42 \cdot 10^{-7}$	2.48	71^4	Lu	$1.72 \cdot 10^{-7}$	2.18
10^3	Ne	$4.60 \cdot 10^{-3}$	2.64	41^4	Nb	$5.05 \cdot 10^{-7}$	2.47	72^4	Hf	$3.57 \cdot 10^{-7}$	2.17
11^3	Na	$7.54 \cdot 10^{-4}$	2.66	42^4	Mo	$7.79 \cdot 10^{-7}$	2.46	73^4	Ta	$2.16 \cdot 10^{-7}$	2.16
12^3	Mg	$8.01 \cdot 10^{-3}$	2.64	43^4	Tc	$6.98 \cdot 10^{-8}$	2.46	74^4	W	$4.16 \cdot 10^{-7}$	2.15
13^3	Al	$1.15 \cdot 10^{-3}$	2.66	44^4	Ru	$3.01 \cdot 10^{-7}$	2.45	75^4	Re	$3.35 \cdot 10^{-7}$	2.13
14^3	Si	$7.96 \cdot 10^{-3}$	2.75	45^4	Rh	$3.77 \cdot 10^{-7}$	2.44	76^4	Os	$6.42 \cdot 10^{-7}$	2.12
15^3	P	$2.70 \cdot 10^{-4}$	2.69	46^4	Pd	$5.10 \cdot 10^{-7}$	2.43	77^4	Ir	$6.63 \cdot 10^{-7}$	2.11
16^3	S	$2.29 \cdot 10^{-3}$	2.55	47^4	Ag	$4.54 \cdot 10^{-7}$	2.42	78^4	Pt	$1.03 \cdot 10^{-6}$	2.10
17^3	Cl	$2.94 \cdot 10^{-4}$	2.68	48^4	Cd	$6.30 \cdot 10^{-7}$	2.41	79^4	Au	$7.70 \cdot 10^{-7}$	2.09
18^3	Ar	$8.36 \cdot 10^{-4}$	2.64	49^4	In	$1.61 \cdot 10^{-7}$	2.40	80^4	Hg	$7.43 \cdot 10^{-7}$	2.08
19^3	K	$5.36 \cdot 10^{-4}$	2.65	50^4	Sn	$7.15 \cdot 10^{-7}$	2.39	81^4	Ti	$4.28 \cdot 10^{-7}$	2.06
20^3	Ca	$1.47 \cdot 10^{-3}$	2.70	51^4	Sb	$2.03 \cdot 10^{-7}$	2.38	82^4	Pb	$8.06 \cdot 10^{-7}$	2.05
21^3	Sc	$3.04 \cdot 10^{-4}$	2.64	52^4	Te	$9.10 \cdot 10^{-7}$	2.37	83^4	Bi	$3.25 \cdot 10^{-7}$	2.04
22^3	Ti	$1.14 \cdot 10^{-3}$	2.61	53^4	I	$1.34 \cdot 10^{-7}$	2.37	84^4	Po	$3.99 \cdot 10^{-7}$	2.03
23^3	V	$6.31 \cdot 10^{-4}$	2.63	54^4	Xe	$5.74 \cdot 10^{-7}$	2.36	85^4	At	$4.08 \cdot 10^{-8}$	2.02
24^3	Cr	$1.36 \cdot 10^{-3}$	2.67	55^4	Cs	$2.79 \cdot 10^{-7}$	2.35	86^4	Rn	$1.74 \cdot 10^{-7}$	2.00
25^3	Mn	$1.35 \cdot 10^{-3}$	2.46	56^4	Ba	$1.23 \cdot 10^{-6}$	2.34	87^4	Fr	$1.78 \cdot 10^{-8}$	1.99
26^2	Fe	$2.04 \cdot 10^{-2}$	2.59	57^4	La	$1.23 \cdot 10^{-7}$	2.33	88^4	Ra	$7.54 \cdot 10^{-8}$	1.98
27^3	Co	$7.51 \cdot 10^{-5}$	2.72	58^4	Ce	$5.10 \cdot 10^{-7}$	2.32	89^4	Ac	$1.97 \cdot 10^{-8}$	1.97
28^3	Ni	$9.96 \cdot 10^{-4}$	2.51	59^4	Pr	$9.52 \cdot 10^{-8}$	2.31	90^4	Th	$8.87 \cdot 10^{-8}$	1.96
29^4	Cu	$2.18 \cdot 10^{-5}$	2.57	60^4	Nd	$4.05 \cdot 10^{-7}$	2.30	91^4	Pa	$1.71 \cdot 10^{-8}$	1.94
30^4	Zn	$1.66 \cdot 10^{-5}$	2.56	61^4	Pm	$8.30 \cdot 10^{-8}$	2.29	92^4	U	$3.54 \cdot 10^{-7}$	1.93
31^4	Ga	$2.75 \cdot 10^{-6}$	2.55	62^4	Sm	$3.68 \cdot 10^{-7}$	2.28				

Absolute flux [(m sr s TeV) $^{-1}$] at E_0 = 1 TeV/nucleus and spectral index of CR elements.
Notes: (2) from PGM; (3) from **B. Wiebel-Soth et al**., Astron. Astrophys. **330** (1998) 389; (4) from PGM after an extrapolation for ultra-heavy elements.

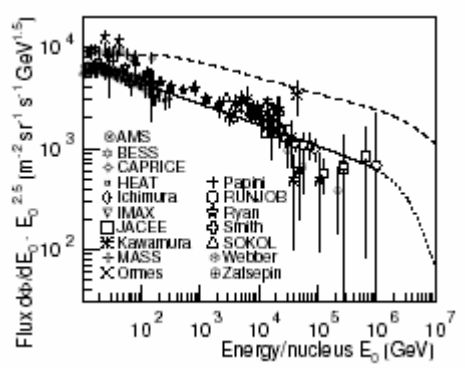

Differential energy spectrum for **protons**. The best fit to the spectrum according to a power law is represented by the solid line, the bend (dotted line) is obtained from a fit to the all-particle spectrum.

←

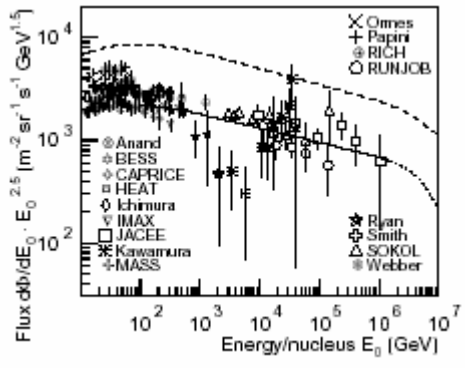

Differential energy spectrum for **helium nuclei**. The best fit to the spectrum according to a power law is represented by the solid line, the bend (dotted line) is obtained from a fit to the all-particle spectrum.

←

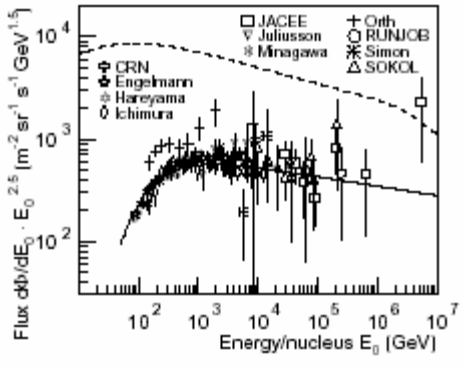

Differential energy spectrum for **iron nuclei**. The best fit to the spectrum is represented by the solid line.

←

In all 3 figures, the all-particle spectra are shown as dashed lines for reference.

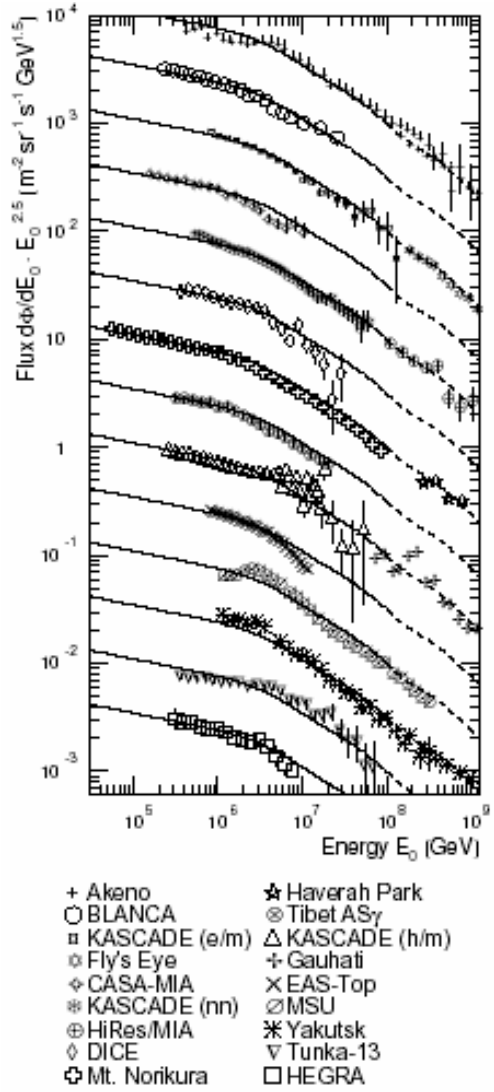

Normalized all-particle energy spectra for individual experiments compared to one of the PGM. The individual results are shifted in steps of half a decade in flux in order to reduce overlap.

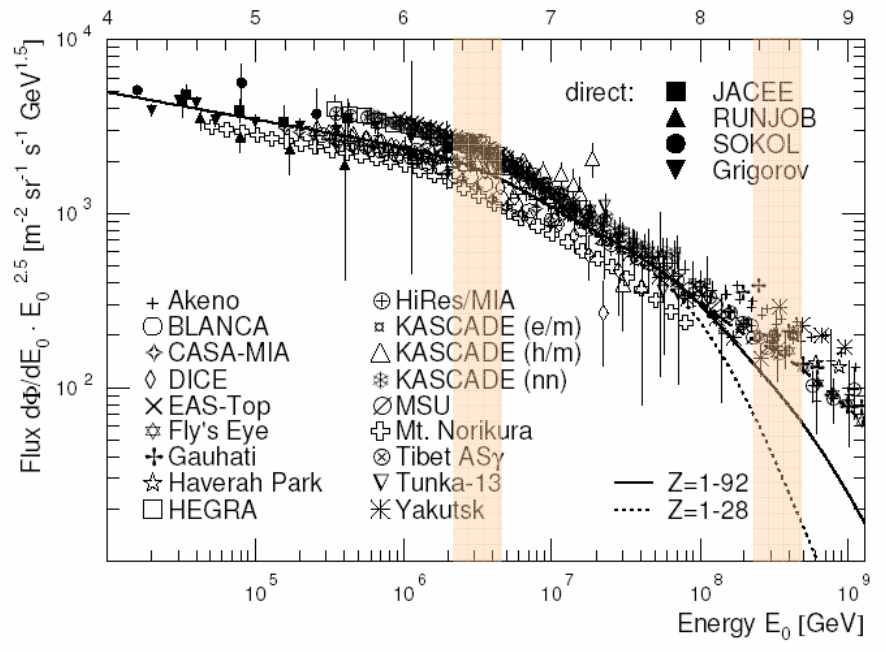

All-particle energy spectra obtained from direct and indirect measurements.

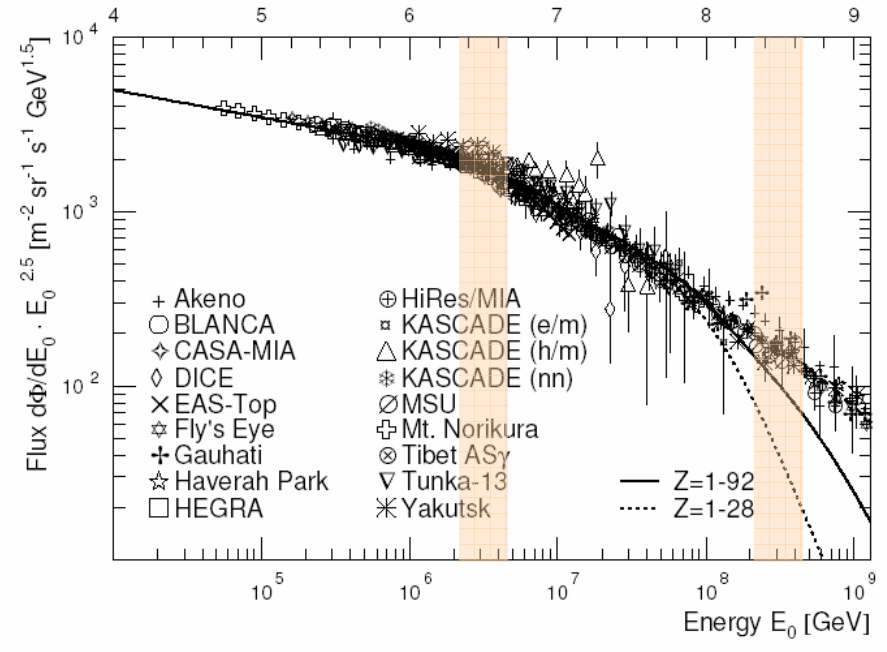

Normalized all-particle energy spectra for Individual experiments.

In both figures, the sum spectra for individual elements according to the poly-gonato model are represented by the dotted line for **1≤ Z ≤ 28** and by the solid line for **1≤ Z ≤ 92**. Above **10^8 GeV** the dashed line reflects the average spectrum.

Conclusion: The knee is explained as the subsequent cutoffs of the individual elements of the galactic component, starting with protons. The second knee seems to indicate the end of the stable elements of the galactic component.

Mean logarithmic mass vs. primary energy.

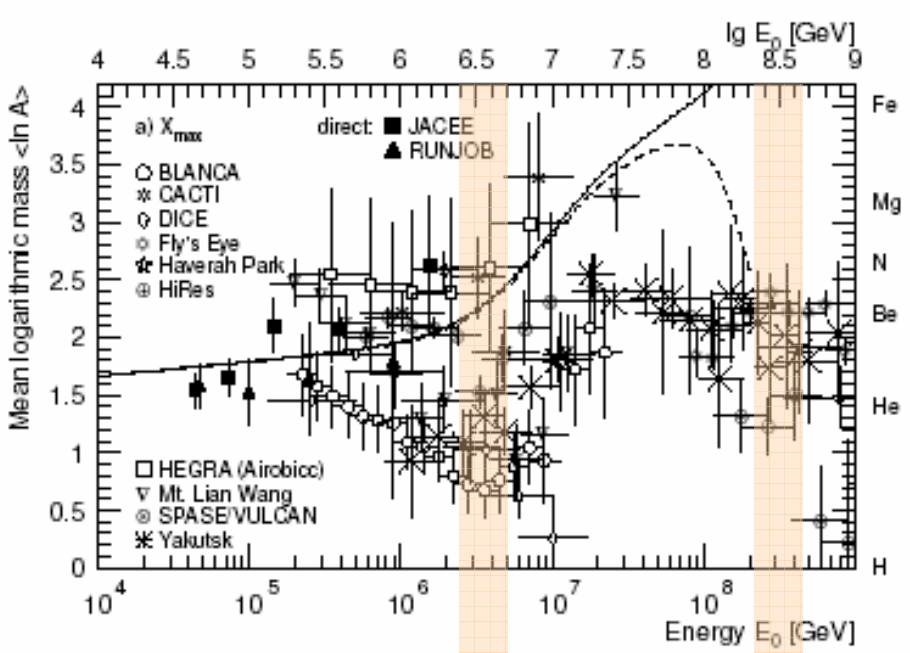

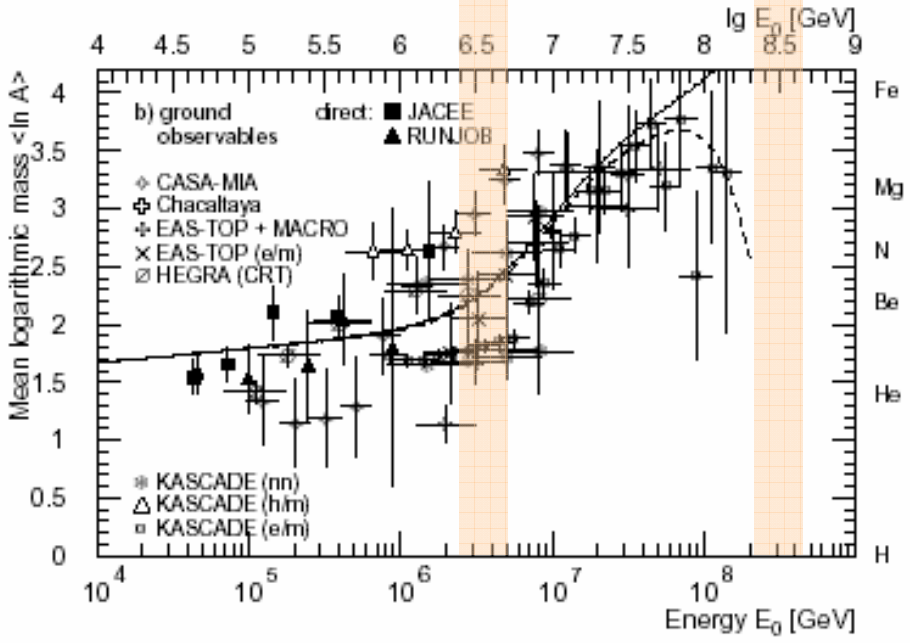

a) Results from the average depth of the shower maximum X_{max} using CORSIKA/QGSJET simulations.

b) Results from measurements of distributions for electrons, muons, and hadrons at ground level.

Results from the balloon experiments JACEE and RUNJOB are given as well. Predictions according to the PGM are represented by the solid lines. The dashed lines are obtained by introducing an *ad-hoc* component of hydrogen only.

Conclusion: The mass composition calculated with the PGM is in good agreement with results from EAS experiments measuring the electromagnetic, muonic and hadronic components at ground level. But the mass composition disagrees with results from experiments measuring the average depth of the shower maximum with Cherenkov and fluorescence detectors. If we believe the model we may conclude that **<ln A> increases around and above the knee.**

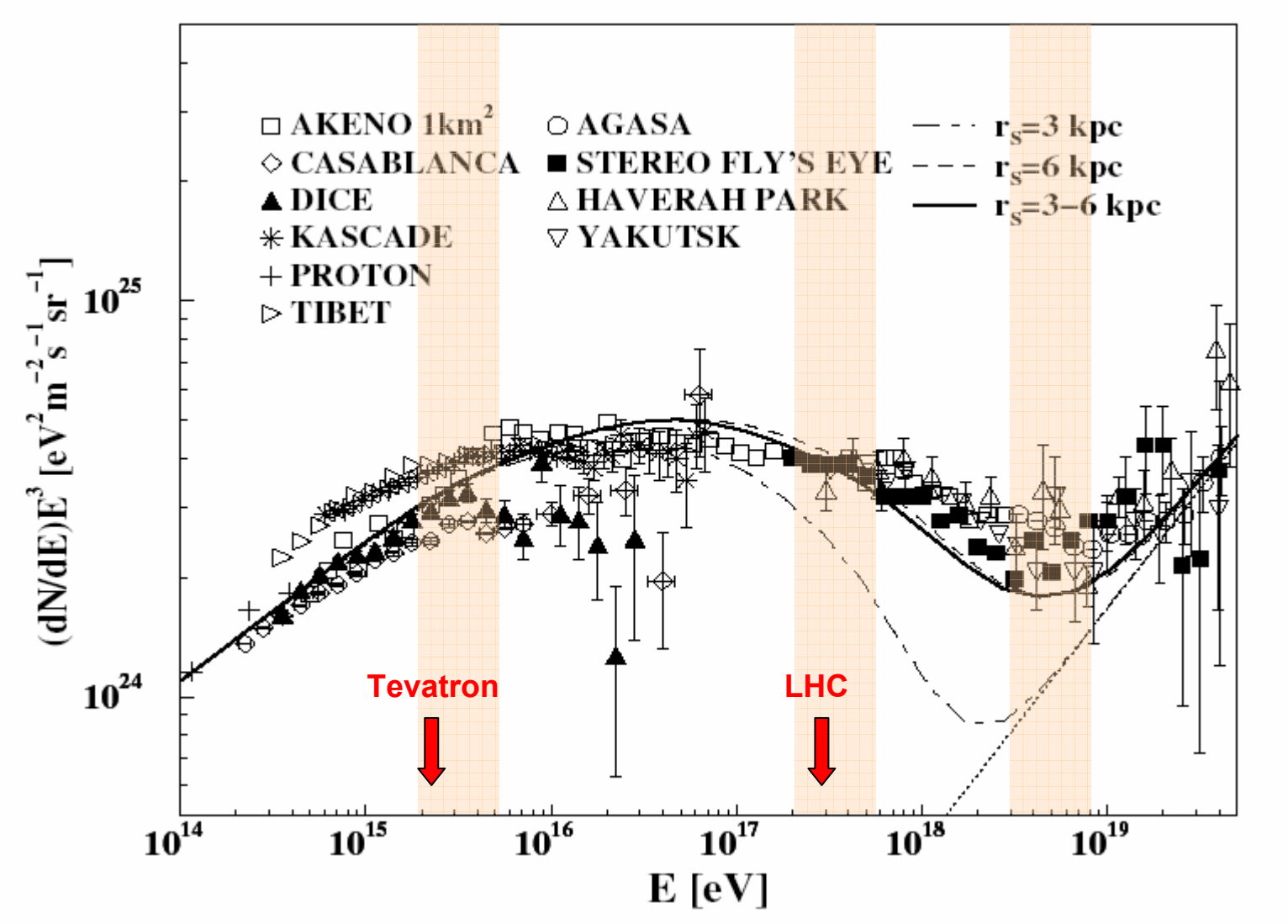

Comparison with several models from J. Candia, S. Mollerach, and E. Roulet, JCAP 05 (2003) 003 [astro-ph/0302082]. The dotted straight line corresponds to an *ad-hoc* isotropic extragalactic component with a power-law spectrum.

Electrons & Positrons

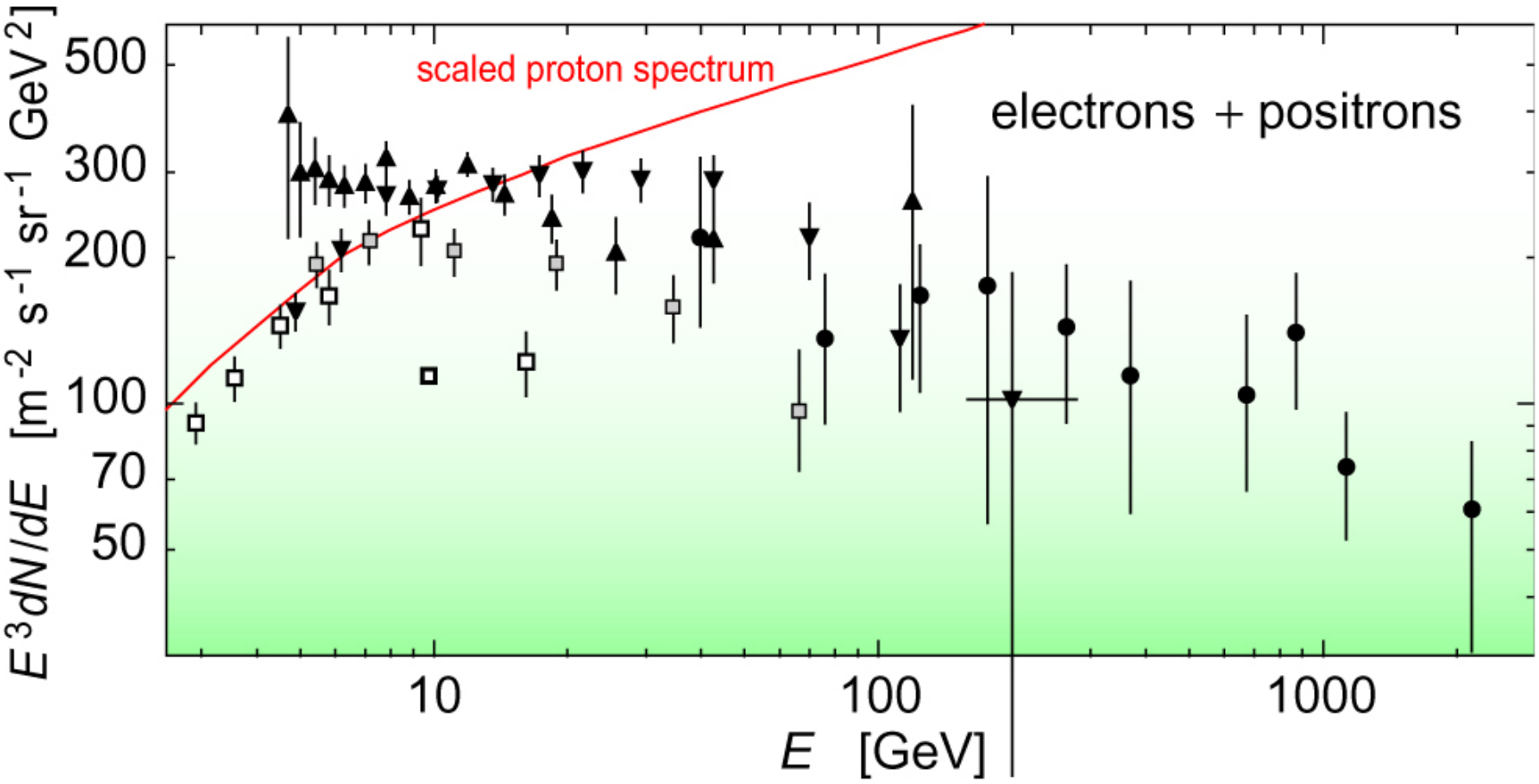

Differential energy spectrum of electrons plus positrons multiplied by E^3 (incomplete data set). The solid line shows the proton spectrum multiplied by 0.01.

[**Reference**: T.K. Gaisser & T. Stanev, "Cosmic rays," pages 228-234 of the Review of Particle Physics, Phys. Lett. B **592** (2004) 1.]

LIS of CR electrons and positrons[a]

The CR spectra $F_a(E,r,t)$ or $F_a(R,r,t)$ measured in the Solar System are in general some functionals of the Local Interstellar Spectra (LIS). For example, in the spherical isotropic model of cosmic ray diffusion through the heliosphere,[b] the relation is

$$F_a(R,r,t) = \left[\frac{R}{R_a(t)}\right]^2 F_a^{\mathrm{LI}}(R_a(t)),$$

where $F_a^{\mathrm{LI}}(R)$ is the LIS (assumed to be isotropic and time-independent),

$$R_a(t) = \frac{1}{Z_a|e|}\sqrt{[E+\Delta E_a(t)]^2 - m_a^2}$$

is the local interstellar rigidity of the particle a and

$$\Delta E_a(t) = Z_a|e|\phi_a(t)$$

is the energy lost by the particles during their travel, which is proportional to the solar modulation parameter, $\phi_a(t)$. This parameter can be expressed as function of the diffusion coefficient and the solar wind velocity, even though usually it is considered a free parameter to be measured.

[a] Here we will mainly follow to D. Casadei and V. Bindi, astro–ph/0302307.

[b] E. N. Parker, Planet. Space Sci. **13** (1965) 9; L. J. Gleeson and W. I. Axford, ApJ **149** (1967) L115; ApJ **154** (1968) 1011.

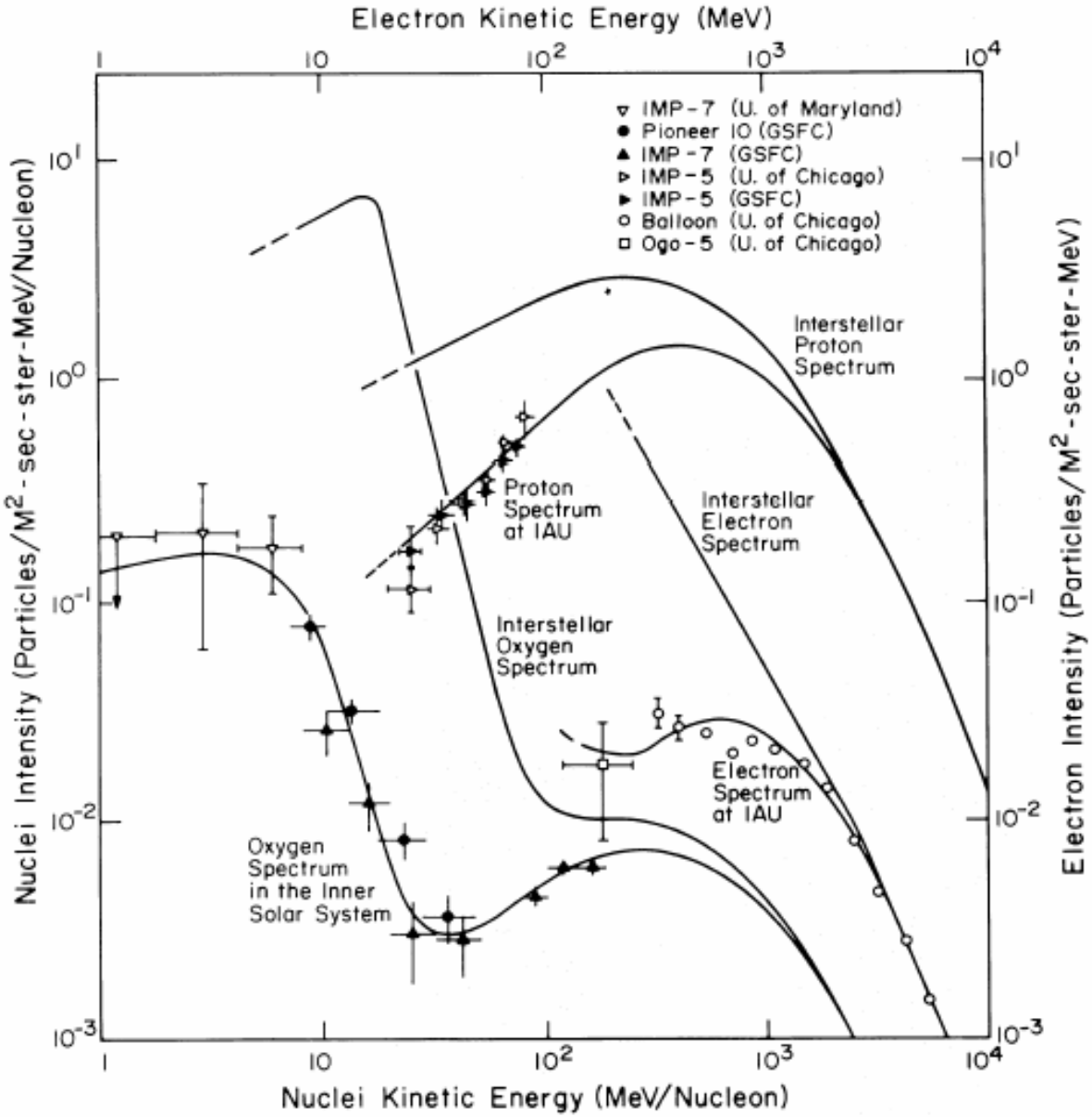

A numerical solution to the Parker-Gleeson-Axford equation for modulated spectra of protons, electrons, and oxygen. The particles undergo a diffusive-like propagation in which trapping between time-varying constituents in the interplanetary magnetic field controls the particle motion.

[**Reference**: L. Fisk, ApJ **206** (1976) 333.]

DIRECT MEASUREMENTS OF COSMIC RAY ELECTRONS AND POSITRONS

MEASUREMENT	YEAR	ϕ (MV)	SUN POLARITY	e^-/e^+ SEPARATION	E_{min} (GeV)	E_{max} (GeV)	REFERENCES e^-	REFERENCES e^+	REFERENCES p^+	NOTES
Fanselow et al. (1969)	1965, 1966	570(50)	−	Y	0.07	11.0	1	1	...	a
Nishimura et al. (1980)	1968–1975	700(200)	−, +	N	30.0	1500	2	...	...	a
Meegan & Earl (1975)	1969, 1973	650(100)	+	N	6.4	114	3	...	...	a
Buffington et al. (1975)	1972, 1973	650(50)	+	Y	5.1	63.0	4	4	...	a
Prince (1979)	1975	550(50)	+	N	10.2	202	5	...	...	a
Golden et al. (1984, 1987)	1976	500(50)	+	Y	3.45	91.7	6	7	...	a
Tang (1984)	1980	900(200)	+	N	4.89	200	8	...	...	a
MASS 89	1989	1400(50)	−	Y	1.6	16.1	9	9	10	b
MASS 91	1991	2000(200)	+	Y	7.5	46.9	11	11	12	b
CAPRICE 94	1994	664(5)	+	Y	0.54	34.3	13	13	14	b
HEAT 94	1994	650(50)	+	Y	5.45	66.4	15	15	...	c
HEAT 95	1995	550(50)	+	Y	1.20	66.4	15	15	...	a
Nishimura et al. (2001)	1996, 1998	600(100)	+	N	30.0	3000	16	...	...	a, c
BETS 97+98	1997, 1998	600(100)	+	N	13.9	112.6	17	...	...	a, c
AMS 98	1998	632(13)	+	Y	0.15	35.7	18	18	19	b

NOTES.—The value of the solar modulation parameter ϕ was estimated using: (a) neutron rates; (b) the proton spectrum measured by the same detector; and (c) the proton spectrum measured by a different detector in the same period. Positive and negative solar polarities refer to epochs when the magnetic field emerging from the north pole of the Sun points outward and inward, respectively (Bieber et al. 1999). The energy range is reported for electrons only.

REFERENCES.—(1) Fanselow et al. 1969; (2) Nishimura et al. 1980; (3) Meegan & Earl 1975; (4) Buffington et al. 1975; (5) Prince 1979; (6) Golden et al. 1984; (7) Golden et al. 1987; (8) Tang 1984; (9) Golden et al. 1994; (10) Webber et al. 1991; (11) Grimani et al. 2002; (12) Bellotti et al. 1999; (13) Boezio et al. 2000; (14) Boezio et al. 1999; (15) Du Vernois et al. 2001; (16) Nishimura et al. 2001; (17) Torii et al. 2001; (18) Alcaraz et al. 2000a; (19) Alcaraz et al. 2000b.

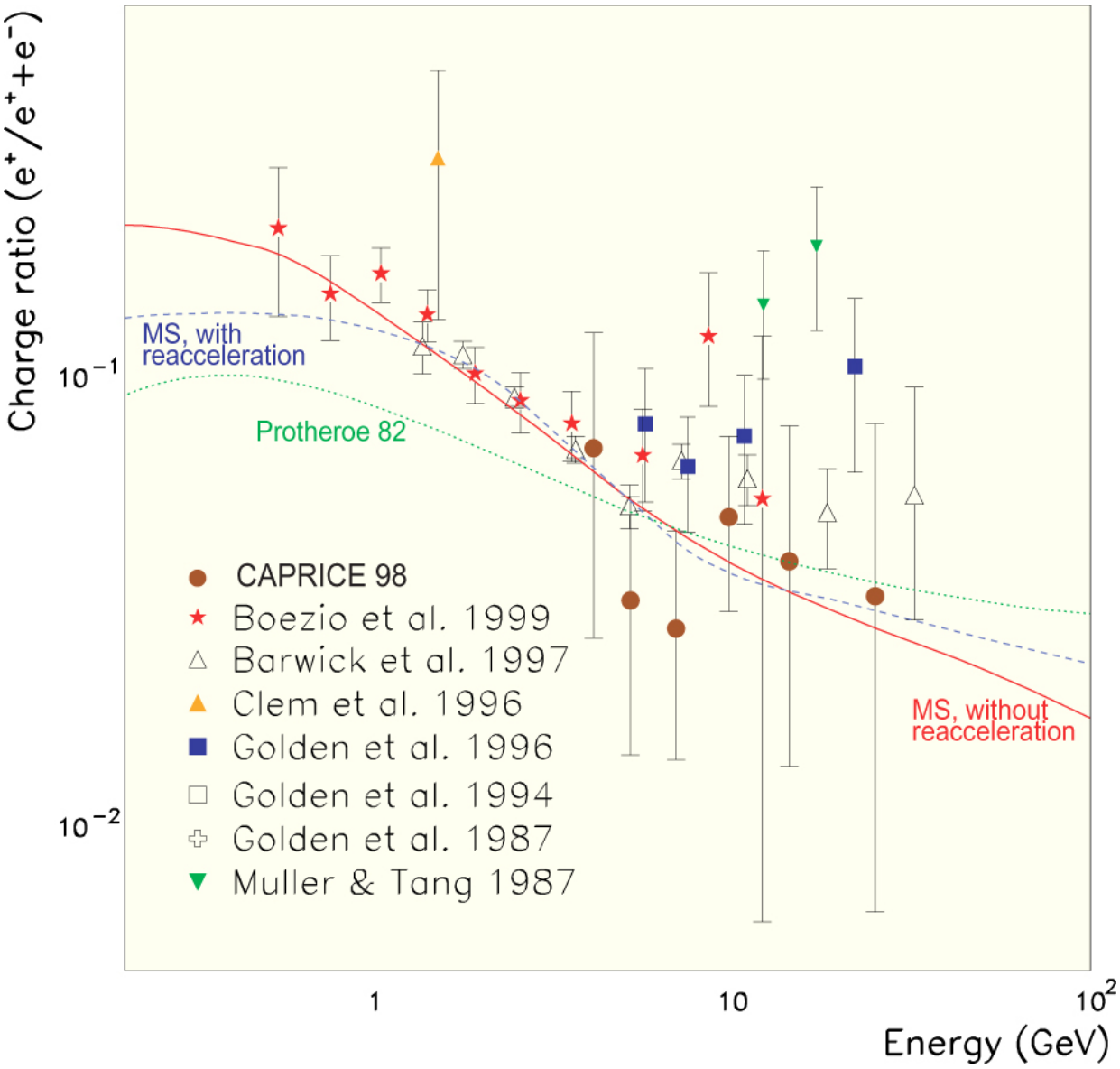

The positron fraction as a function of energy measured by CAPRICE 98 (closed circles) and several other experiments. The dotted line is the secondary positron fraction calculated by R.J. Protheroe [ApJ **254** (1982) 391], the dashed and solid lines are the secondary positron fraction calculated by I.V. Moskalenko and A.W. Strong [ApJ **493** (1998) 694] with and without reacceleration of cosmic rays, respectively.

[**Reference:** M. Boezio et al. (WiZard - CAPRICE98 Collaboration), ICRC'26,OG.1.1.16.]

Note: These data are not included into the fit under discussion.

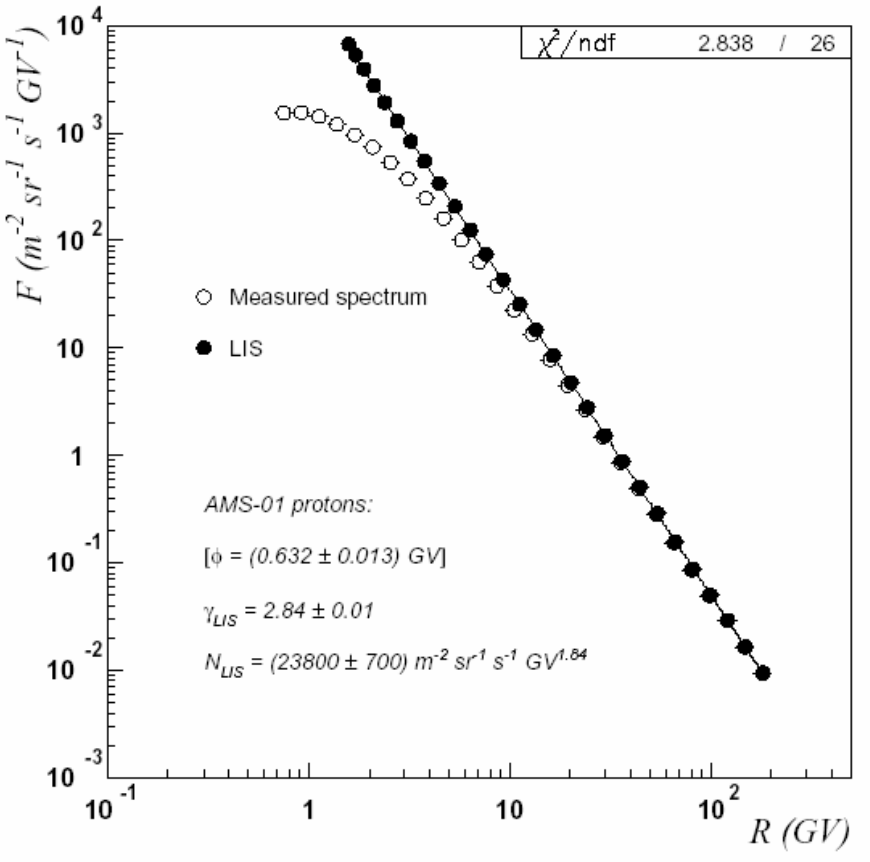

Measured and local interstellar flux of AMS-01 protons.

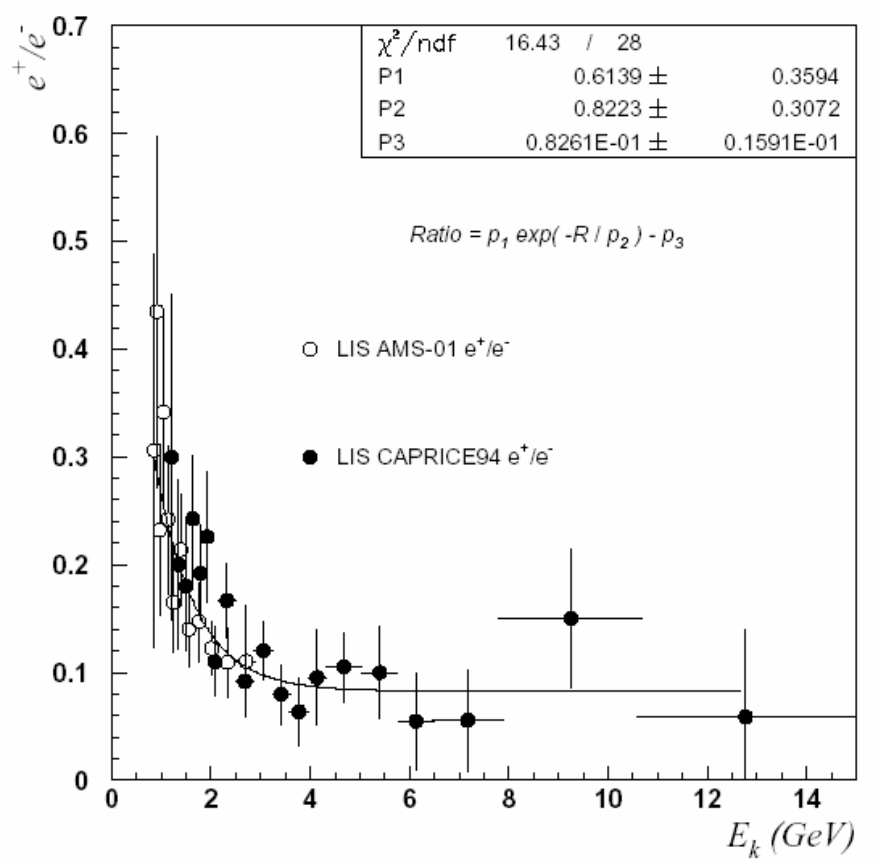

Local interstellar **e^+/e^- ratio** measured by AMS-01 and CAPRICE 94.

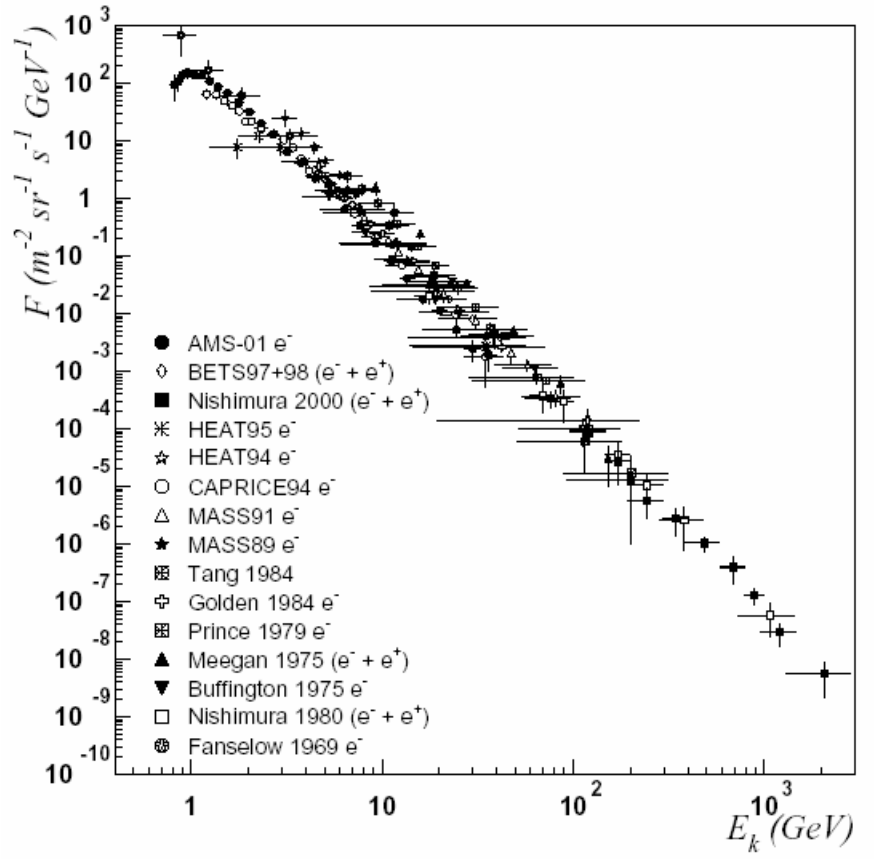

LIS of **e^+** and **e^-** measured by all considered experiments.

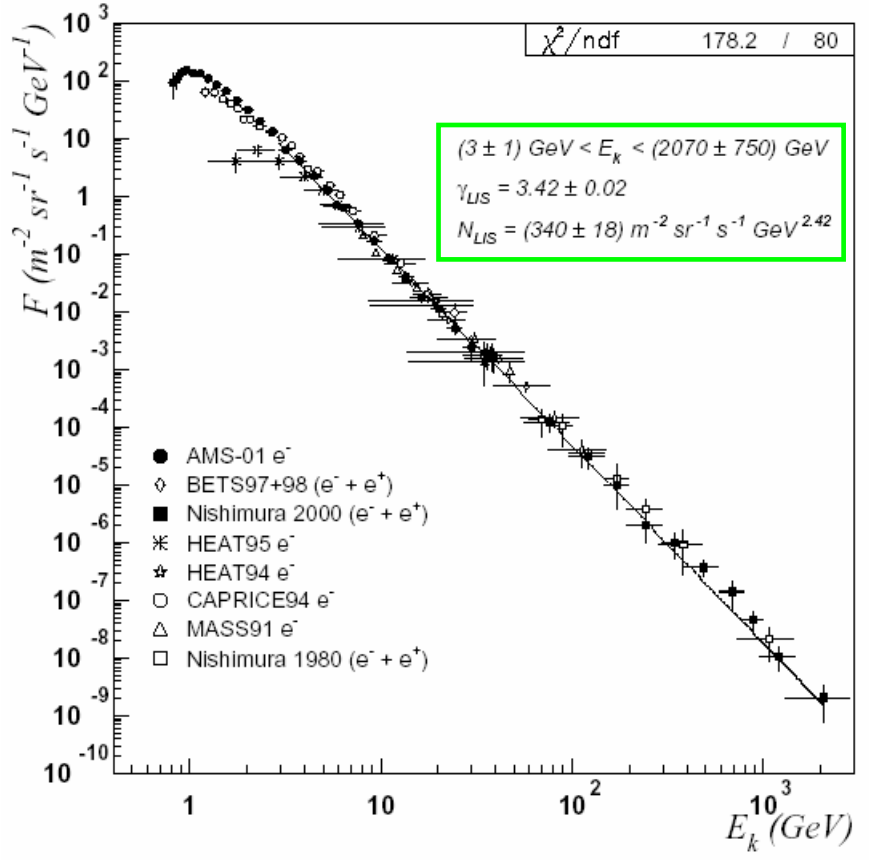

LIS of **e^+** and **e^-** measured by all considered experiments, after renormalization to the AMS-01 and CAPRICE 94 flux at 20 GeV, with a single power-law fit.

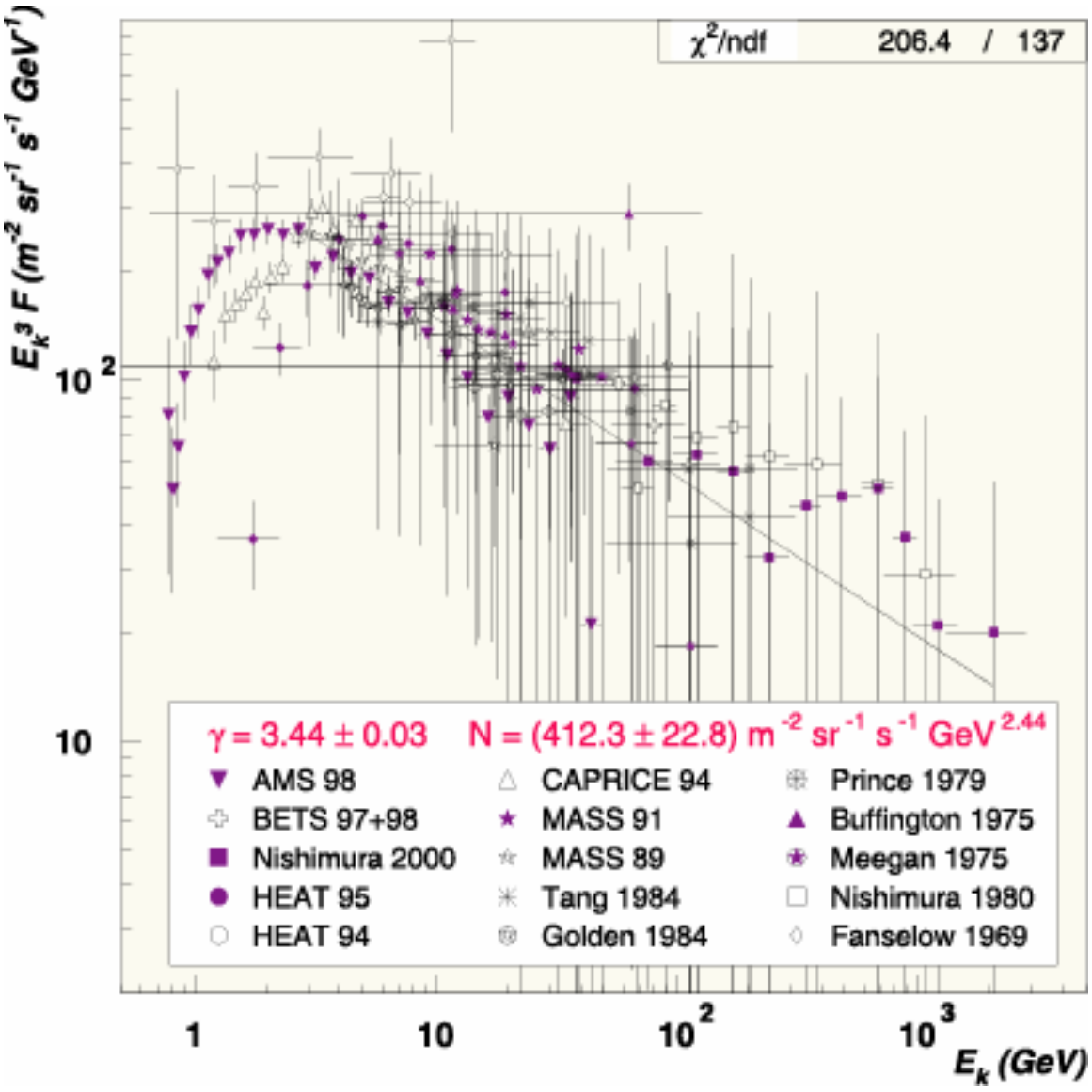

The final (published) result: the single power-law fit of the electron Local Interstellar Spectrum (multiplied by E_k^3), after the rescaling.

The obtained spectral index is 3.44 +/- 0.03 between ~3 GeV and ~2 TeV.

[**Reference**: D. Casadei & V. Bindi, "The origin of cosmic ray electrons and positrons," ApJ **612** (2004) 262-267.]

Note: This published version is formally more accurate in comparison with the e-print one. If true, the analysis suggests that the experimental data are self-contradictory and cannot be described by a single power law.

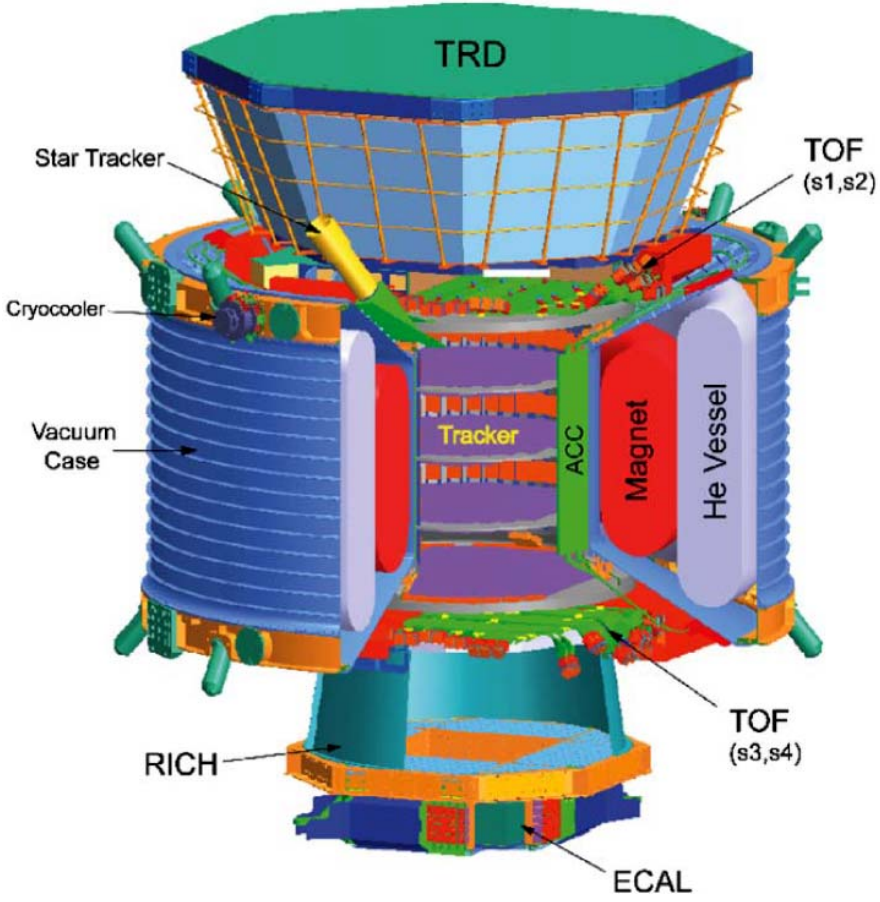

The AMS-02 detector configuration

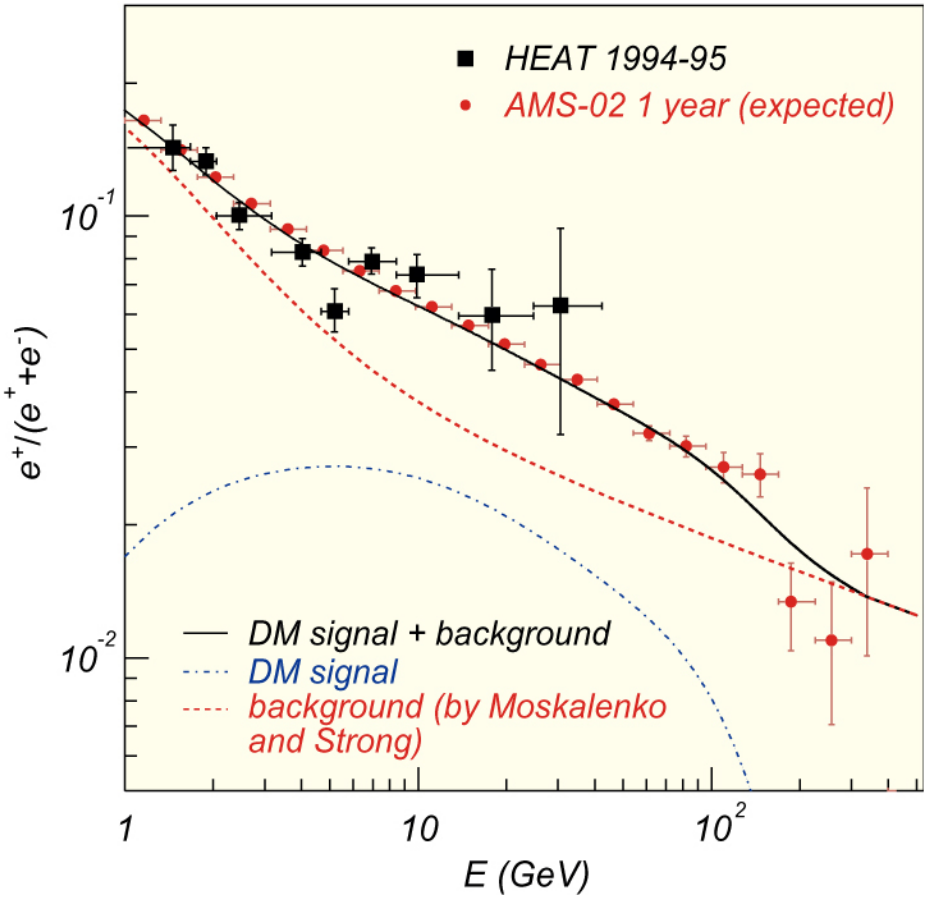

The expected positron fraction accuracy from the AMS-02 after 1 year on the ISS compared to available data from the HEAT collaboration. The error bars reflect the particle identification power estimated from AMS subdetector beam test data.

[From Ph. v. Doetinchem et al., "Performance of the AMS-02 transition radiation detector," Nucl. Instrum. Meth. A **558** (2006) 526–535.]

Antiprotons and antinuclei in CR

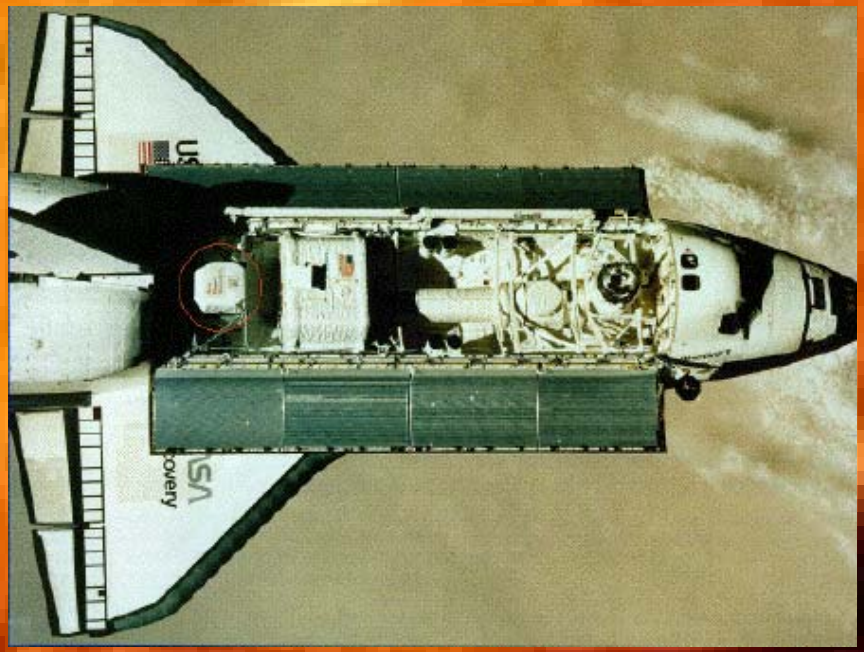

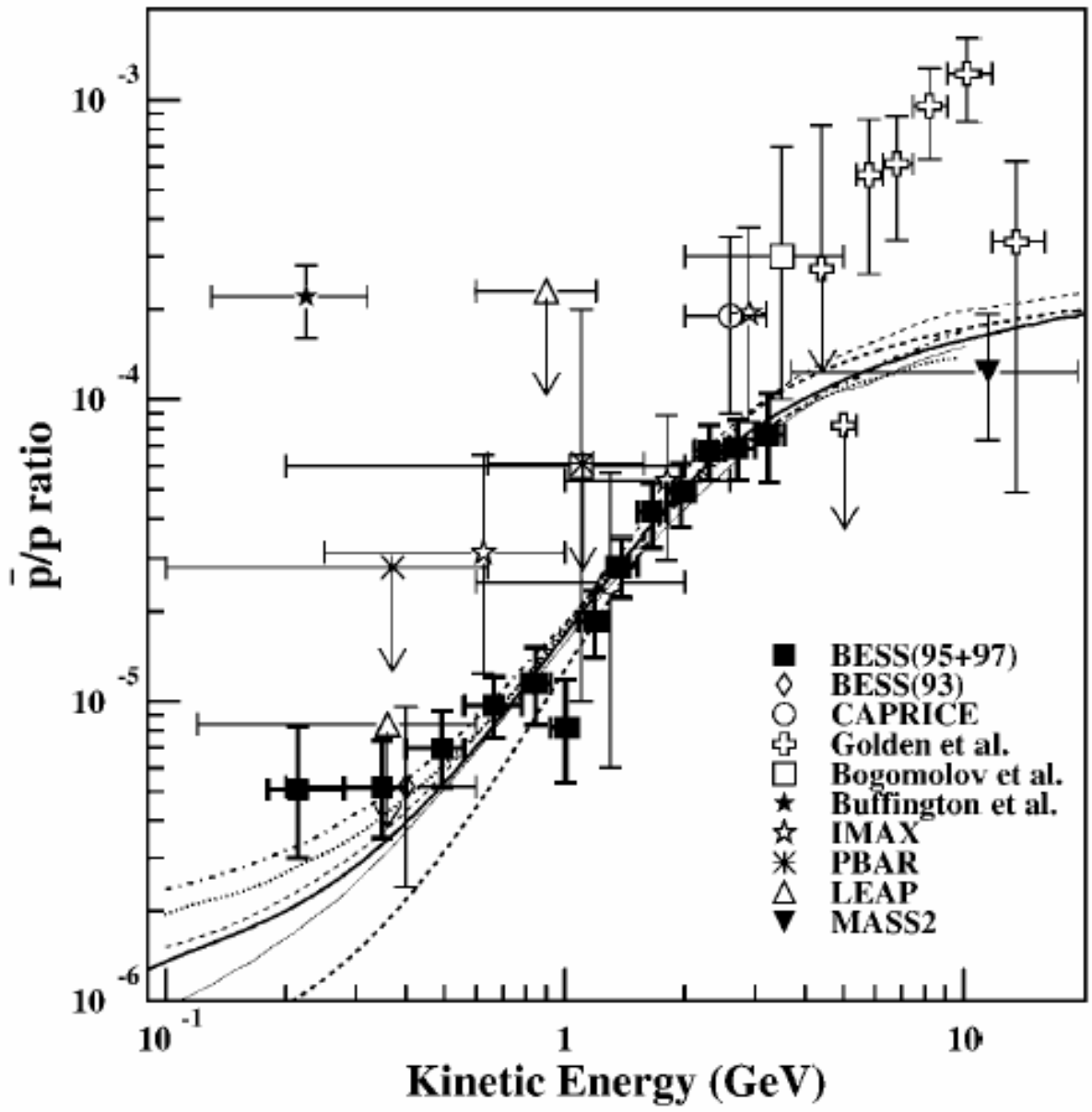

CR antiproton to proton ratio measured in different experiments.

[**Reference**: S. Orito et al. (BESS Collaboration), Phys. Rev. Lett. **84** (2000) 1078.]

Antiproton flux measurements with the L3 detector at LEP CERN

The L3+C: Muon detector

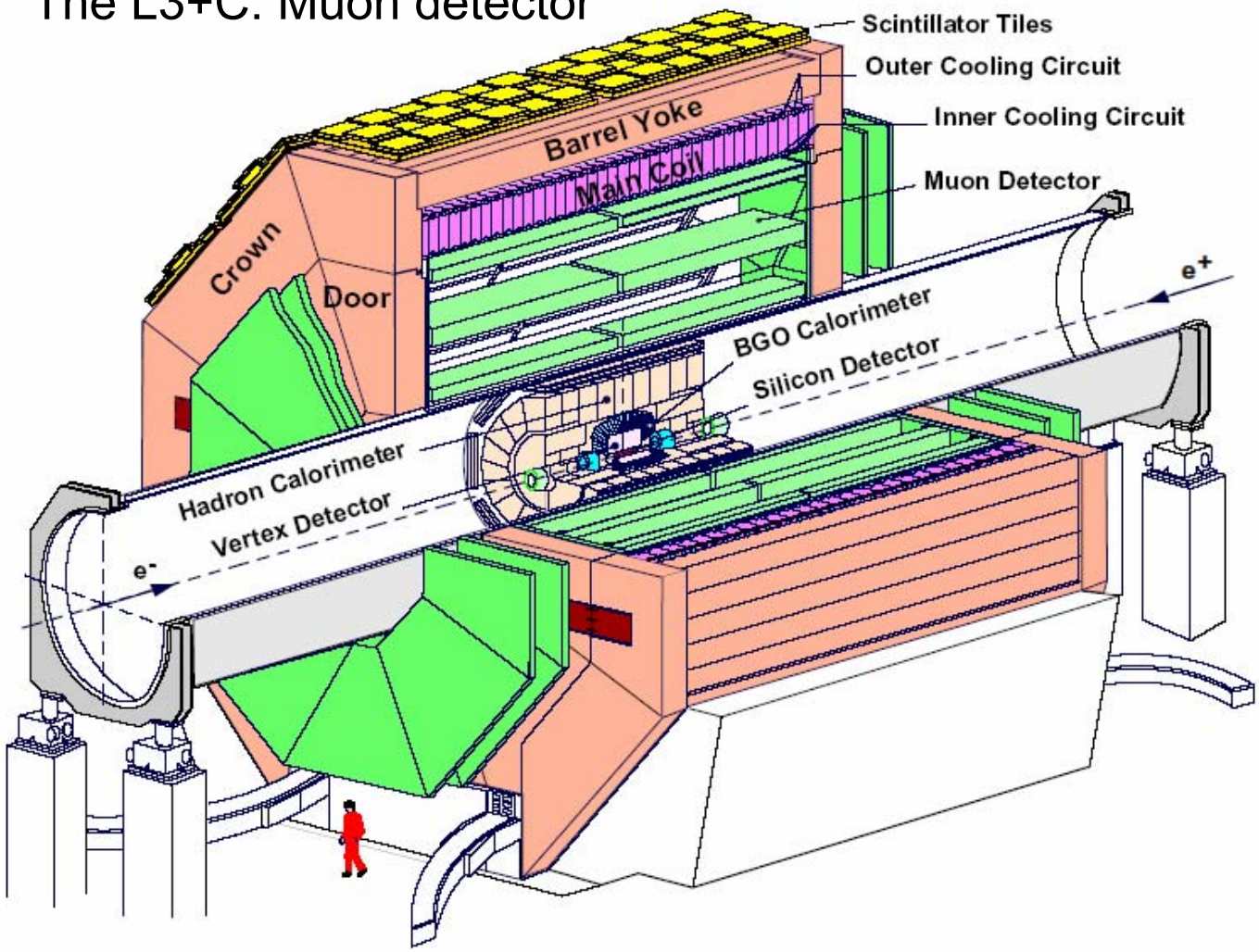

- 30 m below the surface,
- drift chambers in 1000 m^3 magnetic volume (0.5T),
- 200 m^2 scintillator area,
- data acquisition independent from L3,
- 11 billion muon triggers collected.

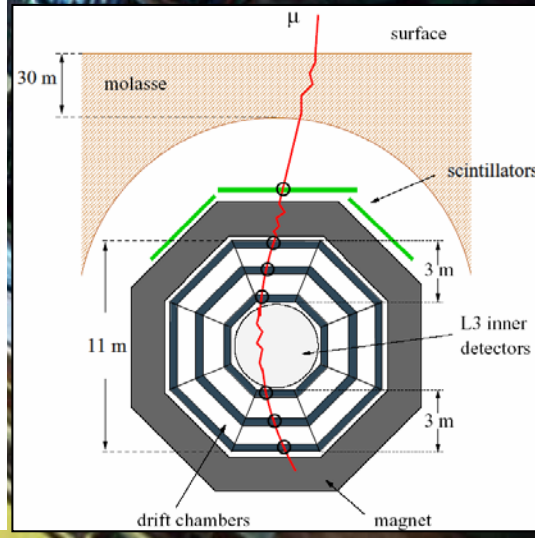

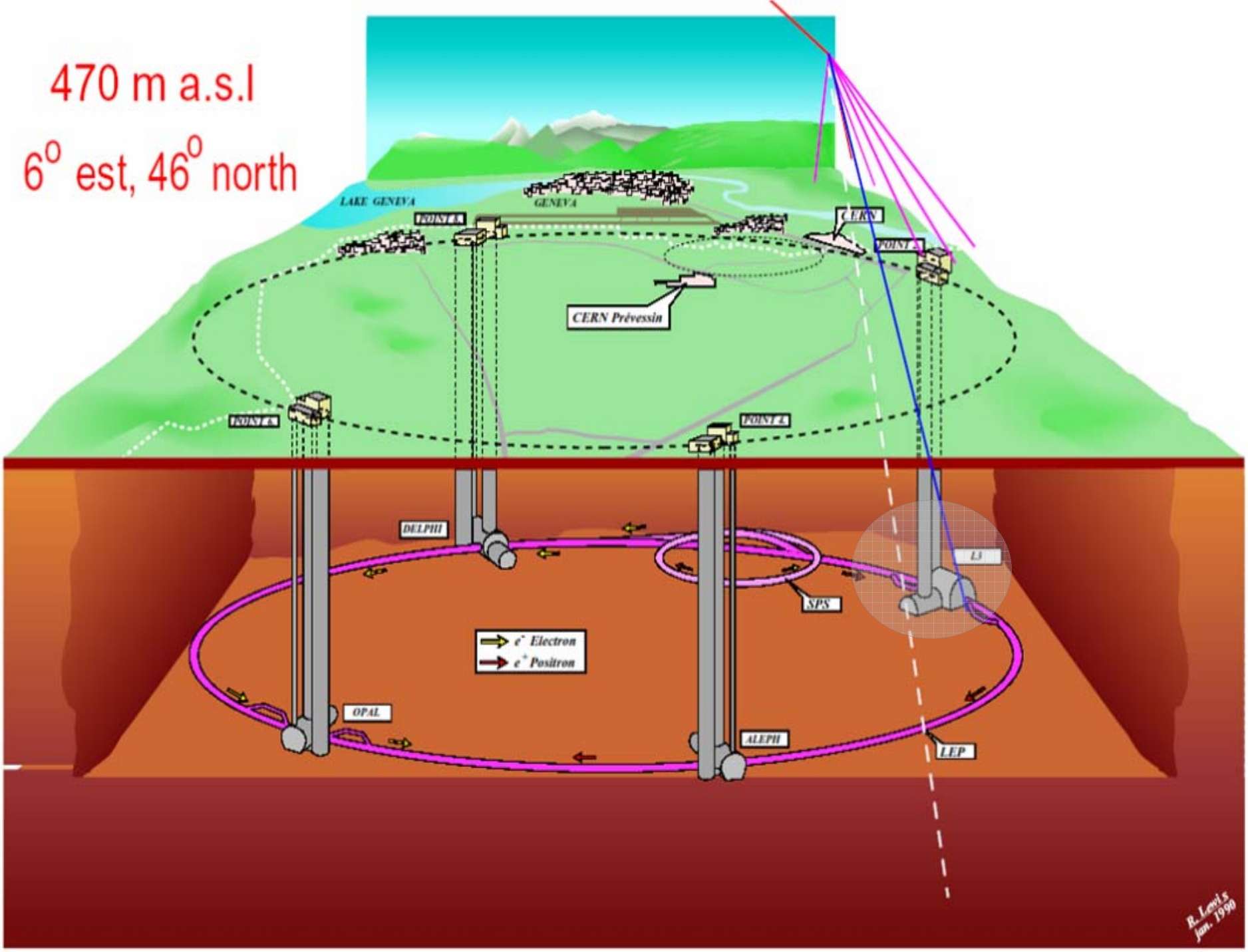
470 m a.s.l
6° est, 46° north
LAKE GENEVA
GENEVA
POINT 8
CERN
POINT 1
CERN Prévessin
POINT 6
POINT 4
DELPHI
L3
SPS
e⁻ Electron
e⁺ Positron
OPAL
ALEPH
LEP
R. Lenis
Jan. 1990

The L3+C: Air Shower Array

47 scintillators ($50\times50\times1 cm^3$), area = 1800 m^2, offline coincidence with muon detector (27×10^6 triggers)

Moon Shadow

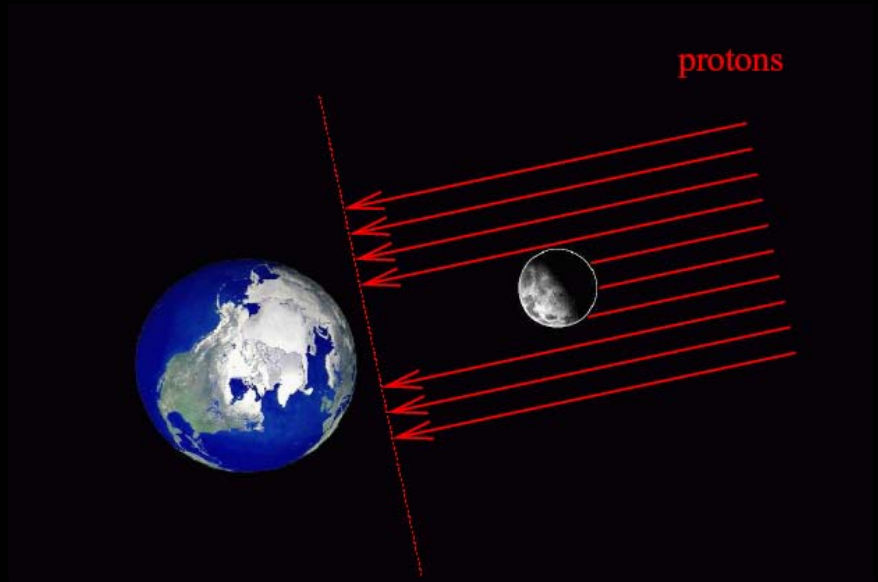

The moon is an absorber for primary cosmic rays. Therefore the moon shadow can be used for verification of experimental pointing accuracy.

The earth magnetic field shadow shifts from optical moon position eastwards for protons and westwards for antiparticles ("anti shadow").

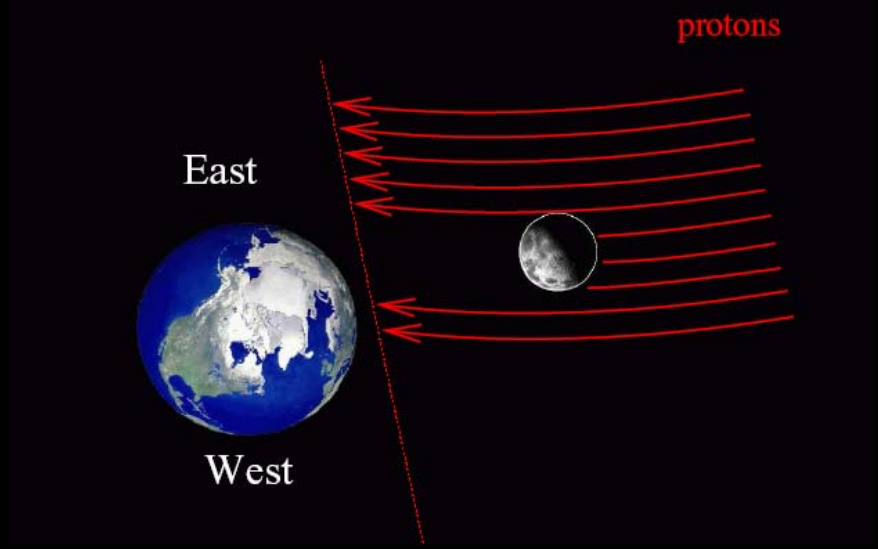

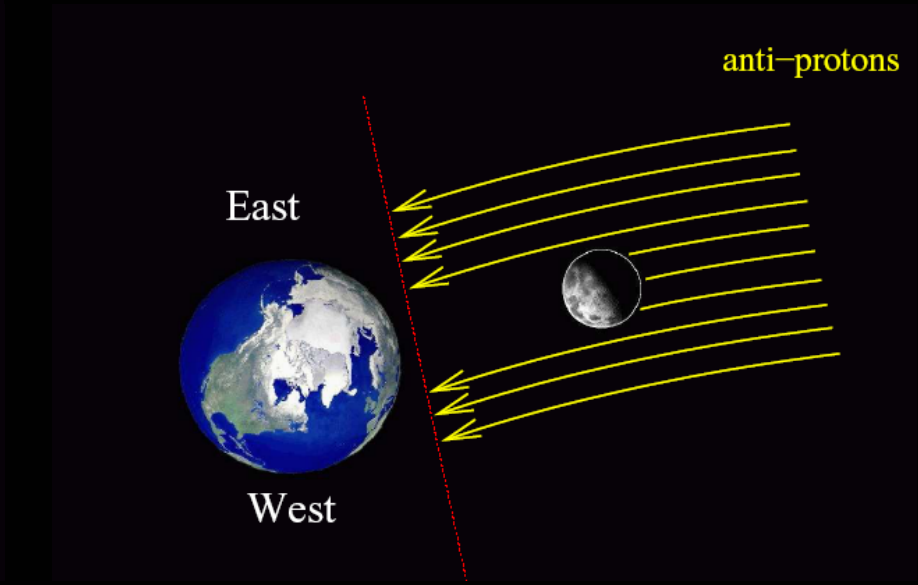

Pointing precision - The Earth-Moon system as a spectrometer

Cosmic rays are blocked by the Moon.
$\Longrightarrow$ deficit of cosmic rays when looking at the Moon (Clark 1957).

- Size of the deficit $\longrightarrow$ effective angular resolution
- Position of the deficit $\longrightarrow$ pointing error

Geomagnetic field: positively charged particles deflected towards the East and negatively charged particles towards the West. $\Longrightarrow$ ion spectrometer

- Advantage of L3+C:
  - Excellent angular resolution and pointing
  - Precise momentum measurement
  - Low p_{min} (high rate, large deflection)
  - Real sensitivity on the earth magnetic field.

Pointing precision: obtained from the comparison of the observed Moon shadow in the local coordinate system and a Monte Carlo simulation. $\Rightarrow$ $< 0.1^\circ$

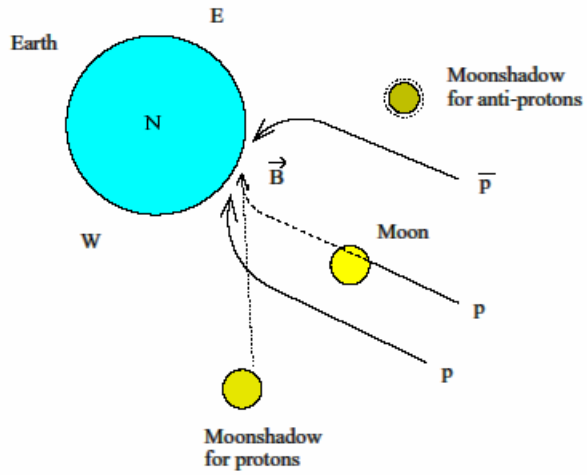

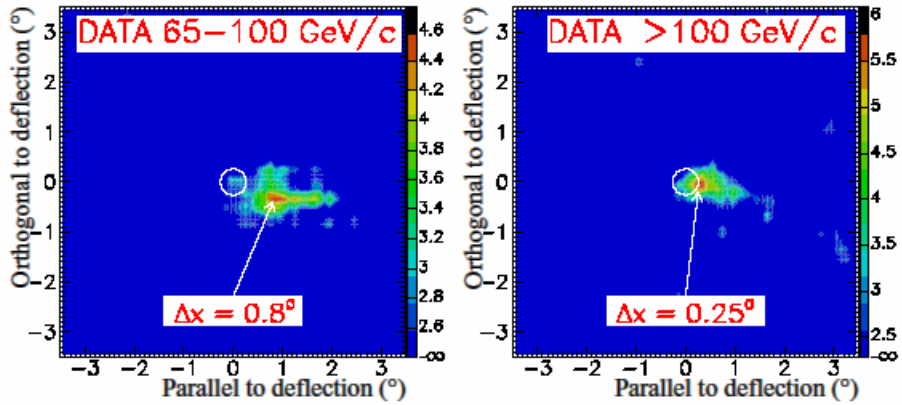

Shadow (in deflection coordinate system)

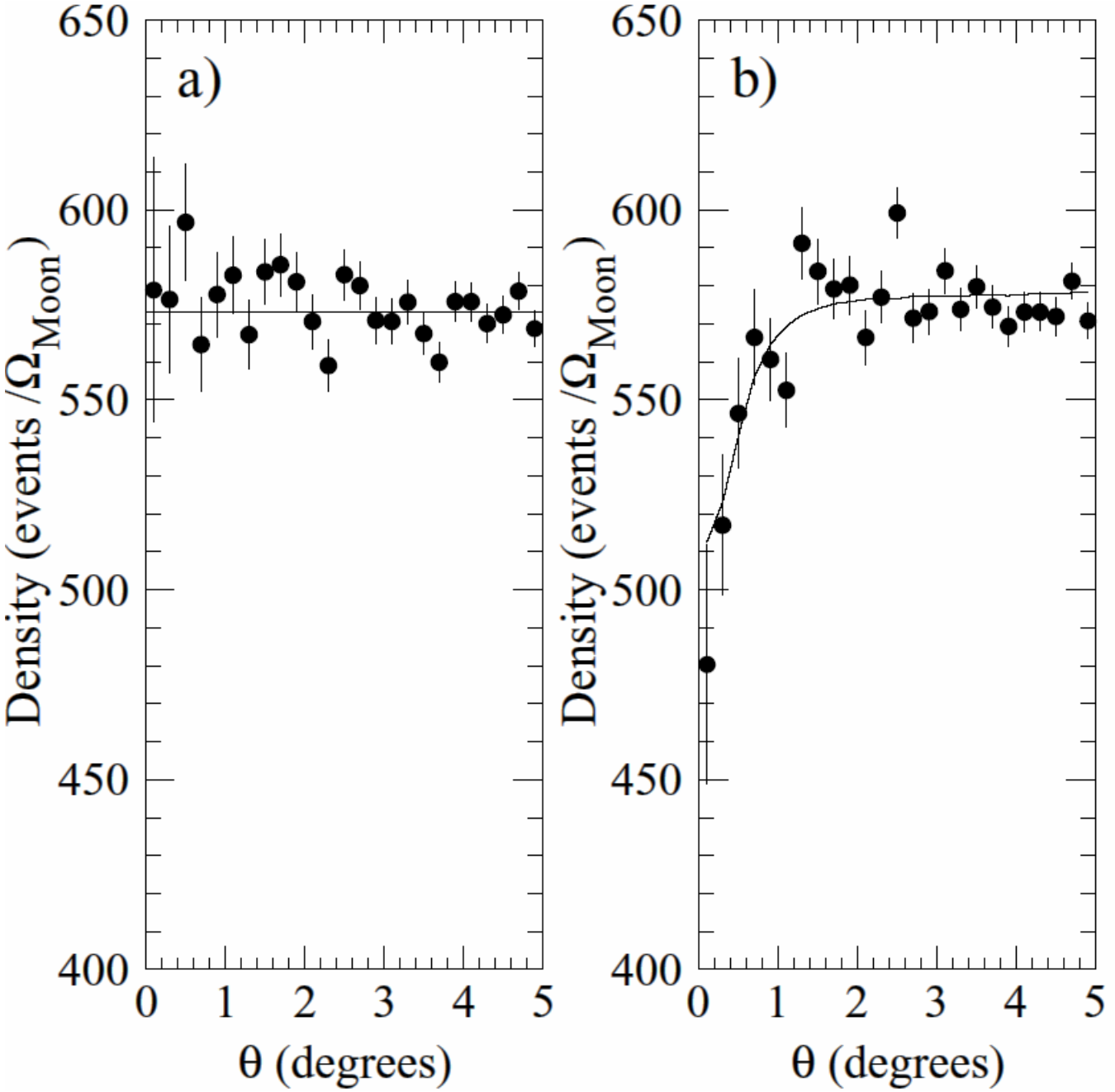

Angular distributions for events/Moon-solid-angle with E > 100 GeV,

(a) for a ‘‘fake Moon’’ shifted 1 hour behind its real position,

(b) using the correct Moon position.

Solid lines are the results of the simulation, including the angular resolution deduced from the study of di-muon events.

[Reference: P. Achard et al. (L3 Collaboration), Astropart. Phys. **23** (2005) 411–434 (astro-ph/0503472).**]**

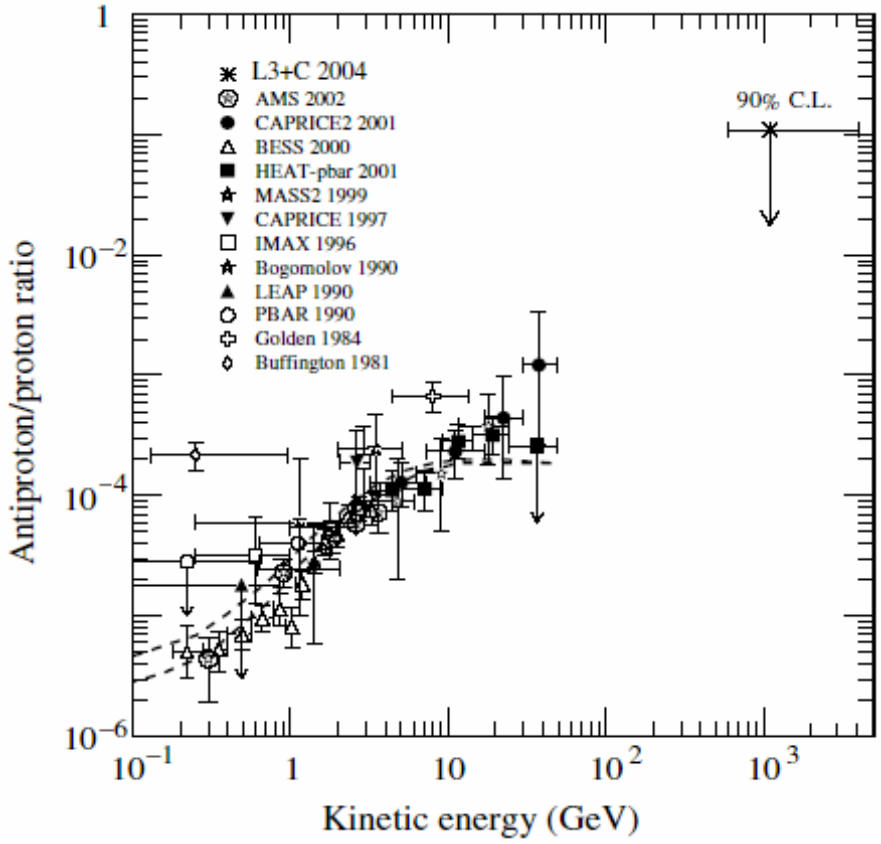

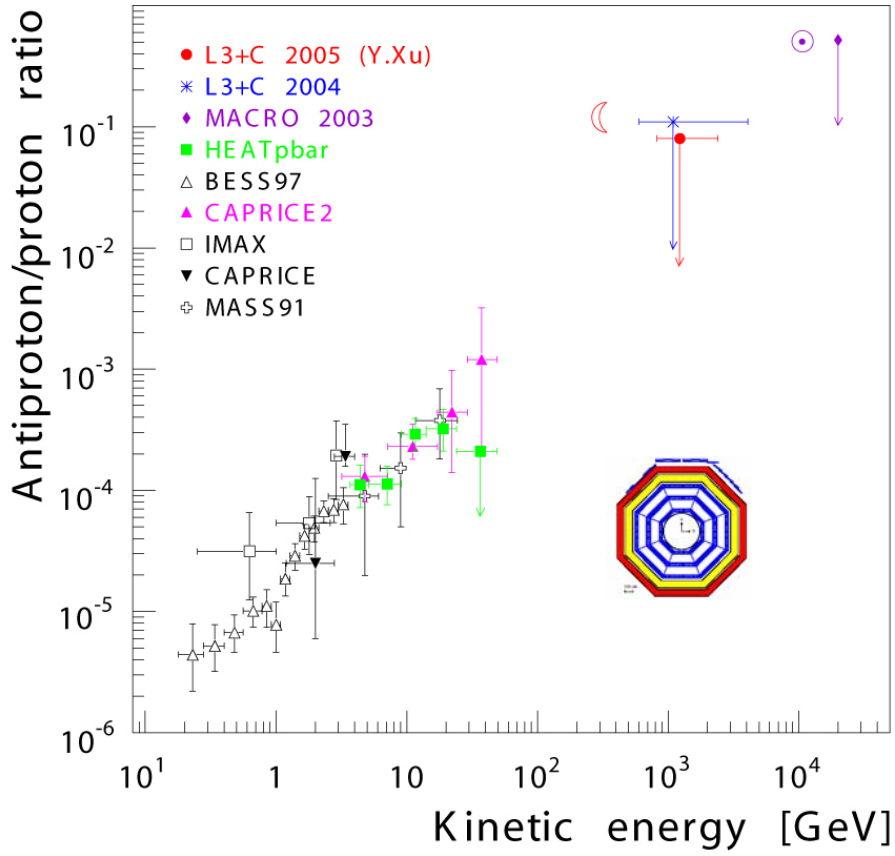

Measurements of the ratio of the antiproton and proton fluxes versus the primary energy, including the L3+C limit around 1 TeV. The dashed lines (left) show the range of the theoretical expectations according to I.V. Moskalenko, Astrophys. J. **565** (2002) 280. An upper limit obtained in the MACRO experiment at Gran Sasso [M. Ambrosio et al. (MACRO Collaboration), Astropart. Phys. **20** (2003) 145-156 (astro-ph/0302586)] from observation of the moon and sun shadows is also shown (right).

[**References**: P. Achard et al. (L3 Collaboration), Astropart. Phys. **23** (2005) 411–434 (astro-ph/0503472); Yupeng Xu, PhD, ETH Zürich (2005).]

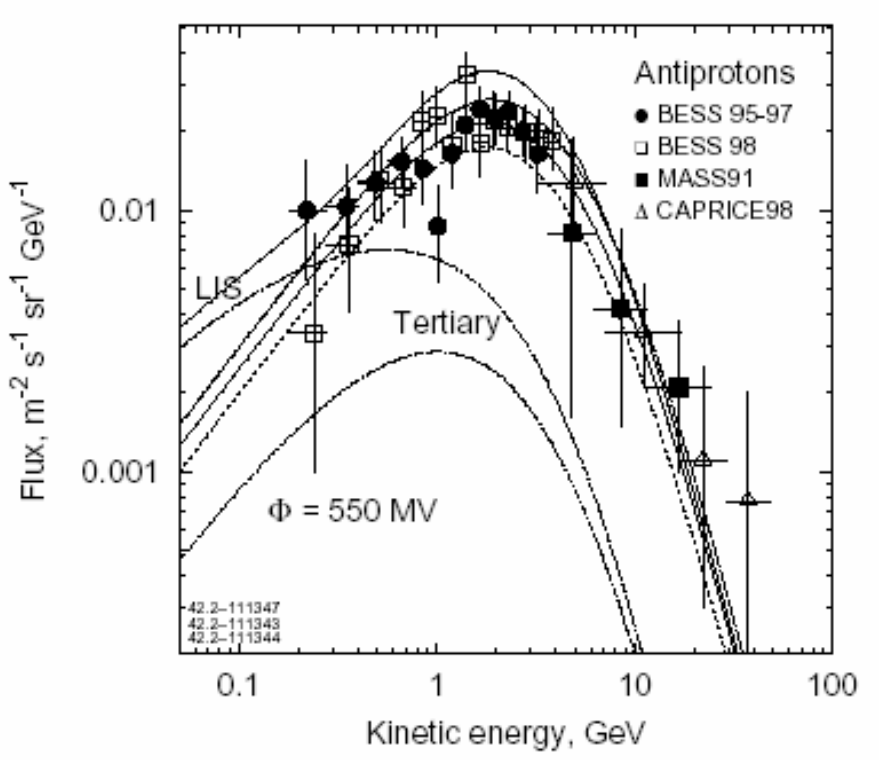

Calculated antiproton flux in a model with the spatial diffusion coefficient $D_{xx} = \beta D_0 (\rho/\rho_0)^{\delta}$; for $\delta = 0.47$ and different normalization factors D_0 ($\times 10^{28}$ cm s^{-2}). ***Solid curves*** – $D_0 = 3.3$ at $\rho_0 = 3$ GV, upper curve – local interstellar spectrum (LIS), lower curve – modulated (with modulation parameter of 550 MV). ***Dots*** – $D_0 = 2.6$, ***dashes*** – $D_0 = 4.3$.
Data: BESS 95-97 (Orito et al., 2000), BESS 98 (Asaoka et al., 2002), MASS 91 (Basini et al., 1999), CAPRICE 98 (Boezio et al., 2001).

[**Reference**: I.V. Moskalenko et al., ApJ **586** (2003) 1050.]

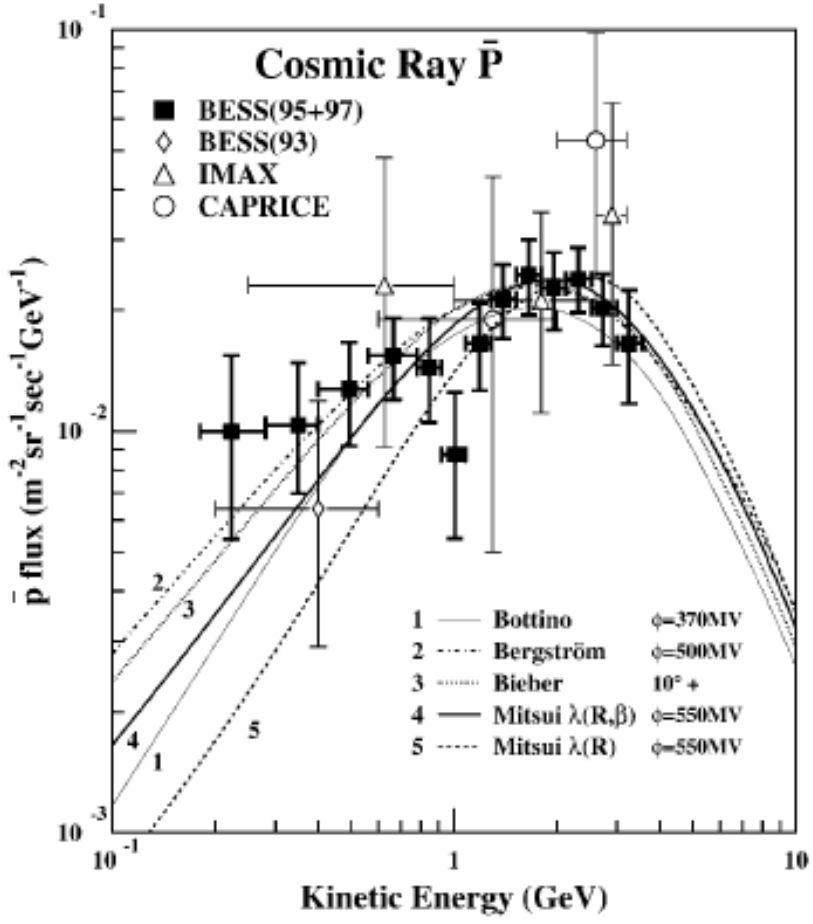

BESS 1995 and 1997 (solar minimum) antiproton fluxes at the top of the atmosphere together with previous data. The curves are recent calculations of the secondary antiproton spectra for the solar minimum period.

[**Reference**: S. Orito et al. (BESS Collaboration), Phys. Rev. Lett. **84** (2000) 1078.]

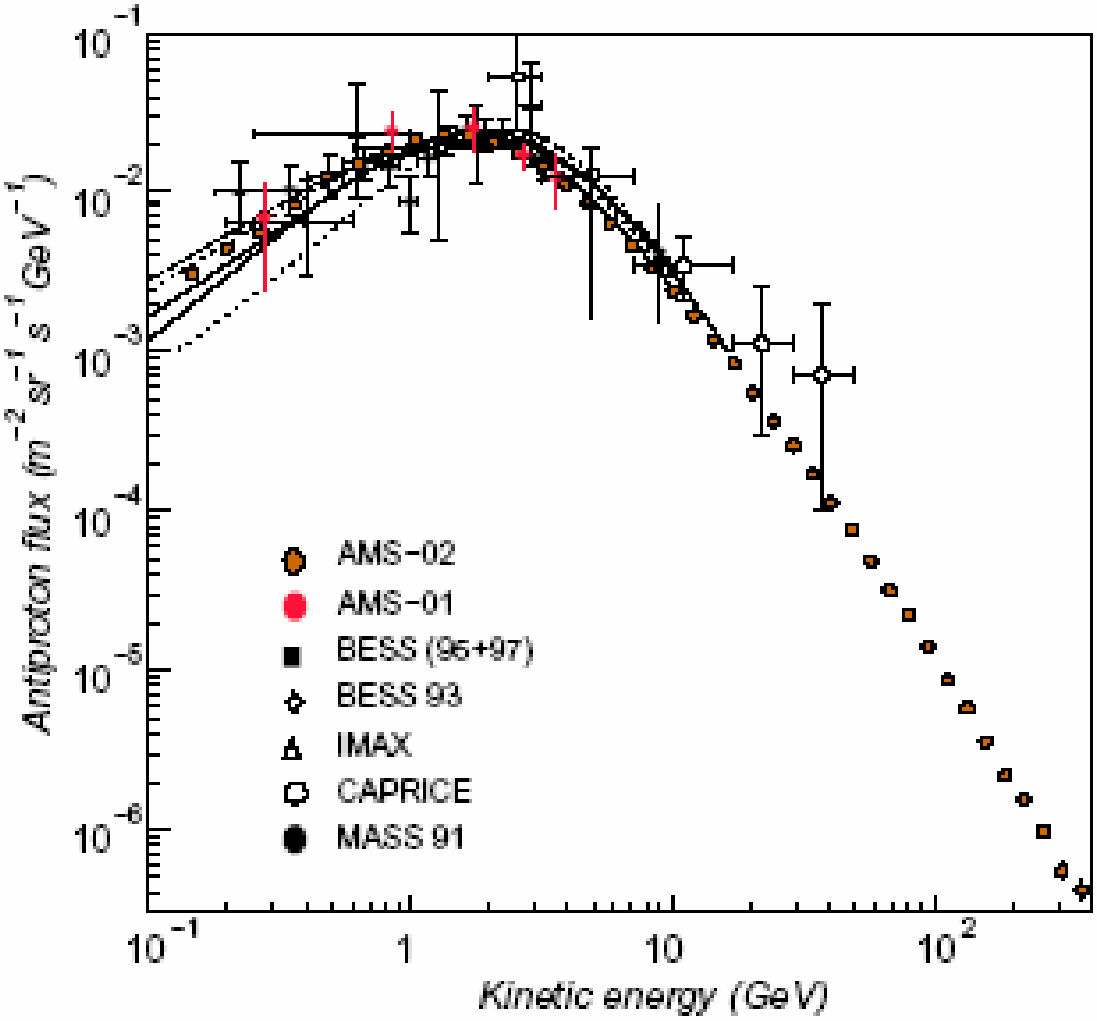

CR antiproton flux measured in different experiments.

The plot also shows expected statistics for the AMS-02 that has the potential to discover high-energy bumps that could be produced by exotic sources like the annihilation of neutralinos, the SUSY candidate for the dark matter.

[**Reference**: D. Casadei (for the AMS Collaboration), “Cosmic ray astrophysics with AMS-02,‘‘ astro-ph/0404529.]

Reference	Instrument	He events	Rigidity (GV)	$\overline{\text{He}}$/He 95% limit
Smoot *et al* (1975)	Balloon	1.5×10^4	4–33	5×10^{-4}
	Supercond. magnet		33–100	2×10^{-2}
Badhwar *et al* (1978)	Balloon	1.7×10^4	4–10	1.7×10^{-4}
	Supercond. magnet		33–100	10^{-2}
Buffington *et al* (1981)	Balloon		1–1.8	2.2×10^{-5}
	No magnet			
Alcaraz *et al* (1999)	Space shuttle	2.86×10^6	1–140	1.1×10^{-6}
	Permanent magnet			
Sasaki *et al* (2001)	Balloon	$>6.6 \times 10^6$	1–14	0.7×10^{-6}
	Supercond. magnet			

Antihelium search results. The last column gives the antihelium to helium flux ratio at 95% confidence level. [**Reference:** Yu.V. Galaktionov, Rep. Prog. Phys. **65** (2002) 1243.]

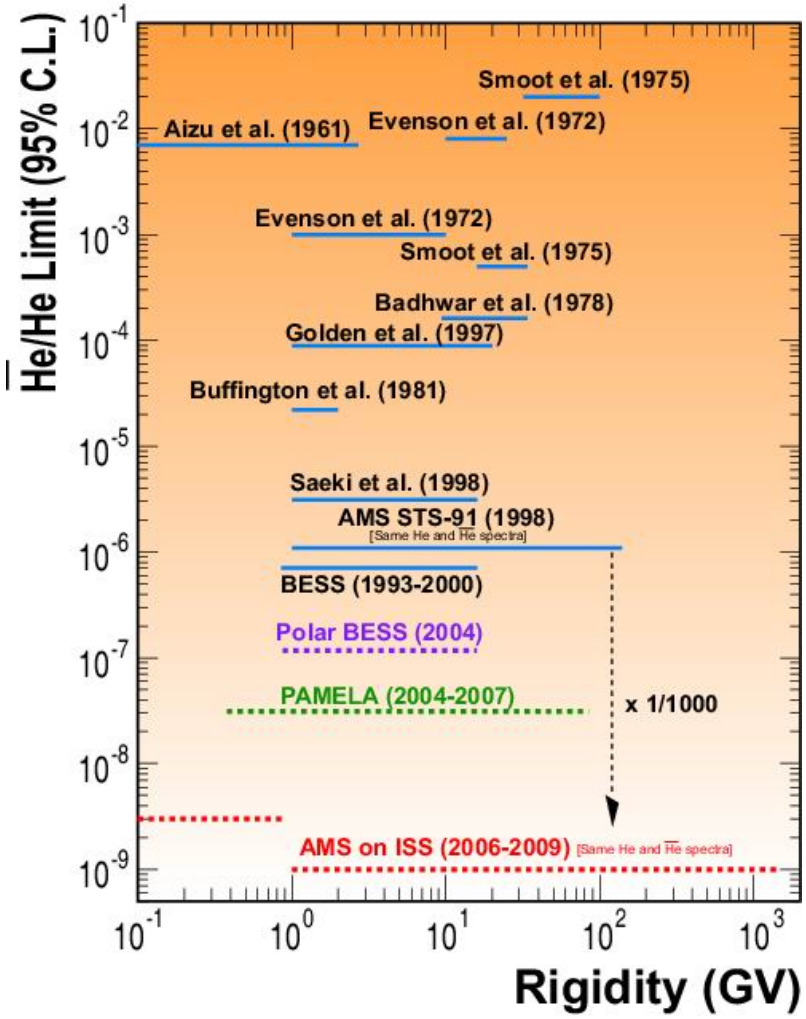

Upper limits on the antihelium to helium ratio in CR.

[**References:** M. Nozaki et al. (BESS Collab.), ICRC'26, OG.1.1.23; T. Saeki et al. (BESS Collab.), Phys. Lett. B **422** (1998) 319; *R. Battiston*, J. Phys. G: Nucl. Part. Phys. **29** (2003) 891; P. Picozza and A. Morselli, *ibid*., 903.]

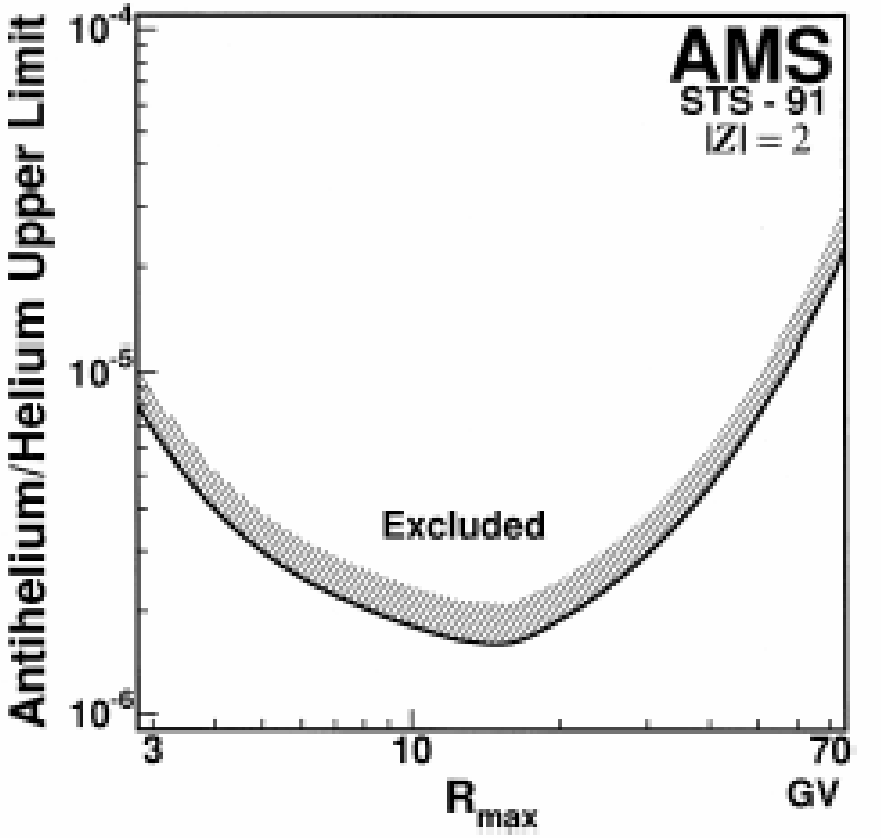

Upper limits on the relative flux of antihelium to helium in CR, obtained with the AMS Cosmic Ray Detector during STS-91 precursor flight (at the 95% confidence level), as a function of the rigidity range from R_{min} = 1.6 GV to R_{max}. In contrast with the AMS upper limits shown in the **left panel**, these results are independent of the assumptions about the incident antihelium spectrum.

[**Reference:** J. Alcaraz et al. (AMS Collaboration), Phys. Lett. B **461** (1999) 387.]

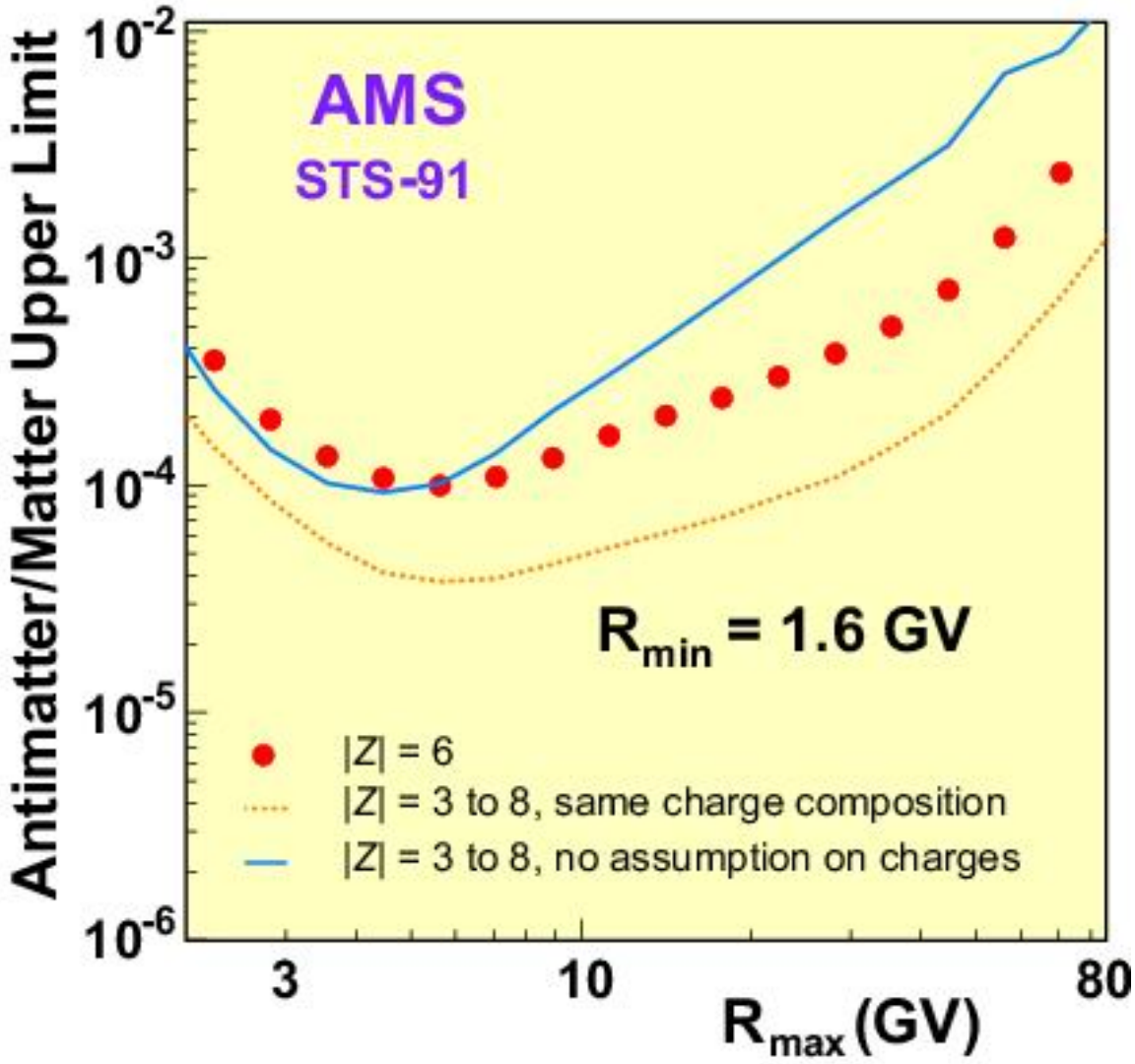

Upper limits on the antimatter-to-matter flux ratio under the conservative approach obtained with the AMS Cosmic Ray Detector during STS-91 precursor flight. Integrating over the rigidity range (from R_{min} = 1.6 GV to R_{max}), the limit curves are shown as a function of the maximal rigidity R_{max}.

[**Reference:** M. Cristinziani, Nucl. Phys. B (Proc. Suppl.) **114** (2003) 275; astro-ph/0303641]

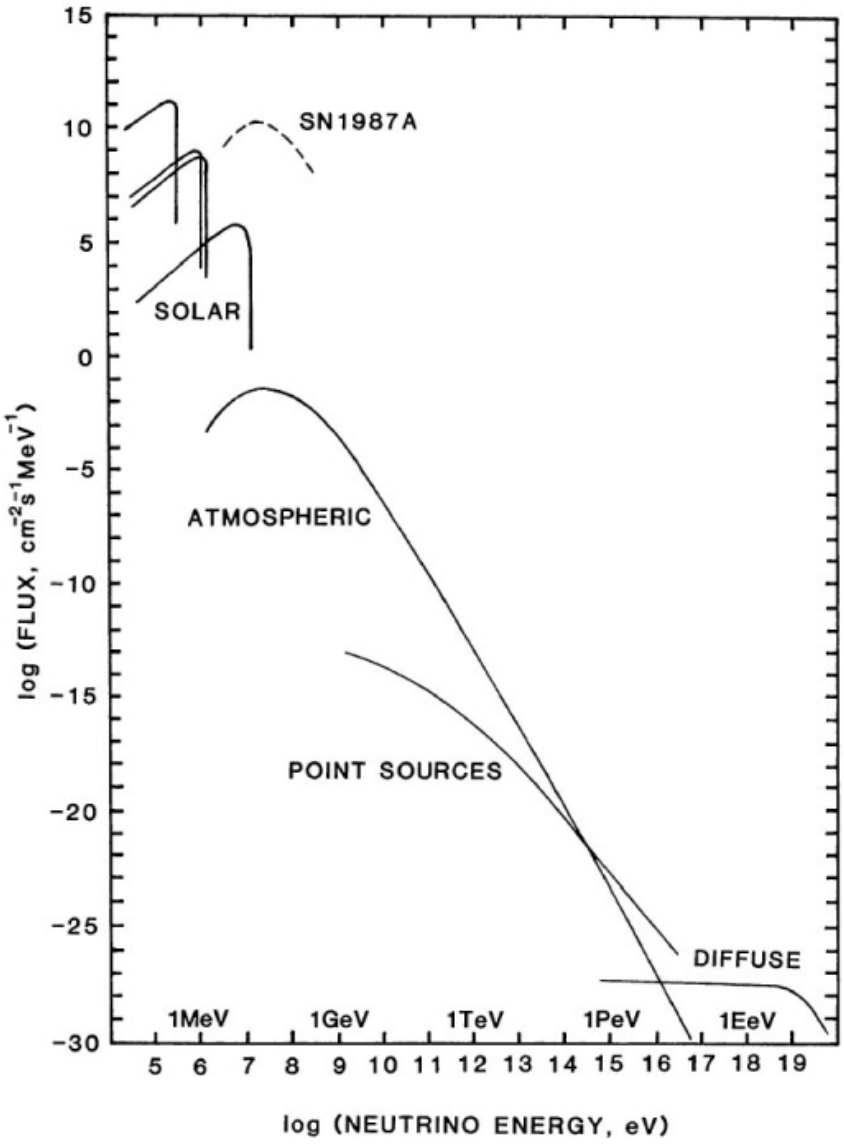

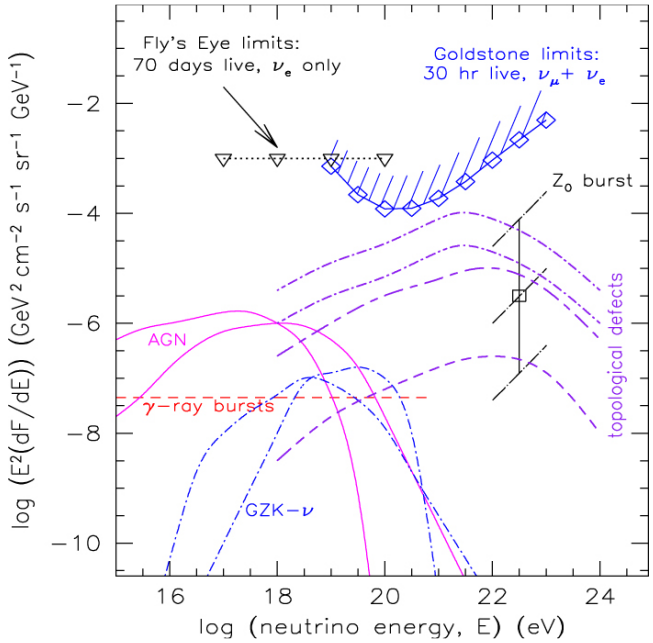

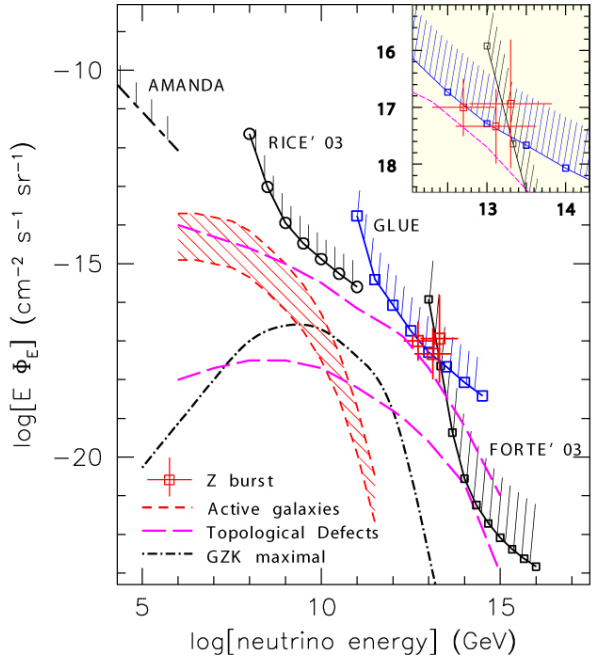

Plots of model neutrino fluxes and limits from several experiment

[From: A.M. Bakich, Space Sci. Rev. **49** (1989) 259-310; P.W. Gorham et al., astro-ph/0102435; P.W. Gorham et al., Phys. Rev. Lett. **93** (2004) 041101 (astro-ph/0310232)].